Photoemission Calculation Including Photon Field Variation in the Surface Region

THESIS SUBMITTED FOR THE DEGREE OF DOCTOR OF PHILOSOPHY (SCIENCE)

Pranati Das

Department of Physics

North Bengal University

West Bengal, India.

ACKNOWLEDGEMENTS

Throughout the length and breadth of life there are many people for whose help I am grateful and because of whom I have been able to complete my thesis. The number is so many that it is not possible to mention them all in the span of one or two pages. But I would like to record my cordial gratitude and indebtedness to all of them.

I am specially grateful to my supervisor Dr N Kar, Department of Physics, N.B.U, for his dynamic and enlighting guidance and electrifying encouragements from the very commencement of this work. I am really indebted to him as without his help and guidance this thesis would not have been possible. I am also grateful and indebted to all my teachers of the Physics Department for their timely and helpful suggestions. In particular, I an indebted to Dr P Mandal for his kind co-operation and numerous help. I would like to thank to all of my colleagues and particularly to Mr R K Thapa for his valuable suggestions and helps. I am also indebted to NCSI, Bangalore, who provided me with valuable references and reprints. I must be thankful to the North Bengal University and CSIR, India, for their award of fellowships. The co-operation of the staff-members of the University Library and Physics Department is gratefully acknowledged. Finally, I am indebted to my parents who are the fountain of my inspiration and determination.

Pranati Das

Date - June 29, 1995 (Pranati Das)

TABLE OF CONTENTS

LIST OF FIGURES & TABLE

CHAPTER-I

Introduction

In photoemission, electrons are emitted when electromagnetic radiation, typically in the visible or ultraviolet region is incident on the surface. Photoemission phenomenon was first observed by Hertz[1] (1887) and later on, Einstein[2] described it as a quantum phenomenon. Nowadays, photoemission spectroscopy has become a very popular probe to know both the surface and the bulk electronic properties of a solid.

In Ultraviolet Photoemission Spectroscopy (UPS) and X-ray Photoemission Spectroscopy (XPS) the source of radiations are respectively an ultraviolet lamp and an X-ray tube. The availability of synchrotron radiation has been very important to the development of photoemission experiment. Synchrotron radiation provides a continuous spectrum extending from the infra-red to the X-ray region. UPS is conceptually identical to XPS except that the incident photons are in the energy range of 20-150 eV. It is ideally suited for the study of the valence band electrons in the surface region. The Universal Curve of mean free path shows that UPS photoelectrons originate from the surface region and valence band photo cross-section is large at UPS excitation energies.

The variables involved in the photoemission spectroscopy process are the energy, polarization, and the angle of incidence of the incident photon and also the energy, polarization and the emission angle of the emitted electrons (fig 1.1). In various photoelectron spectroscopy techniques, only a few of such variables are varied keeping others to be constant. In the constant final state spectroscopy (CFS), the energy analyzer is set to a specific energy, and the incident photon energy is swept. CFS provides a direct measure of both the initial density of states and the surface sensitivity. In constant initial state spectroscopy (CIS), the photon energy ($\hbar\omega$) and the electron kinetic

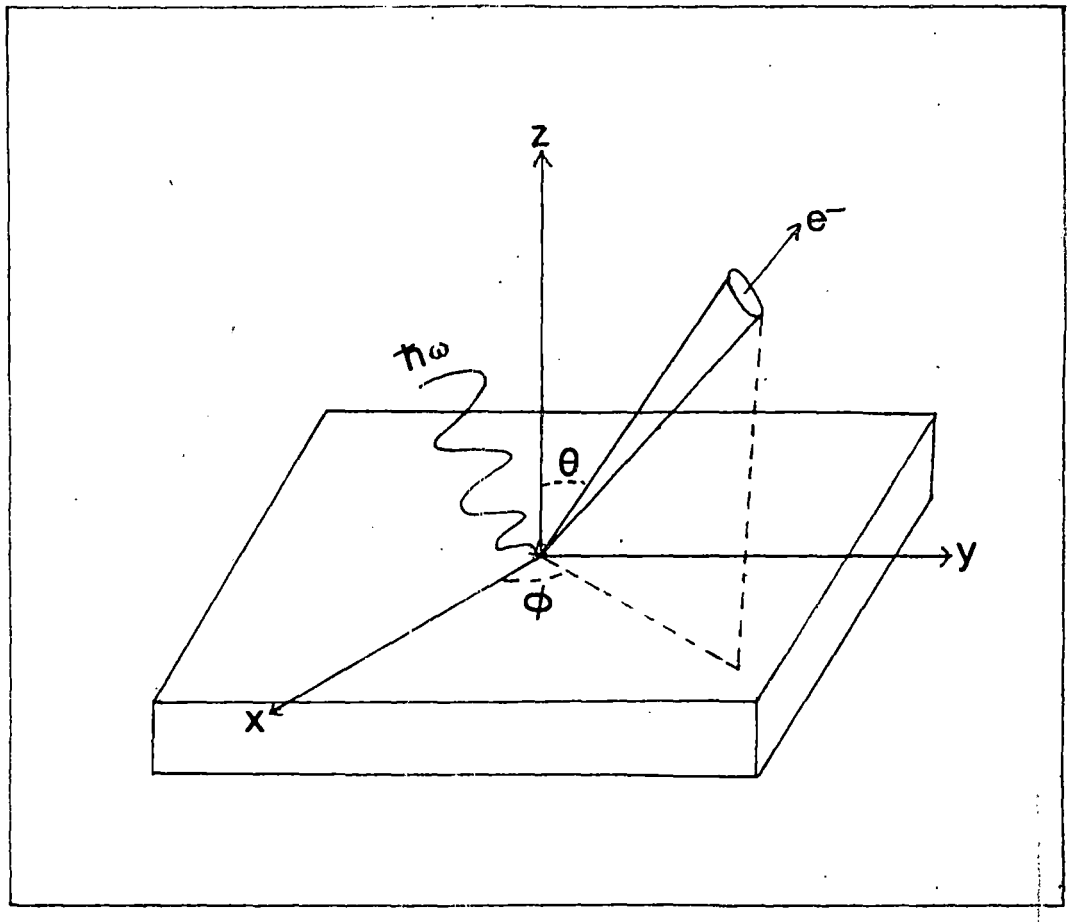

Fig 1.1 Schematic representation of photoemission

energy (E) are varied simultaneously so that E- $\hbar\omega$ is kept constant. In this mode of operation a direct measure of the final state density is obtained. In the vectorial photoeffect polarization of the incoming photon is varied while by analyzing the electron spin one obtains spin polarized photoemission.

Photoemission techniques can be classified according to the manner in which the energy and momentum of the incident photon and the ejected photoelectron are controlled. When the emitted electrons are collected for a specified angle (θ,ϕ) we get angle-resolved photoemission and when all emitted electros are collected by a hemispherical detector we get the angle integrated photoemission. Escape length for electrons in the 10 eV -100 eV range is of the order of 10 A^0, so the process is surface sensitive. Angle integrated photoemission gives joint density of states while, the angle-resolved photoemission gives a detailed information of band structure, surface sensitiveness etc. In angle resolved photoemission spectroscopy the direction and energy of an ejected photoelectron is measured to determine the photoelectron wavevector $\vec{K}$. At the surface the wavevector conservation breaks down in the direction perpendicular to the surface due to the lack of periodicity in this direction. But, in the direction parallel to the surface periodicity remains and the wavevector conservation still holds as

$$\vec{K}_{\parallel}=\vec{k}_{\parallel}+\vec{g}$$

where, $\vec{k}_{\parallel}$ and $\vec{g}$ are the parallel component of the bulk electron wavevector and reciprocal lattice vector respectively. From the energy conservation at the surface we may write

$$\frac{\hbar^2 \vec{K}_\perp^2}{2m} = [E_f(\vec{k}) - E_v] - \frac{\hbar^2}{2m}(\vec{k}_\parallel^2 + \vec{g}^2)$$

Therefore, we see that if we know the energy at the final state $E_f(\vec{k})$ and the vacuum level E_v we can calculate the directions of photoelectrons generated by a bulk transitions.

In normal photoemission, photoelectrons are emitted in the direction normal to the crystalline surface and we have $\vec{k}_\parallel = 0$. This considerably simplifies the problem as we are confined to sampling bulk states as a function of $\vec{k}_\perp$ along a specific line in $\vec{k}$ space.

In the independent-particle approximation the expression for current density in three-step model of photoemission process may be written from Fermi Golden rule[3] as

$$\frac{di(E)}{d\Omega} = \frac{2\pi}{\hbar} \sum_i |\langle \psi_f | H' | \psi_i \rangle|^2 \delta(E - E_f)\, \delta(E_f - E_i - \hbar\omega)\, f_0(E - \hbar\omega)\, [1 - f_0(E)]$$

(1.1)

where H' is the perturbation responsible for photoemission by radiation of frequency ω, given by $H' = (e/2mc)(\vec{A}.\vec{p} + \vec{p}.\vec{A})$, $\vec{p}$ being the one electron momentum operator and $\vec{A}$ is vector potential of the photon field. $|\psi_i\rangle$ and E_i refer to initial state wavefunction and energy and $|\psi_f\rangle$ and E_f to the final state wavefunctions and energy, and $f_0(E)$ denotes the Fermi occupation function. The sum is taken over all occupied states and the δ-functions establish the energy selection rule. Therefore, the photoemission cross-section calculation is essentially the evaluation of the matrix element $\langle \psi_f | H' | \psi_i \rangle$ and one has to know the initial and final state wavefunctions and the photon field at the surface.

The final state wavefunction is nonvanishing outside the solid and represents the electron arriving at the detector while the initial

state wavefunction describes the bound electron before excitation, both the wavefunctions being the solution of Schrödinger equation of the unperturbed system. The initial and the final states are modified from the bulk states by the presence of the surface. The electronic states in the presence of surface have been calculated self-consistently by a number of authors. These methods are generally based on Linear Augmented Plane Wave (LAPW)[4-7] and Linear Muffin Tin Orbitals (LMTO)[8-10] methods - and these involve a substantial computational effort. However, so far, photoemission calculations have not incorporated the wavefunctions resulting from such self-consistent procedure.

There has been a number of approaches for photocurrent calculation. Mahan[11](1970) gave a scattering approach (first proposed by Adawi[12] (1964)) of photoemission in the free electron model and considered the angular distributions of photoelectrons. Ashcroft and Schaich[13] (1970) developed a model of photoemission theory on the basis of quadratic response theory and independent particle approximation. The calculated results are similar to that of Mahan. Also, they have studied photoemission from nearly free electron and tight binding model of a solid and the photoyield from the surface states. Endriz[14] (1973) developed a modified form of the Mitchell-Makinson[15,16] time dependent perturbative calculation of the surface photoeffect considering both the electron excitation back into the metal as well as electron emission into the vacuum. The calculation was based on Bloch hydro-dynamic equations where an improved treatment of surface polarization charge density variations had been considered. The results for the case of aluminium and other nearly free electron metals agree with the experimental data but fails to reproduce the direct optical excitation of the surface photoelectric effect in the alkali metals.

Kliwer (1976)[17] presented both local and non local theory of photoemission in detail in which the surface photoeffect was identified as being exclusively due to the presence of a longitudinal component of the vector potential inside the solid.

Mativ & Metiu[18] (1980) were primarily concerned with the fields in the immediate vicinity of the interface and developed a scheme for a general solution of Feibelman's model. They determined a dielectric function which in contrast to conventional models is continuous across the interface. The plot of the photoyield versus photon energy did not show the behaviour as obtained by Feibelman[19] and Levinson *et al*[20] for aluminium. They found their model to be valid for photon energy greater than the plasmon energy and the model was applicable only to free electron type of solids.

The photon field can also be calculated from hydrodynamical model which considers the electron hole-spectrum and uses the dielectric function. Using this model Kempa and others[21] (1983, 1985) calculated the vector potential for aluminium and also had incorporated the photon field in the photoyield calculation. It is shown that the frequency dependence of the photoyield is essentially due to the behaviour of the electric field but does not depend very much on the initial and final state wavefunction. Their results for photoyield agree with the experimental data. Barberan and Inglesfield[22] (1981) calculated photoemission from aluminium considering the band structure effects but they have neglected the screening of the photon field. Although their results fail to produce the observed variation of photoemission intensity from a constant initial state as a function of photon energy - it gives good agreement with the experimental data at fixed photon

energy. Further, using the simple hydro dynamical method for non-local screening at a metal surface they have calculated photocurrent from both the surface state and the Fermi level of aluminium which gives good agreement with the experimental results.

Meyers & Feuchtwang[23] (1983) developed a detailed theory of photoemission from a free electron metal with a vanishingly small optical absorption above the plasmon energy. Calculated photoelectron energy distribution curves (EDC) differ significantly both in magnitude and dependence on photon energy from the conventional free electron results. Lee & Schaich[24] (1988) presented a series of model calculations on a simple theory of photoemission yield for jellium metals considering the spatial variation for both the potential energy barrier and the photon field. They have shown that a suitable choice of the parameters can made the predictions to agree with experimental data retaining the surface effect mechanism.

Feibelman[19] (1975) calculated the vector potential in the neighbourhood of a flat jellium-vacuum interface, for the case of long wavelength transverse electromagnetic wave incident form the vacuum. The Random Phase Approximation (RPA) to the conductivity tensor was used and the required one electron wave functions were evaluated from the self-consistent surface barrier potential of Lang and Khon[25]. Vector potential was studied in detail, as a function of the parameters of the surface and the photon energy which may be used for the calculation of refraction effects in surface photoemission and in reflection spectroscopy. Again for the jellium model, he calculated the surface photocurrent using the same surface potential barrier model to evaluate the initial and final state wavefunctions and the spatial behaviour of the photon field. The shapes of the surface photoelectron energy and the

angular distribution are independent of the surface structure, while, the total surface photoyield versus frequency is strongly dependent on it.

Mukhohopadhay & Lundqvist[26] (1978) calculated the electromagnetic field near a semi infinite jellium surface. The solutions for the vector potential in the vacuum and bulk regions are of asymptotic form and in the surface region this form becomes modified due to the potential. They concluded that the solution in the surface region depend essentially on the particle-hole excitation. They used their formulation to study the semi classical infinite barrier (SCIB) model of the sharp metal surface and the long wavelength limit for the electromagnetic wave incident on a diffuse metal surface which have been considered by Kliewer and Feibelman.

Photoemission calculations based on LEED formalism have been done by several authors e.g., Liebsch[27], Pendry[28], Pendry & Hopkinson[29]. Liebsch (1974) presented a detailed theory of angle-resolved photoemission from the localized adsorbate orbital considering the effects of final states. In some theoretical approaches, photoemission process is considered as a one-step quantum mechanical event in which an electron, under the influence of the electromagnetic field, is removed from an occupied state and deposited at the detector. Liebsch (1976) expresses the initial state wavefunction as the sum of the spherical waves emanating directly from the atom at the origin and also the scattered waves from the surrounding atoms, to the detector. Both multiple and single scattering processes are included. The approach is similar to LEED but here, electron source is the spherical wave rather than the external beam of plane wave electrons.

A sophisticated theory of photoemission has been developed by

Pendry[28] (1976) where, the wavefunctions for both the initial and final states for the semi-infinite solid are constructed accurately. The semi-infinite solid is supposed to be composed of stack of parallel layers of atoms with a potential of muffin-tin form. The initial state wavefunction has different forms in the interstitial and muffin-tin regions. The final state wavefunction is represented by an electron going to the detector as in Low Energy Electron Diffraction. The vector potential was taken to be a constant and a convenient choice of a gauge for the vector potential simplifies the mathematical calculations. For the scattering from each layer, the reflection and transmission matrices have been calculated and this procedure is continued first for a pair of layers and then pair of pairs and so on. This is called the layer doubling method to consider the finite thickness of the crystal. The conditions for the convergence of the method is to introduce an imaginary part of the potential (V_{0i} <0) to consider some finite absorption. This is computationaly a fast method and can also be extended to photoemission from surfaces covered with overlayers. The formalism has been applied to both clear and adsorbate covered surfaces[30].

Ishii & Aisaka[31] (1991) presented a theoretical analysis of the angle-resolved photoemission spectrum by using a dynamical multiple scattering formalism for photoelectrons. Their calculated spectrum shows a different peak position compared with that of band calculation with the same muffin-tin potential which may be due to the multiple scattering effect of the photoelectrons and the mean free path effect for both the initial and final states of photoexcited electrons. However, the discrepancy between the calculated and the experimental results[32] is very small in case of Al(100) but large for Na(110).

The wavelengths of radiation typically used for exciting the photoelectrons are long compared to atomic dimensions. This is the argument for ignoring the spatial variation of the incident electromagnetic field and take it to be constant. This assumption of constant field can be utilised to make the computation simpler by using the commutation relation between $\vec{p}$ and $\vec{A}$ and choosing a convenient gauge - as has been done, for example, by Pendry.

In many cases the results of such calculations gave reasonable agreement with experiment. However, in certain situations, e.g. variation of photocurrent with photon energy, the consideration of spatial variation of photon field is important. Bagchi & Kar[33] showed that, even with a simple model, consideration of variation of field near the surface gave a reasonable qualitative agreement with experimental results for the photocurrent from the tungsten surface as a function of photon energy. Feibelman has also considered this problem in some detail with his much more sophisticated self-consistent field calculation with the jellium model, and applying this to the case of aluminium showed that the spatial variation of the photon field should not be ignored. Feibelman's calculation is, however, applicable only to free electron metals, and further, the self-consistent field calculation is an extremely involved process and no attempt has been made so far to incorporate this field variation into a LEED type calculation.

The model of Bagchi & Kar, on the other hand, uses experimentally measured optical data as input and is therefore, much more empirical in character. However, the expression for field can be analytically derived in the long wavelength limit for this model and so it is easier to incorporate into a photoemission calculation. In addition, this model may be applied to metals other than free electron

types. We note that being a 'local' model - it is inadequate for the exact description of fields -- but it is definitely an improvement on constant field. The fields for a number of elements have been calculated with this model[34]. We have used this model in our photoemission calculations and so, at this point we give a brief description of the fields resulting as solutions of this model.

In this model, the z-direction is taken to be perpendicular to the nominal surface chosen as z=0 plane and the metal is assumed to occupy all the space to the left of this plane. The response of the electromagnetic field is bulk like everywhere except in the surface region defined as $-a/2 \leq z \leq a/2$. In this region the model dielectric function is chosen to be a 'local' one which interpolates between the bulk value and the vacuum value (unity) out side as

$$\epsilon(\omega) = \begin{cases} \epsilon_1(\omega) + i\epsilon_2(\omega) & z \leq -\frac{a}{2} \\ \frac{1}{2}[1+\epsilon(\omega)] + [1-\epsilon(\omega)]\frac{z}{a} & |z| \leq \frac{a}{2} \\ 1 & z \geq \frac{a}{2} \end{cases} \tag{1.2}$$

For a p-polarised light, incident on the surface plane at an angle θ_i with z-axis, the magnetic field $B(z) = B(Q,\omega,z)$ (where $Q=(\omega/c)\sin\theta_i$ is small) is in the y-direction and it obeys the following equation with $\epsilon=\epsilon(\omega)$

$$\frac{d}{dz}\left(\frac{1}{\epsilon}\frac{dB}{dz}\right) + \left(\frac{\omega^2}{c^2} - \frac{Q^2}{\epsilon}\right)B = 0$$

This equation may be obtained from Maxwell's equations. The components of the electric field can be obtained from the magnetic field by using the relations

$$E^x(\vec{Q},\omega,z) = \frac{c}{i\omega\epsilon}\frac{dB}{dz}$$

$$E^z(\vec{Q},\omega,z) = -\frac{\sin\theta_i}{\epsilon}B$$

The solution of the above equation leads to the normal component of the electric field in the limit $\omega a/c \to 0$

$$\frac{E_z(\vec{Q}\to 0,\omega;z)}{E_0} = \begin{cases} -\dfrac{\sin 2\theta_i}{\sqrt{[\epsilon(\omega)-\sin^2\theta_i]}+\epsilon(\omega)\cos\theta_i} & z<-\dfrac{a}{2} \\ -\dfrac{\sin 2\theta_i}{\sqrt{[\epsilon(\omega)-\sin^2\theta_i]}+\epsilon(\omega)\cos\theta_i}\dfrac{\frac{a\epsilon(\omega)}{1-\epsilon(\omega)}}{\frac{z}{a}+\frac{1}{2}\frac{1+\epsilon(\omega)}{1-\epsilon(\omega)}} & -\dfrac{a}{2}\le z\le\dfrac{a}{2} \\ -\dfrac{\epsilon(\omega)\sin 2\theta_i}{\sqrt{[\epsilon(\omega)-\sin^2\theta_i]}+\epsilon(\omega)\cos\theta_i} & z>\dfrac{a}{2} \end{cases}$$

(1.3)

In our calculation, we have made a slight change by taking the surface region from -a to zero. This transformation does not change the qualitative behaviour of the field in the different regions.

In this thesis, we have first used the free electron model for initial and final state wavefunctions and the case of normal photoemission from the Fermi level of aluminium for the (100) face was considered as an application. For improving the free electron wavefunctions, the initial (free-electron like) state was replaced by that calculated with a periodic potential in muffin-tin form. The case of aluminium was considered again and the calculated results were compared with the free electron results. Finally, the formalism for photocurrent calculation with a LEED type final state and band initial state with the field given by this model has been developed. However, numerical results for this case have not yet been computed.

In addition, we have calculated the local field near the surface of some dipolar lattices with hexagonal, hexagonal close-packed and diamond structure. The major part of the works included in this thesis have been published[38,41,52].

We may mention that the fields calculated from Bagchi & Kar model, along with free electron wavefunctions have also been used subsequently by Thapa & Kar for normal photoemission from beryllium and the results are to be published soon[39]. Also calculations with Kronig-Penney wavefunctions and fields from this model and the dielectric functions for a number of elements have been performed and published[40].

The contents of the thesis are organized as follows. In chapter-II the photoemission calculation using free electron wavefunction with a simple model for the spatially varying photon field and its application to aluminium has been presented. The photocurrent using the same simple form for the photon field, band wavefunctions and also a muffin-tin potential for aluminium and tungsten surface are presented in chapter-III. Chapter-IV has formalism for photocurrent calculation with time reversed LEED type final states, band initial states and the photon field variation in the surface region. Chapter-V contains the calculation of the dipolar fields near the surface of crystals with simple hexagonal, hexagonal close-packed and diamond structure. Precise summary of the total work done in this thesis and conclusion are given in chapter VI. The details of some involved mathematical calculations and the FORTRAN programs used are given in the APPENDIX. Reprints of publications are also included.

CHAPTER-II

Photoemission calculation with free electron wavefunction

2.1 Introduction

Photoemission experiments on surfaces of solids are basically concerned with the excitation of electrons by the incident photon energy. A simple calculation of photocurrent (in one electron approximation) involves the evaluation of matrix elements (equation 1.1) of the form $\langle \psi_f | H' | \psi_i \rangle$, where $| \psi_i \rangle$ and $| \psi_f \rangle$ denote the initial and final one-electron states whose energies are connected by $E_f - E_i = \hbar\omega$ and $H' = (e/2mc).(\vec{p}.\vec{A} + \vec{A}.\vec{p})$. $\vec{p}$ being the one-electron momentum operator and $\vec{A}$, the vector potential associated with the photon field. The states $| \psi_i \rangle$ and $| \psi_f \rangle$ are modified from the bulk states by the presence of the surface. Similarly, the photon field also has a spatial variation in the surface region.

In standard photoemission calculations[27,28] the one-electron states are calculated with a high degree of accuracy - but the variation of the photon field is generally neglected. Depending on the type of the experimental data one intends to compare the calculation with, this may or may not be a reasonable approximation. In the case where one looks at the photoemission current as a function of photon energy with a constant initial state, the photon field variation in the surface region needs to be considered more carefully. However, a first principles calculation of the electromagnetic field in the presence of the surface is an extremely complex problem - only for the case of jellium the results are available[19,26]. Bagchi and Kar[33], on the other hand, computed the field in a simple 'local' model, using experimentally determined frequency-dependent dielectric functions as parameter, and they used this for calculation of photocurrent from the surface state of tungsten. This simple model is applicable to those elements for which the frequency-dependent dielectric functions are known. In this chapter, we use this model in conjunction with free-electron wavefunctions for

electron states and show that the results obtained agree qualitatively with experimental data and the theoretical results obtained by more sophisticated jellium field calculations. This would indicate that we may use the simple model for calculation of photoemission cross-section of other metals for which the jellium results would not be applicable. The contents of this chapter have already been published[38]. Subsequently, a successful application in the case of berryllium has also been made[39].

We are considering the photoemission to take place along z-axis, which is normal to the surface. We may therefore write H' as

$$H' = \frac{e\hbar}{imc}\left[\tilde{A}_\omega(z)\frac{d}{dz}+\frac{1}{2}\frac{d}{dz}\tilde{A}_\omega(z)\right]$$

$$\text{where,}\quad \tilde{A}_\omega(z)=\frac{A_\omega(z)}{A_0}$$

with $A_\omega(z)$ as the component of the vector potential along z-axis, and A_0 is the amplitude of the incident beam. The formula for photoemission cross-section (equation 1.1) can be written as

$$\frac{d\sigma}{d\Omega} \approx \frac{k_f^2}{\omega}\left|\langle\psi_f|\tilde{A}_\omega(z)\frac{d}{dz}+\frac{1}{2}\frac{d}{dz}\tilde{A}_\omega(z)|\psi_i\rangle\right|^2$$

(2.1)

To evaluate the matrix element in equation (2.1) we have to construct ψ_i, ψ_f and determine $\vec{A}_\omega$.

2.2 Initial and final state wavefunctions

The wavefunctions for both the initial and final states are calculated in the free electron model with the potential given by

$$V(z)=V_0\theta(z) \qquad \text{where,}\quad V_0=E_F+\phi$$

E_F being the energy at the Fermi level in the free electron model and ϕ the work function, $\theta(z)$ is the step function defined as: $\theta(z)=0$ for $z<0$

and $\theta(z)=1$ for $z>0$ as shown in fig 2.1. By matching the wavefunctions at the surface plane $z=0$, we may write the initial state wavefunction as

$$\psi_i(\vec{r}) = \begin{cases} \left[e^{ik_i z} + \dfrac{ik_i+\chi}{ik_i-\chi} e^{-ik_i z}\right] e^{i\vec{k}_\parallel \cdot \vec{r}_\parallel} & z<0 \\ \dfrac{2ik_i}{ik_i-\chi} e^{-\chi z} e^{i\vec{k}_\parallel \cdot \vec{r}_\parallel} & z>0 \end{cases}$$

$$\text{where,} \quad k_i^2 = \frac{2m}{\hbar^2} E_i - \vec{k}_\parallel^2, \quad \chi^2 = \frac{2m}{\hbar^2}(V_0 - E_i) + \vec{k}_\parallel^2$$

(2.2)

and $\vec{k}_\parallel$ and $\vec{r}_\parallel$ are the components of $\vec{k}$ and $\vec{r}$ in the x-y plane i.e. the plane parallel to the surface.

Similarly, the final state wavefunction may be written as

$$\psi_f(\vec{r}) = \begin{cases} \left[e^{iqz} + \dfrac{q-k_f}{q+k_f} e^{-iqz}\right] e^{i\vec{k}_\parallel \cdot \vec{r}_\parallel} & z>0 \\ \dfrac{2q}{q+k_f} e^{ik_f z} e^{i\vec{k}_\parallel \cdot \vec{r}_\parallel} & z<0 \end{cases}$$

$$\text{where,} \quad \vec{k}_f^{\,2} = \frac{2mE_f}{\hbar^2} - \vec{k}_\parallel^2, \quad \vec{q}^2 = \frac{2m}{\hbar^2}(E_f - V_0) - \vec{k}_\parallel^2, \quad E_f = E_i + \hbar\omega$$

(2.3)

2.3 Photon field

The model of Bagchi and Kar[33] is employed for the computation of $A_0(z)$. We assume the z-direction to be perpendicular to the nominal surface which is chosen as $z=0$. The slight change made from the model of Bagchi & Kar seems to be more realistic to us and is also more convenient when we want to include the periodic potential later. The metal is assumed to occupy all space to the left of the $z=0$ plane as shown in fig 2.2. The response of the electromagnetic field is bulk-like

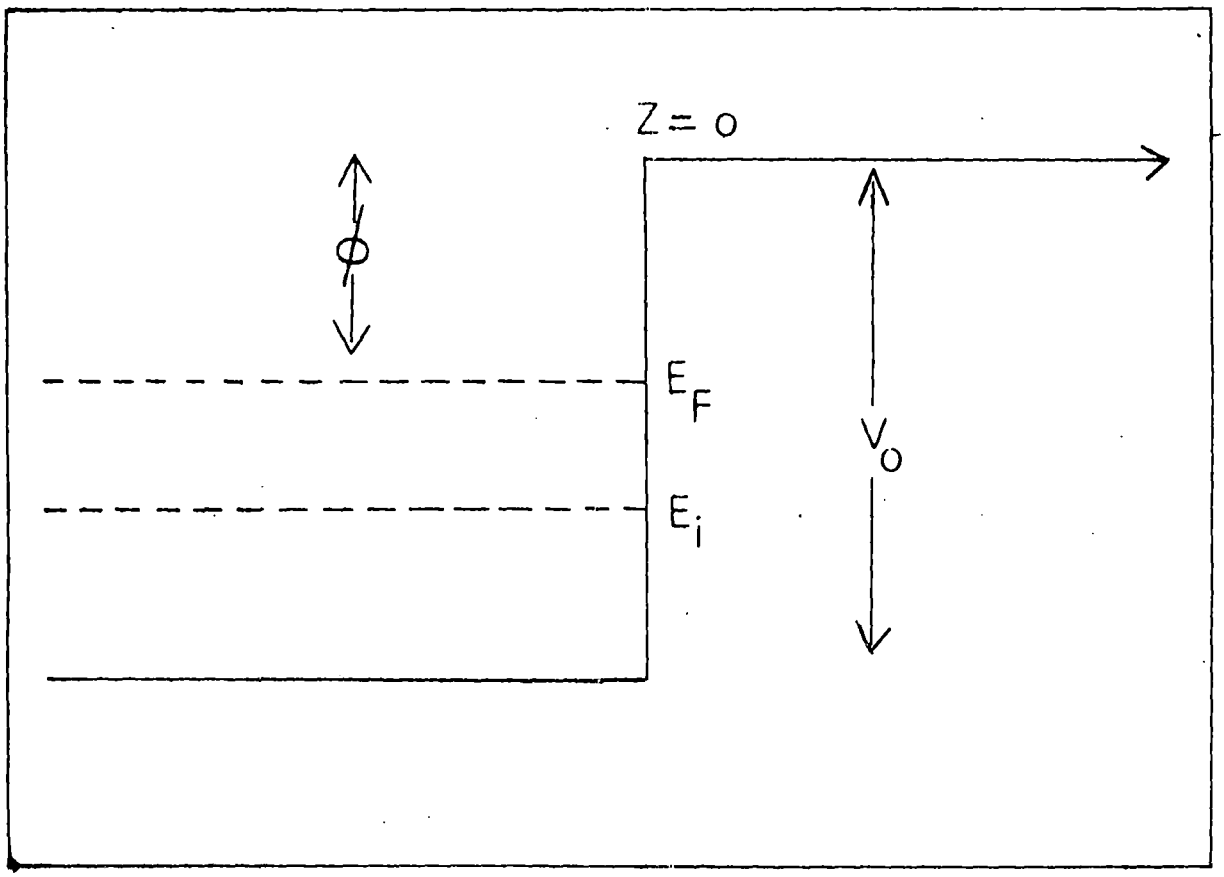

Fig 2.1 Model potential used for calculating wavefunctions for initial and final states. ϕ=4.25 eV & V_o=15.95 eV

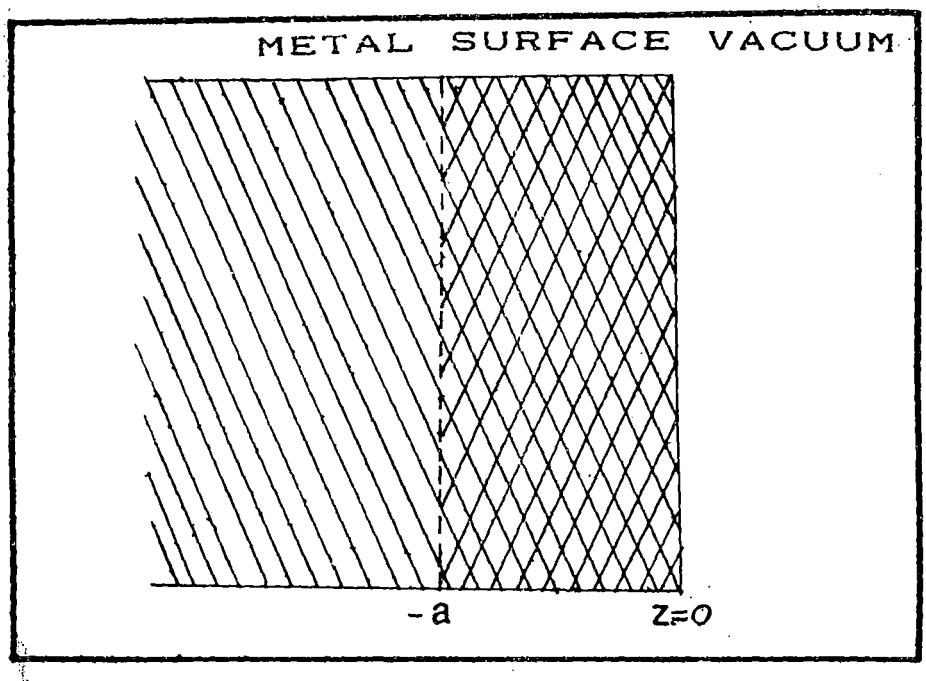

Fig 2.2 Schematic representation of the surface region used in the model

everywhere except in the surface region defined by $-a \leq z \leq 0$. In this region the model dielectric function is chosen to be a local one which interpolates linearly between the bulk value inside the metal and the vacuum value (unity) outside. The model frequency-dependent dielectric function is therefore given by

$$\epsilon(\omega) \equiv \begin{cases} \epsilon_1(\omega) + i\epsilon_2(\omega) & z < -a \\ 1 + [1-\epsilon(\omega)]\frac{z}{a} & -a \leq z \leq 0 \\ 1 & z > 0 \end{cases}$$

For the complex dielectric function $\epsilon(\omega,z)$ we use the experimental values given by Weaver[35]. We consider p-polarised light to be incident on the surface plane making an angle θ_i with the z-axis. We have chosen the origin to be at the metal-vacuum interface instead of at the centre of the surface region and by substituting (z+a/2) for z in equation (1.3) the calculated vector potential of interest, $A_\omega(z)$, in the long-wavelength limit $(\omega a/c) \to 0$ is

$$\tilde{A}_\omega(z) = \begin{cases} -\dfrac{\sin 2\theta_i}{\sqrt{[\epsilon(\omega) - \sin^2\theta_i]} + \epsilon(\omega)\cos\theta_i} & z < -a \\ -\dfrac{\sin 2\theta_i}{\sqrt{[\epsilon(\omega) - \sin^2\theta_i]} + \epsilon(\omega)\cos\theta_i} \dfrac{a\epsilon(\omega)}{[1-\epsilon(\omega)]z + a} & -a \leq z \leq 0 \\ -\dfrac{\epsilon(\omega)\sin 2\theta_i}{\sqrt{[\epsilon(\omega) - \sin^2\theta_i]} + \epsilon(\omega)\cos\theta_i} & z > 0 \end{cases}$$

(2.4)

2.4 Cross-section calculation

To calculate the photoemission cross-section we have to integrate the matrix element in equation (2.1) over the different regions of the solid i.e., vacuum, surface and bulk region using the expressions for Ψ_i,

ψ_f and $\vec{A}_\omega$ (equations 2.2-4) as

$$I = \int_{-\infty}^{\infty} \psi_f^* \left[\tilde{A}_\omega(z) \frac{d}{dz} + \frac{1}{2} \left[\frac{d}{dz} \tilde{A}_\omega(z) \right] \right] \psi_i dz$$

$$= \int_{-\infty}^{-a} \psi_f^* \tilde{A}_\omega(z) \frac{d\psi_i}{dz} dz + \int_{-a}^{0} \psi_f^* \tilde{A}_\omega(z) \frac{d\psi_i}{dz} dz$$

$$+ \frac{1}{2} \int_{-a}^{0} \psi_f^* \left[\frac{d}{dz} \tilde{A}_\omega(z) \right] \psi_i dz + \int_{0}^{\infty} \psi_f^* \tilde{A}_\omega(z) \frac{d\psi_i}{dz} dz$$

(2.5)

In the following sections we shall calculate each of the integral in equation (2.5) over the different region of the solid :

a) Bulk region

The photon field equation (2.4) is a constant here and we calculate analytically the first term of equation (2.5) as

$$I_1 = \int_{-\infty}^{-a} \psi_f \tilde{A}_\omega(z) \frac{d\psi_i}{dz} dz$$

$$= \frac{2qA_1}{q+k_f} \int_{-\infty}^{-a} e^{-ik_f z} e^{\alpha z} ik_i \left[e^{ik_i z} - \frac{ik_i+\chi}{ik_i-\chi} e^{-ik_i z} \right] dz$$

$$= iC_1 k_i \left[\frac{e^{-\alpha a} e^{-i(k_i-k_f)a}}{\alpha+ik_i-ik_f} - \frac{ik_i+\chi}{ik_i-\chi} \frac{e^{-\alpha a} e^{i(k_i+k_f)a}}{\alpha-ik_i-ik_f} \right]$$

where, $C_1 = \frac{2qA_1}{q+k_f}$ and $A_1 = -\frac{\sin 2\theta_i}{\sqrt{[\epsilon(\omega)-\sin^2\theta_i]+\epsilon(\omega)\cos\theta_i}}$

(2.6)

b) Surface region

It is already mentioned that the extent of the surface region is $-a \le z \le 0$ and the photon field has a spatial variation over this region and we calculate numerically two terms (2nd & 3rd term of equation 2.5) as

$$I_2 = \int_{-a}^{0} \psi_f \tilde{A}_\omega(z) \frac{d\psi_i}{dz} dz$$

$$= ik_i C_2 \int_{-a}^{0} \frac{e^{-ik_f z}}{\frac{z}{a} + B_1} \left[e^{ik_i z} - \frac{ik_i + \chi}{ik_i - \chi} e^{-ik_i z} \right] e^{\alpha z} dz$$

and $$I_3 = \frac{1}{2} \int_{-a}^{0} \psi_f^* \frac{d\tilde{A}_\omega}{dz} \psi_i dz$$

$$= -\frac{1}{2a} C_2 \int_{-a}^{0} \frac{e^{-ik_f z}}{\left(\frac{z}{a} + B_1\right)^2} \left[e^{ik_i z} + \frac{ik_i + \chi}{ik_i - \chi} e^{-ik_i z} \right] e^{\alpha z} dz$$

where, $B_1 = \frac{1}{1 - \epsilon(\omega)}$ and $C_2 = C_1 B_1 \epsilon(\omega)$

(2.7)

c) Vacuum region

Photon field has no spatial variation in the vacuum region and we calculate the 4th term of equation (2.5)

$$I_4 = \int_{0}^{\infty} \psi_f \tilde{A}_\omega(z) \frac{d\psi_i}{dz} dz$$

$$= ik_i C_3 \int_{0}^{\infty} \left[e^{-iqz} + \frac{q - k_f}{q + k_f} e^{iqz} \right] e^{-\chi z} dz$$

$$= ik_i C_3 \left[\frac{1}{iq + \chi} + \frac{q - k_f}{q + k_f} \frac{1}{\chi - iq} \right]$$

where, $C_3 = \frac{2A_1(-\chi)\epsilon(\omega)}{ik_i - \chi}$

(2.8)

The general expression for photoemission (equation 2.1) in terms of I_1, I_2, I_3 and I_4 would be

$$\frac{d\sigma}{d\omega} \approx \frac{k_f^2}{\omega} |I_1+I_2+I_3+I_4|^2$$

(2.9)

Using equations (2.6-2.9) we have calculated photocurrent numerically. Some portions of the computer programs are given in the appendix-II. However, to ensure convergence for z<0, one has to introduce a convergence factor due to lifetime effects. This is a standard procedure in Low Energy Electron Diffraction and photoemission calculations (see, for example, Pendry[36]). We do it here by introducing a factor $e^{-\alpha z}$ (for z<0) in the calculation of the matrix element - this is to take into account the inelastic scattering of electrons.

2.5 Results and discussion

We have applied our results for computing the normal photoemission from the Fermi level of aluminium (100) face, for which the experimental results as well as theoretical calculations using jellium model are available. The experimental results are shown in fig 2.3, the data of Levinson *et al*[20] having been used. For our calculations[38], we have taken ϕ = 4.25 eV and E_F=11.7 eV - these values have been given by Ashcroft and Mermin[37]. Since normal photoemission is considered $\vec{k}_{\parallel}$ =0; also θ_i is taken to be 45^0 as in the experiment. Our results for the photoemission cross-section are shown in fig 2.4 (with a= 10 atomic units). We see that there is qualitative agreement between the experimental data and the calculated photo-current. The calculated curve shows a peak at 11 eV, a minimum at 15 eV (~ plasmon energy) and again a broad peak around 20.5 eV. These features are also present in the experimental curve - although the ratio of the peak heights of the two peaks (below and above the plasmon energy) in the calculated and

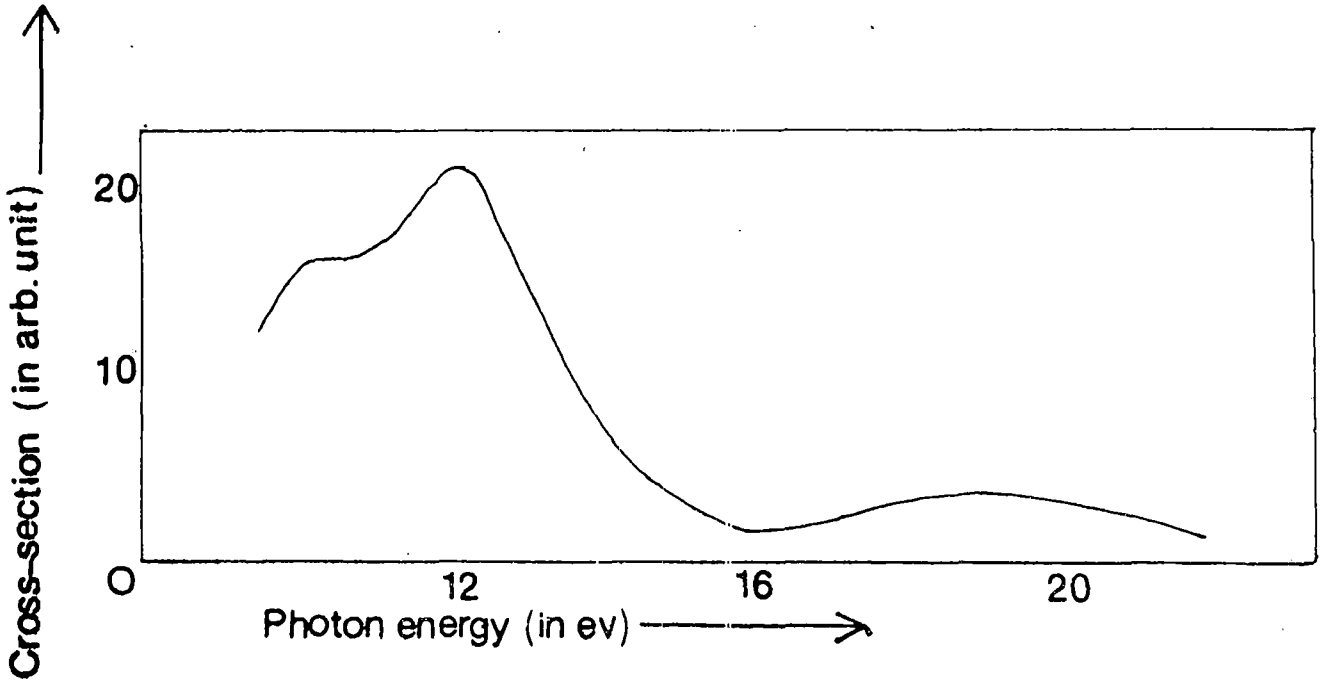

Fig 2.3 Experimental data of photoemission cross-section (in arb. unit) for normal photoemission from Fermi level aluminium (100) as a function of photon energy

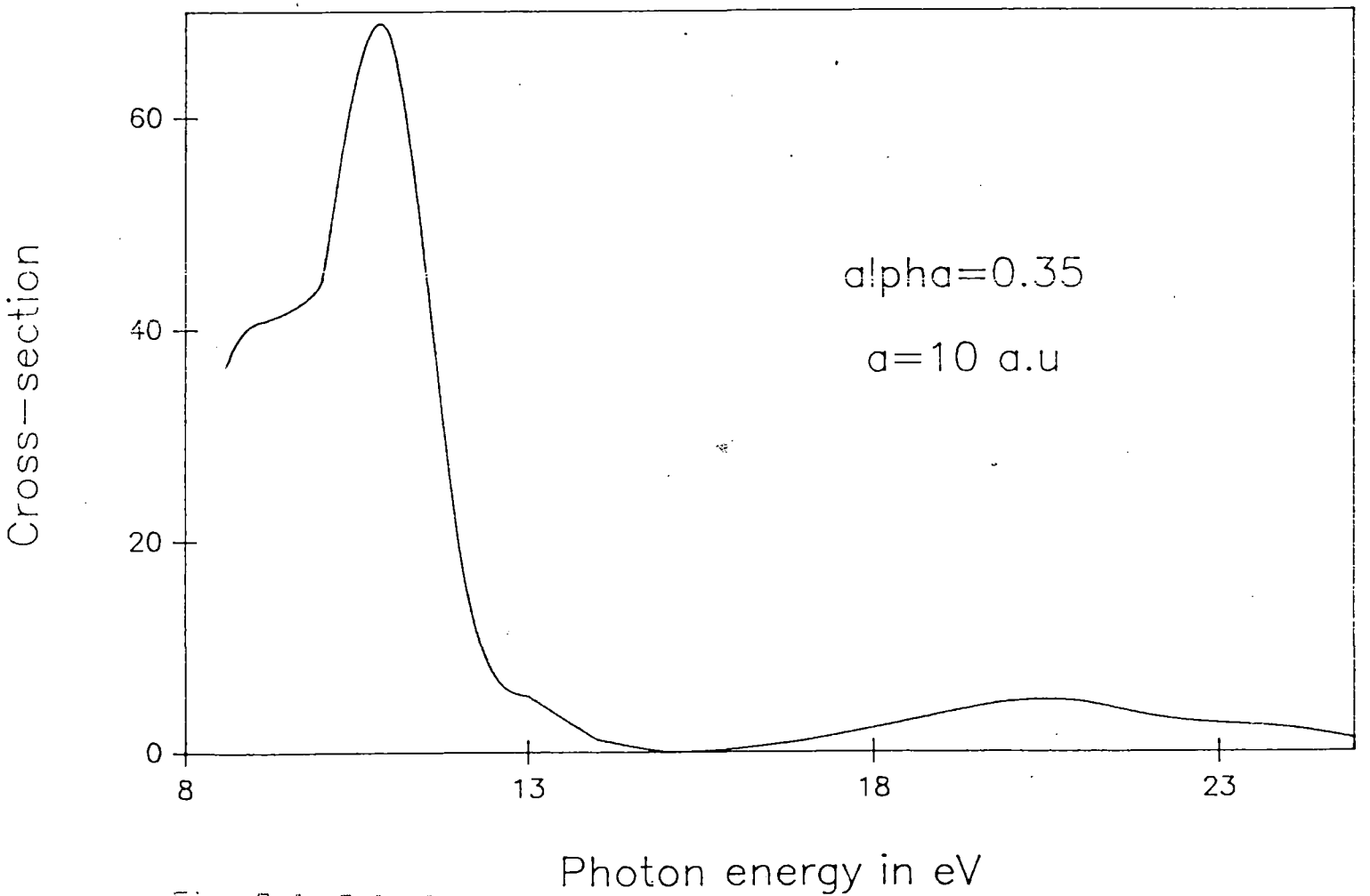

Fig 2.4 Calculated photoemission cross-section (in arb unit) for normal photoemission from Fermi level of aluminium (100) as a function of photon energy

experimental curve is different.

We further investigated the origin of the peak at 11 eV in the calculated spectrum and concluded that it is a surface feature. As evidence for that we plot the field $|A_\omega(z)|$ as a function of z in the surface region for $\hbar\omega$=11 eV (fig 2.5). We see that there is strong peak in the middle of the surface region. For $\hbar\omega$=15 eV and 20 eV, on the other hand, the plot of $|A_\omega(z)|$ does not show any peak in the surface region.

As further evidence of the peak at 11 eV being surface related, we show the results of a calculation of photo-current with fields given by the Fresnel refraction formula (obtained by putting a=0 in equation 2.4)

$$\tilde{A}_\omega(z) = \begin{cases} -\dfrac{\sin 2\theta_i}{\sqrt{[\epsilon(\omega)-\sin^2\theta_i]}+\epsilon(\omega)\cos\theta} & z<0 \\ -\dfrac{\epsilon(\omega)\sin 2\theta_i}{\sqrt{[\epsilon(\omega)-\sin^2\theta_i]}+\epsilon(\omega)\cos\theta} & z>0 \end{cases}$$

and the (free-electron) wavefunctions are the same as in equations (2.2-3). We see that, although there is a minimum around 12 eV, there is no peak around 11-12 eV (fig 2.6). Above the plasmon frequency, the curve shows a peak which is much more pronounced than that in the calculation with a surface region (fig 2.4). The peak in the experimental data above the plasmon frequency is also much less pronounced. Anyway, it is quite clear that the calculations with the simple Fresnel refraction formula is not even qualitatively correct - in particular, it completely fails to reproduce the peak around 11-12 eV.

We have thus shown that with a simple local model for the dielectric function, we can get a qualitative agreement with experimental data. There have been previous calculations, notably by

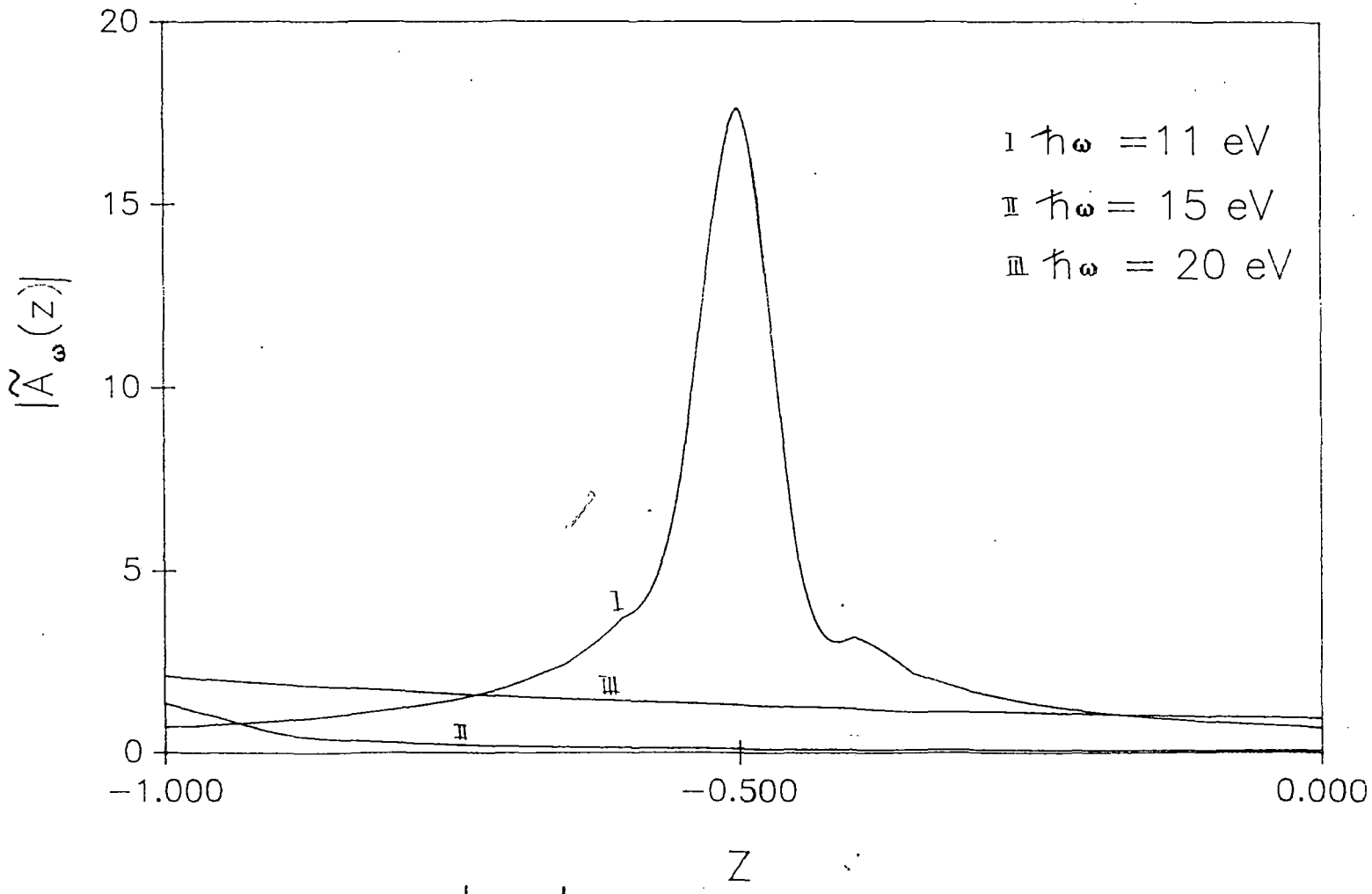

Fig 2.5 Plot of $|A\omega(z)|$ versus z in the surface for $\hbar\omega$ =11 eV, 15 eV and 20 eV for aluminium

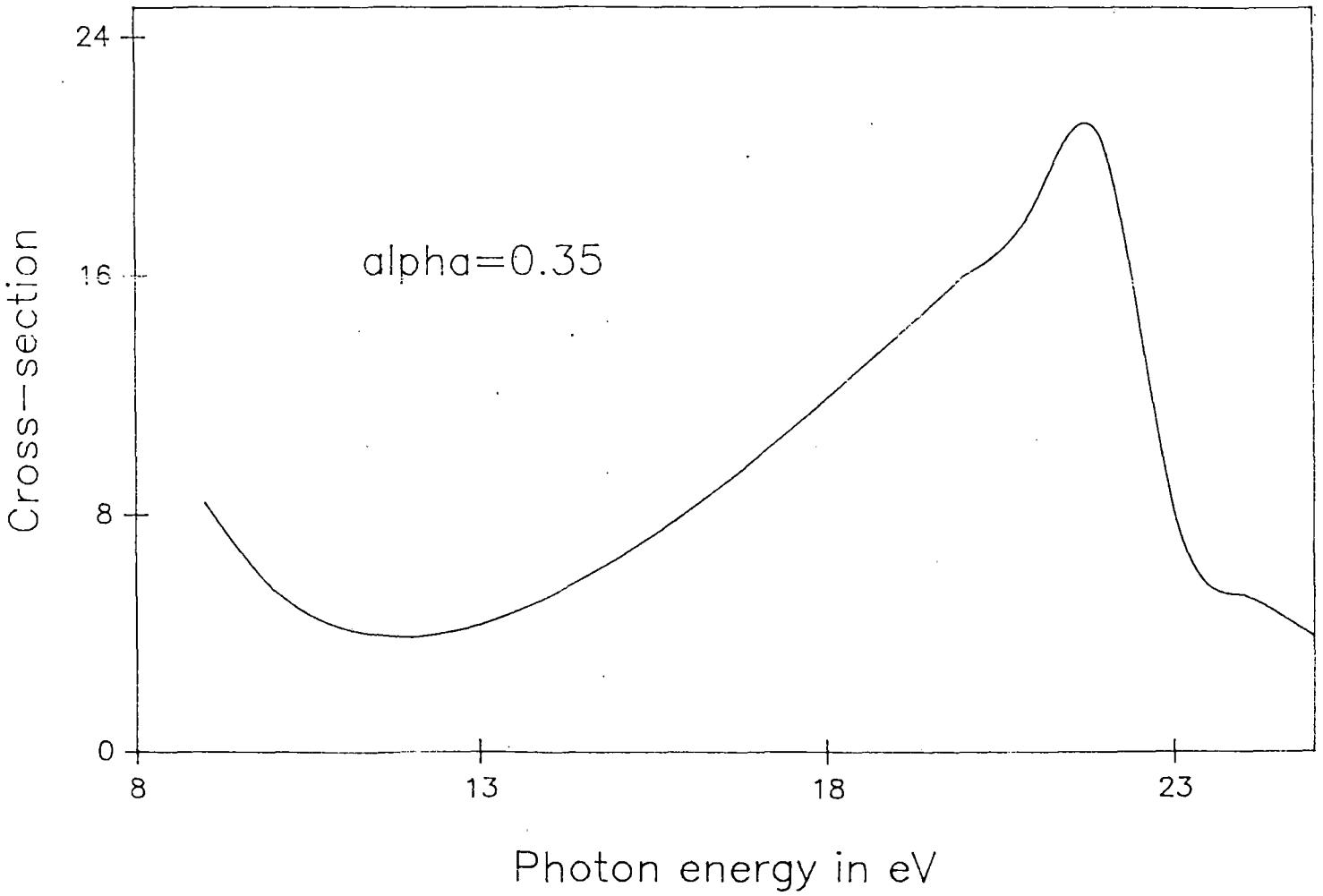

Fig 2.6 Photoemission cross-section (in arb. unit) for normal emission from Fermi level of aluminium with Fresnel fields

Levinson et al[20] and Barberan and Inglesfield[22] for aluminium. Kempa and others[21] have also considered the photoyield in terms of the hydrodynamical model and attributed the 12 ev peak to plasma waves. The calculations of Levinson et al, employing the self-consistent jellium model for fields in the surface region are more sophisticated and their results are in better agreement with the experimental data. However, the calculations for jellium can not be extended to more complicated cases, e.g., transition metals and semiconductors, while the model we have employed can be extended to these cases. So the qualitative agreement we obtain in aluminium and the previous application of the same model to the case of tungsten[33] gives us confidence to apply our model to photoemission calculations for other metals and semiconductors. However, for these cases, we can not use free electron wavefunctions any more.

In conclusion, although there are shortcomings in the model for electromagnetic field employed here (for example, since experimentally measured dielectric functions are used as inputs, the physical origin of the surface- related peak cannot be pin-pointed) -it gives results in reasonable agreement with experimental data, and has the potential of being used for a number of metals and semiconductors. In the next chapter, we shall combine a better description of the wavefunction with the field given by this model for photo-current calculations.

CHAPTER -III

Photoemission calculation with band initial state wavefunction

3.1 Introduction

In the last chapter we have seen that, a simple local model of dielectric function varying with the distance from the surface plane in the surface region gave us a reasonable description of the photocurrent as a function of photon energy for aluminium even with the free electron wavefunction for the initial and the final states. However, we know that we should include the crystal potential for the proper description of the metal - so that we should have the correct band structure and the density of states. In this chapter, we shall take a step in that direction - we shall consider the initial state as a proper band state. We shall describe the final state in the free electron form - although this is not the correct wavefunction. The reason for this is that the computational procedure even with the free electron final state becomes much more involved. We shall give the formalism first and we shall present numerical results for aluminium and show a comparison with the result of the previous chapter. The important results of this chapter have already been published[41].

As before, the main ingredient in the photocurrent calculation is the matrix element $\langle \psi_f | H' | \psi_i \rangle$ where $H' = (e/2mc)(\vec{A}.\vec{p}+\vec{p}.\vec{A})$. For the calculation of ψ_i, we shall assume the solid to be composed of layers parallel to the surface (Fig 3.1); further we shall assume that within each layer there is one atom per unit cell and the centres of all the atoms lie in the same plane parallel to the surface. We shall consider the crystal potential to be of muffin-tin form. For each layer we expand wavefunctions in the muffin-tin form and in the interstitial region, since the potential is constant the wavefunctions can be expanded into forward and backward travelling plane waves. With the centre of a muffin tin sphere in the layer chosen as origin, the

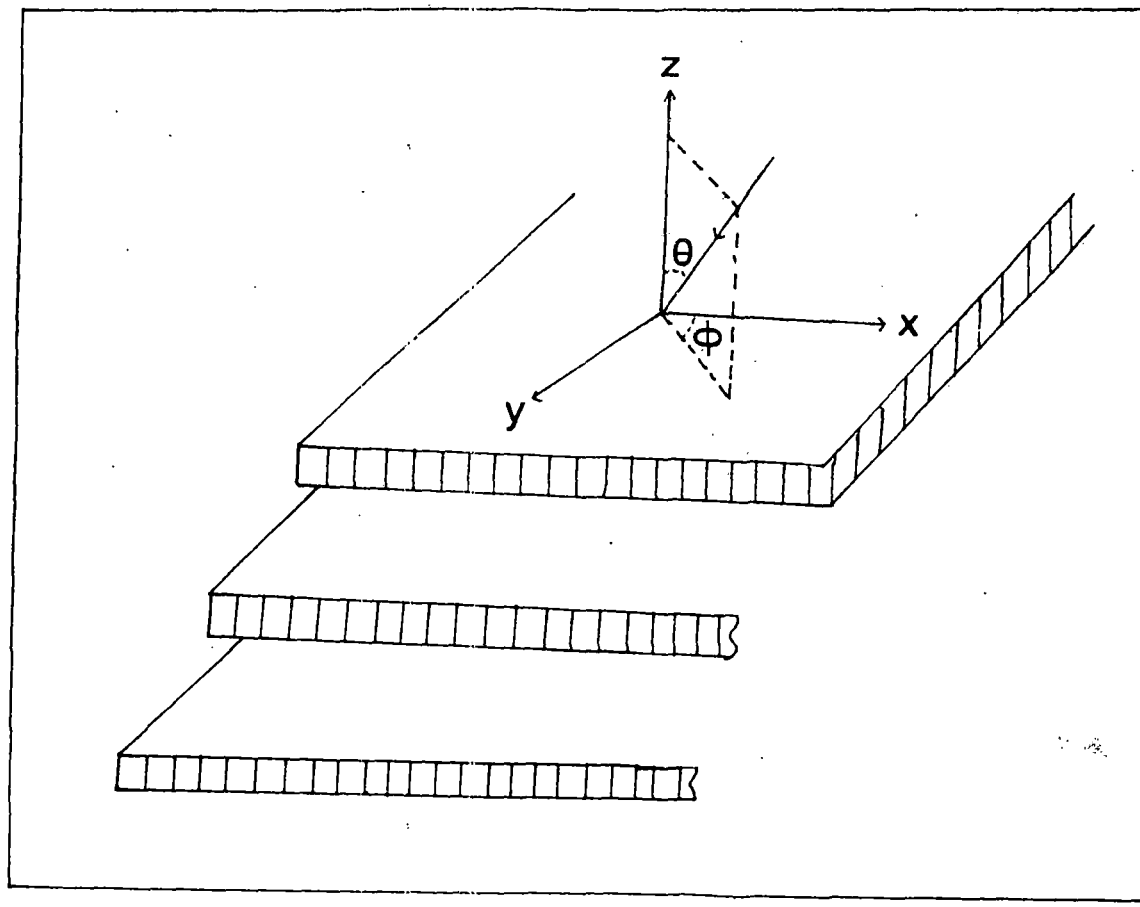

Fig 3.1 Schematic view of the crystal, considered as a stack of layers of atoms parallel to the surface

wavefunction may be written as:

$$\psi_i(\vec{r}) = \begin{cases} \sum_L A_{1L} f_{1l}(R)\, Y_L(\theta,\phi) & \text{spherical region} \\ \sum_{\vec{g}} [u_{\vec{g}} e^{i\vec{k}_{\vec{g}}^{+}\cdot\vec{R}} + v_{\vec{g}} e^{i\vec{k}_{\vec{g}}^{-}\cdot\vec{R}}] & \text{interstitial region} \end{cases}$$

$$\text{where, } \vec{K}_{\vec{g}}^{\pm} = \left[(\vec{k}+\vec{g})_{\parallel}, \pm\sqrt{2(E_i - V_0) - |\vec{k}+\vec{g}|_{\parallel}^2} \right], \quad \text{and} \quad \vec{R} = \vec{r} - \vec{c}_j \tag{3.1}$$

with the $\vec{g}$'s denoting two-dimensional reciprocal lattice vectors and $\vec{c}_j$ is the origin at the j-th layer. V_0 is the constant interstitial potential with respect to vacuum. To determine $u_{\vec{g}}$ and $v_{\vec{g}}$ an eigenvalue equation is constructed by using scattering properties of the layer and the Bloch condition, the solutions of which give the Bloch waves with the real and complex wave vectors. From these, the real Bloch waves propagating towards the surface are identified. $u_{\vec{g}}$ and $v_{\vec{g}}$ form the eigenvector for this Bloch wave. The construction of the eigenvalue equation is given in the appendix-I. The $u_{\vec{g}}$, $v_{\vec{g}}$'s corresponding to different layers are related by Bloch equation. This method is used in LEED type calculations and the details are given , for example, by Pendry[36]. The A_L's are determined from $u_{\vec{g}}$'s and $v_{\vec{g}}$'s by proper matching.

With the wavefunctions in each layer thus determined, one can write down the initial state wavefunction in the vacuum region as an exponentially decaying function

$$\psi_i(\vec{r}) = \sum_{\vec{g}} T_{\vec{g}} e^{i\vec{K}_{\vec{g}}\cdot(\vec{r}-\vec{r}_0)_{\parallel}} e^{-\chi_{\vec{g}}(z-z_0)} \quad \text{vacuum region}$$

$$\text{where,} \quad \chi_{\vec{g}} = \sqrt{-[2E_i - (k+\vec{g})_{\parallel}^2]} \tag{3.2}$$

and $z=z_0$ is the surface plane with respect to the origin in the first

layer. The coefficient $T_{\vec{g}}$ can determined by matching across the vacuum plane.

The final state ψ_f and the vector potential $\vec{A}$ are taken to be the same as in the last chapter. This means that we shall be considering p-polarized radiation in the long wavelength limit, and only the z-component (i.e., the one normal to the surface) will be considered. In addition, since in the description of the initial state the solid is divided up into layers, we shall consider the surface region to be equal to an integral number of layers. In what follows, we shall take the surface region to be the same as the first layer for calculational simplicity, but this may be extended to include more than one layer.

3.2 Matrix element calculation

We may now write down the matrix element for the solid as a whole

$$\langle \psi_f | H' | \psi_i \rangle = \int_{vac} \psi_f^* H' \psi_i \, d^3r + \int_{1st} \psi_f^* H' \psi_i \, d^3r + \sum_j \int_{bulk} \psi_f^* H' \psi_i \, d^3r \tag{3.3}$$

where, in each region the wavefunctions and vector potentials corresponding to that region have to be used.

i] Vacuum region

For this region form of the wavefunctions and the photon field are as follows

$$\psi_i(\vec{r}) = \sum_{\vec{g}} T_{\vec{g}} e^{i\vec{K}_g \cdot (\vec{r}-\vec{r}_0)} e^{-\chi_g (z-z_0)}$$

$$\psi_f(\vec{r}) = e^{i\vec{q} \cdot (\vec{r}-\vec{r}_0)} + \frac{q-k_f}{q+k_f} e^{-i\vec{q} \cdot (\vec{r}-\vec{r}_0)}$$

$$A_\omega(z) = A_1 \epsilon(\omega)$$

and the integration can be calculated analytically and the result is

$$T_1 = \int_{z_0}^{\infty} \psi_f^* \vec{A}_\omega . \vec{\nabla} \psi_i \, d^3 r$$

$$= -A_1 \epsilon \chi_0 T_0 S_0 \left[\frac{1}{\chi_0 + iq} + \frac{q - k_f}{q + k_f} \frac{1}{\chi_0 - iq} \right]$$

(3.4)

where, S_0 is the area of the surface unit cell. The integration for the parallel part becomes a δ-function from which we get only the contribution from the term $\vec{g}=0$.

ii] First (surface) layer

We have taken the width of the surface layer to be different from the other layers. This was done so that the metal-vacuum interface ($z=z_0$) can be taken to be tangential to the last layer of muffin-tin spheres as shown in fig 3.2. The form of the photon field in the surface layer is

$$A_\omega(z) = \frac{A_1 \epsilon(\omega)}{[1-\epsilon(\omega)]\,(\frac{z}{a}+\beta_1)} \quad \text{with} \quad \beta_1 = \frac{1}{[1-\epsilon(\omega)]} - \frac{z_0}{a}$$

In the factor β_1, which is similar to B_1 of the chapter-II, an additional term $(-z_0/a)$ comes due to the change in the position of the origin. Here we have taken the muffin-tin centre as the origin instead of the metal vacuum interface as considered in the previous chapter.

In each layer we shall calculate the matrix element for the interstitial and muffin-tin region separately.

The evaluations of the integral over the interstitial region is somewhat more complicated because of the shape of the region. To do it, we perform the integration over the cell (whole layer) and over the muffin-tin sphere, using the form for ψ_i for the interstitial region. Subtracting these two integrals we obtain the matrix element for

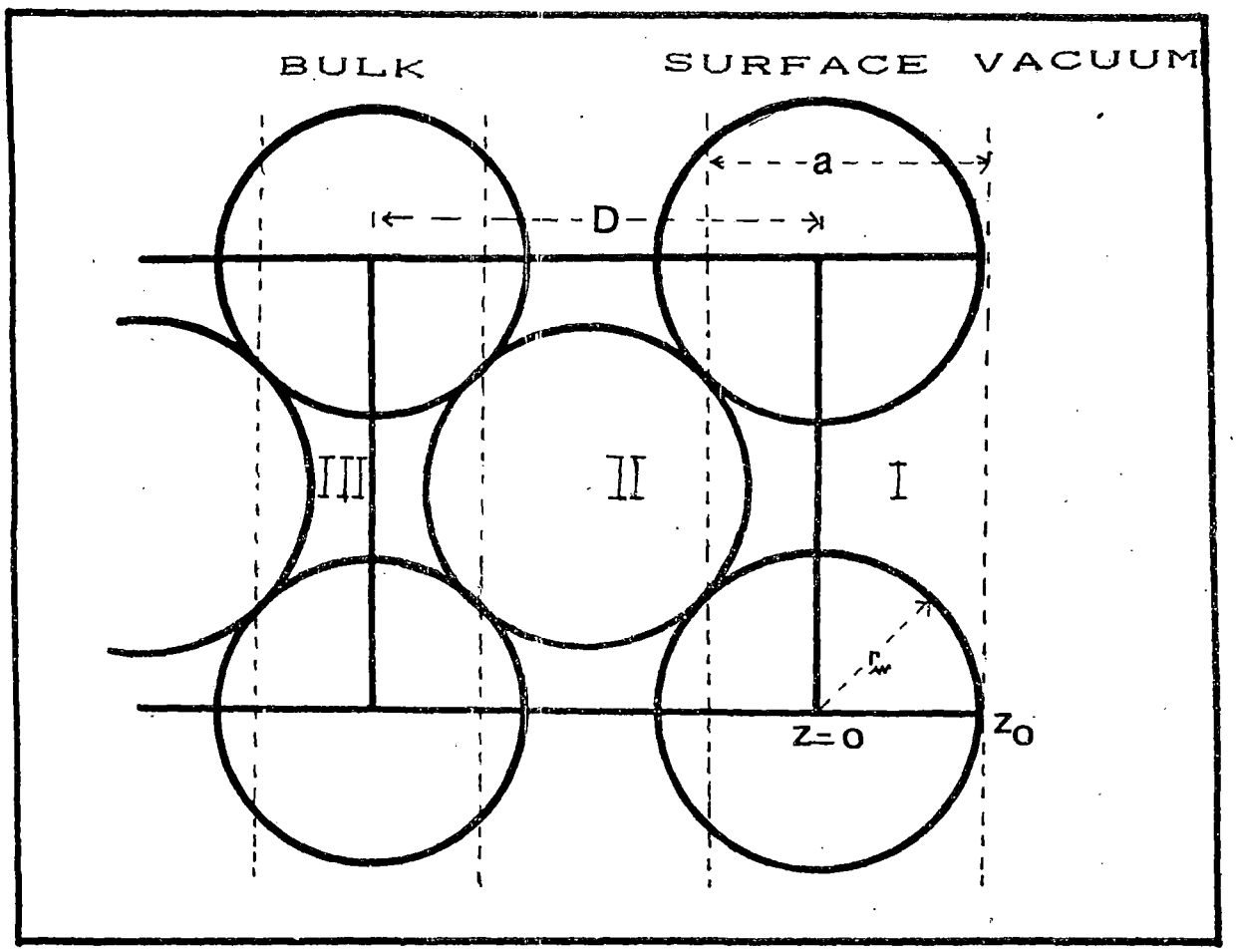

Fig 3.2 View of the muffin-tin potential at the surface of a solid

the interstitial region as given in the following equation

$$\int_{inst} \psi_f^* H' \psi_i d^3r = \int_{cell} \psi_f^* H' \psi_i d^3r - \int_{mft} \psi_f^* H' \psi_i d^3r$$

(3.5)

In the interstitial region the wave functions have the following form

$$\psi_f(\vec{r}) = \frac{2q}{q+k_f} e^{ik_f(\vec{r}-\vec{r}_0)}$$

$$\psi_i(\vec{r}) = \sum_{\vec{g}} \left[u_{\vec{g}} e^{ik_{\vec{g}}^+ \cdot \vec{r}} + v_{\vec{g}} e^{ik_{\vec{g}}^- \cdot \vec{r}} \right]$$

Using the above forms for the wave functions we calculate the integration over the cell as

$$T_2 = \int_{-\frac{D}{4}}^{z_0} \psi_f^* \left[\vec{A}_\omega \cdot \vec{\nabla} + \frac{1}{2} (\vec{\nabla} \cdot \vec{A}) \right] \psi_i d^3r$$

$$= p_1 S_0 \int_{-\frac{D}{4}}^{z_0} \left[\frac{iK_{\vec{g}z}^+}{\frac{z}{a}+\beta_1} \left\{ u_0 e^{iK_{\vec{g}fz}^+ z} - v_0 e^{iK_{\vec{g}fz}^- z} \right\} \right.$$

$$\left. - \frac{1}{2a(\frac{z}{a}+\beta_1)^2} \left\{ u_0 e^{iK_{\vec{g}fz}^+ z} + v_0 e^{iK_{\vec{g}fz}^- z} \right\} \right] dz$$

$$\text{where, } p_1 = \frac{2qA_1 \epsilon e^{i\vec{k}_f \cdot \vec{r}_0}}{(q+k_f)(1-\epsilon)} \text{ and } \vec{K}_{\vec{g}f}^{\pm} = \vec{K}_{\vec{g}}^{\pm} - \vec{k}_f$$

(3.6)

and D is the lattice constant.

For evaluating the integral over the muffin-tin sphere, we have to expand ψ_f , ψ_i and the z-component of the vector potential in spherical harmonics (or Legendre Polynomials). To express A_z and A_z' in

spherical coordinate, we write them in the following form

$$A_\omega(z) = A_\omega(r\cos\theta) = \frac{1}{\frac{r}{a}\cos\theta+\beta_1} = \sum_l B_l(r)\, P_l(\cos\theta)$$

$$\text{with } B_l(r) = \frac{2}{2l+1}\int_0^\pi A_\omega(r\cos\theta)\, P_l(\cos\theta)\sin\theta\, d\theta$$

$$\text{and } A'_\omega(z) = A'_\omega(r\cos\theta) = \frac{1}{\left(\frac{r}{a}\cos\theta+\beta_1\right)^2} = \sum_l D_l(r)\, P_l(\cos\theta)$$

$$\text{with } D_l(r) = \frac{2}{(2l+1)}\int_0^\pi A'_\omega(r\cos\theta)\, P_l(\cos\theta)\sin\theta d\theta$$

(3.7)

We have calculated these integrals analytically using the standard form of the integrations[42]. The details of the expressions for the radial part of the photon field $B_l(r)$ and $D_l(r)$ for different values of angular momentum l are given in the Appendix-I.

We calculate the matrix element in the muffin-tin region using the interstitial form for the initial state wavefunction given by

$$T_3 = \int_0^{r_m} \psi_f^* \left[\vec{A}_\omega . \vec{\nabla} + \frac{1}{2} (\vec{\nabla} . \vec{A}_\omega) \right] \psi_i \, d^3 r$$

$$= 8\pi p_1 \sum_{\vec{g},l} \frac{i^l}{2l+1} \Big[\Big\{ i K_{gz}^+ \int_0^{r_m} [u_{\vec{g}} P_l(K_p^+) j_l(|\vec{K}_{\vec{g}f}^+| r)$$

$$- v_{\vec{g}} P_l(K_p^-) j_l(|\vec{K}_{\vec{g}f}^-| r)] B_l(r) r^2 dr \Big\}$$

$$- \Big\{ \frac{1}{2a} \int_0^{r_m} [u_{\vec{g}} P_l(K_p^+) j_l(|\vec{K}_{\vec{g}f}^+| r)$$

$$+ v_{\vec{g}} P_l(K_p^-) j_l(|\vec{K}_{\vec{g}f}^-| r) D_l(r) r^2 dr \Big\} \Big]$$

$$\text{where, } K_p^\pm = \vec{K}_{\vec{g}f}^\pm . \hat{z}$$

(3.8)

and r_m being the muffin-tin radius. Here we have used the standard expansion

$$e^{i\vec{k}^\pm . \vec{r}} = 4\pi \sum_L i^l j_l(|\vec{K}^\pm| r) \, Y_L(\vec{r}) \, Y_L^*(\vec{K}^\pm)$$

(3.9)

and also the orthogonality properties of spherical harmonics.

The form for the initial state wave function inside the muffin-tin sphere is given by

$$\psi_i(\vec{r}) = \sum_L A_L f_l(r) \, Y_L(\theta, \phi)$$

and the calculated form of the matrix element over the muffin-tin sphere comes out to be

$$T_4 = \int_0^{r_m} \psi_f^* \left[\vec{A}_\omega . \vec{\nabla} + \frac{1}{2} (\vec{\nabla} . \vec{A}_\omega) \right] \psi_i \, d^3 r$$

$$= 8\pi p_1 \sum_{L_1, l_2, L_3} \frac{A_{L_3} (-i)^{l_1} Y_{L_1} (\vec{k}_f)}{2 l_2 + 1} \int_0^{r_m} \left[\left\{ C^1_{L_1 l_2 L_3} \left[\frac{\partial}{\partial r} f_{L_3} (r) \right] r^2 \right.\right.$$

$$\left.\left. + C^2_{L_1 l_2 L_3} f_{l_3} (r) \, r \right\} B_{l_2} (r) - \frac{1}{2a} C^3_{L_1 l_2 L_3} f_{l_2} (r) \, r^2 D_{l_2} (r) \right] j_{l_1} (k_f r) \, dr$$

(3.10)

Although the explicit form of the equations (3.8 & 3.10) are the same but we have used different form for ψ_i. In the above equation angular parts of the integration are given by

$$C^1_{L_1 l_2 L_3} = \int_\Omega Y_{L_1}^* \, Y_{L_3} \, P_{l_2} (\cos\theta) \cos\theta \, d\Omega$$

$$C^2_{L_1 l_2 L_3} = \int_\Omega Y_{L_1}^* P_{l_2} (\cos\theta) \left[\frac{\partial}{\partial \theta} Y_{L_3} \right] Sin\theta \, d\Omega$$

$$C^3_{L_1 l_2 L_3} = \int_\Omega Y_{L_1}^* P_{l_2} (\cos\theta) \, Y_{L_3} \, d\Omega$$

For further simplifications for these angular integrals we have used the recursion relations for the spherical harmonics.

Therefore, 1st layer contribution to the matrix element can be calculated from the terms T_2, T_3 and T_4 and equation (3.5) as $T_5 = T_2 - T_3 + T_4$

iii] Bulk layers

For the bulk layers we calculate the matrix element over the interstitial and muffin-tin region separately as we have done in the 1st layer. It is to be noted that the photon field is constant here given by

$$A_\omega (z) = A_1$$

and in the integration we have no term involving the variation A(z). In the bulk layers the calculations are simpler compared to that of the 1st layer and we have calculated some of terms analytically.

Term T_5 is the matrix element for the cell (whole layer) with the interstitial form for the initial state wavefunction, similar to the term T_2 of the 1st layer given by

$$T_5 = p_2 S_0 K_{gz}^{+} \left[\frac{u_0 \sin\left[K_{gfz}^{+} \frac{D}{4}\right]}{K_{gfz}^{+}} - \frac{v_0 \sin\left[K_{gfz}^{-} \frac{D}{4}\right]}{K_{gfz}^{-}} \right]$$

$$\text{where,} \quad p_2 = \frac{2iqA_1 e^{i\vec{k}_f \cdot \vec{r}_0}}{(q+k_f)}$$

(3.11)

Similarly, in the interstitial we calculate term T_6 which is identical to term T_3 of the surface layer

$$T_6 = 8\pi\sqrt{\pi} p_2 \sum_{g} K_{gz}^{+} \int_0^{r_m} \left[u_g j_0\left(|\vec{K}_{gf}^{+}|R\right) Y_0^{*}\left(\vec{K}_{gf}^{+}\right) \right.$$

$$\left. - v_g j_0\left(|\vec{K}_{gf}^{-}|R\right) Y_0^{*}\left(\vec{K}_{gf}^{-}\right) \right] R^2 dR$$

(3.12)

Calculation of the matrix element in the muffin-tin region is the same as in the surface layer (term T_4) and the result comes out to be

$$T_7 = p_3 \sum_{L_1 L_3} (-i)^{l_1} A_{L_3} Y_{L_1}(\vec{k}_f) \left[\int_0^{r_m} \left\{ C^4_{L_1 L_3} \left(\frac{\partial}{\partial R} f_{l_3}(R) \right) R^2 \right.\right.$$

$$\left.\left. - C^5_{L_1 L_3} f_{l_3}(R) R \right\} j_{l_1}(|\vec{k}_f| R)\, dR \right]$$

where, $$C^4_{L_1 L_3} = \int_\Omega Y_{L_1}^* Y_{L_3} \cos\theta \, d\Omega$$

$$C^5_{L_1 L_3} = \int_\Omega Y_{L_1 L_3}^* \left[\frac{\partial}{\partial \theta} Y_{L_3} \right] \sin\theta \, d\Omega$$

$$and \quad p_3 = -i p_2 8\pi^2$$

(3.13)

Similar to the surface layer the bulk contribution (using equation 3.5) is obtained from the relation $T_B = T_5 - T_6 + T_7$.

Using the values for the different terms T_S, T_B and $T_V (= T_1)$ we have calculated the photoemission cross-section numerically (using eqn.3.3) for which some portions of the FORTRAN programs are given in the appendix-III.

3.3 Results and discussion

We have applied our formalism to calculate normal photoemission cross-section from the Fermi level of aluminium and tungsten as a function of photon energy. For both the structures we have calculated the band structures where the imaginary part of the crystal potential has been taken to be zero. We have used some of the subroutines given by Pendry[36] and Hopkinson *et al* [43]. For the photon field calculation, data given by Weaver[35] for the complex dielectric function of aluminium and tungsten as a function of photon energy were used. The maximum value of the angular momentum L has been taken to be 4. Since the final state was taken to be free electron like a convergence factor of $\exp(-\alpha z)$ was

introduced in the final state to take into account the inelastic scattering of electrons.

The muffin-tin potential and the crystal parameters for aluminium are those given by Pendry[36]. We have taken[37] E_f=11.7 ev, V_0=15.95 ev and the lattice constant for aluminium as 4.05 A^0. In the figure (3.3), we show the result obtained for normal photoemission ($\vec{k}_{\parallel}$=0) for a p-polarised photon incident at 45^0 to the surface normal. The two curves shown correspond to two different values for the parameter '*a*' defining the surface region in the field calculation. The curve (I) is for '*a*' taken to be the same as the first layer while the plot (II) is for '*a*' equal to the first two layers. The scale for photocurrent for the two curves are not the same - we have plotted them so that the peaks around 11 ev are of comparable height. The value of α was taken to be 0.35 (the same value used earlier with free electron initial & final states in chapter-II).

The calculated photocurrent[41] shows a peak at 11.5 eV followed by a minimum at the plasmon energy (~16 eV) and a broad maximum around 20 eV. We have seen that these features are also present in the experimentally observed and previously calculated results[20,22] (fig. 2.3). In fig 3.4 we have compared the photocurrent variation against the photon field for the two types of crystal potential: muffin-tin (I) and free-electron (II). The scale of the photocurrent in the two curves are different but we have plotted them so that the peaks around 11 eV are of comparable height. Fig 3.4 shows that the ratio of the peak heights of the two peaks (below and above the plasmon energy) are of the order of 15 (free electron potential) and 3.6 (muffin-tin potential with a= thickness of first layer only) but in the experimental curve this ratio

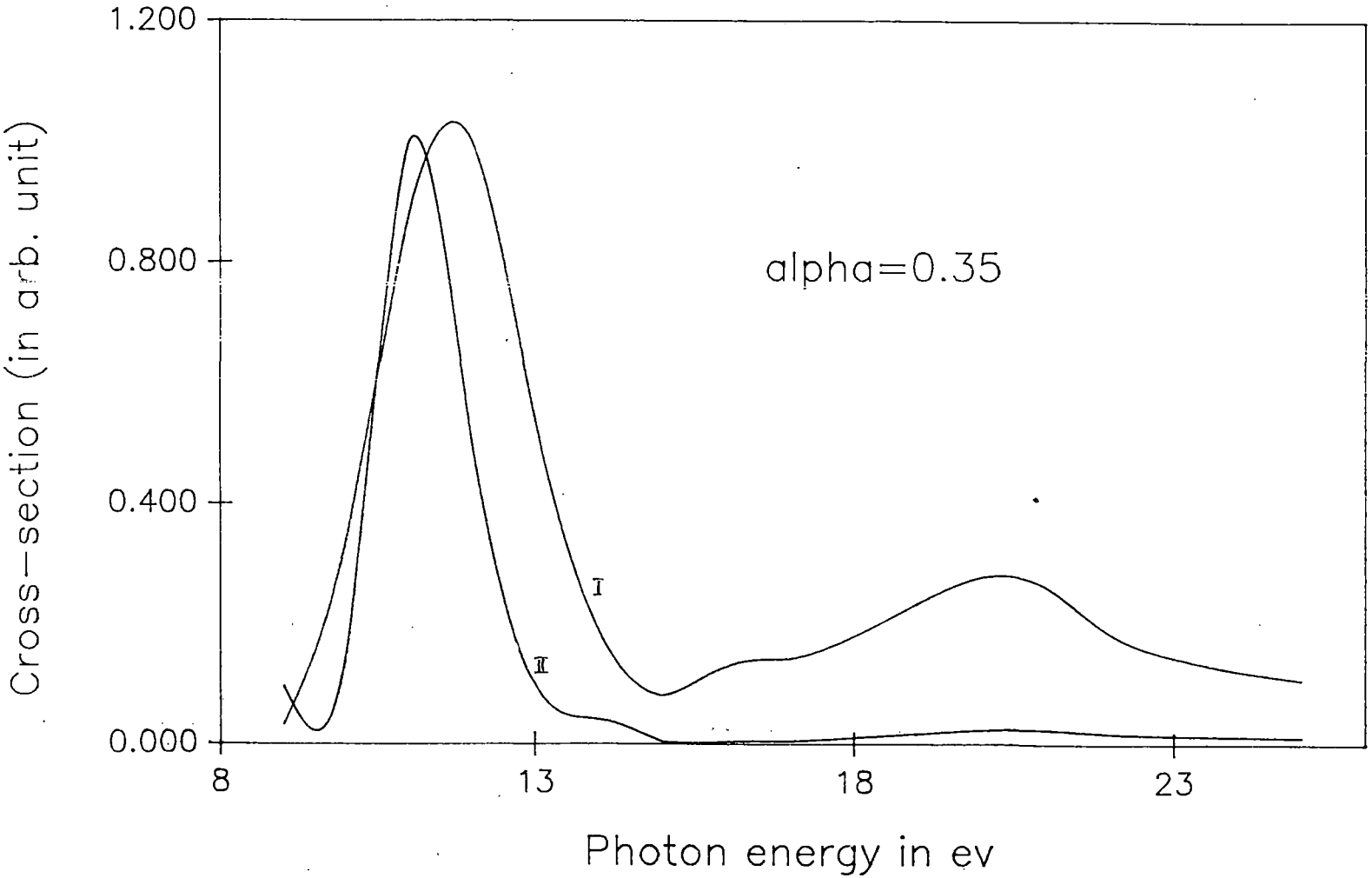

Fig 3.3 Calculated photocurrent against photon energy for normal emission from the Fermi level of aluminium (100) face with the surface region for field variation, a = thickness of the first layer (I) and first two layers (II)

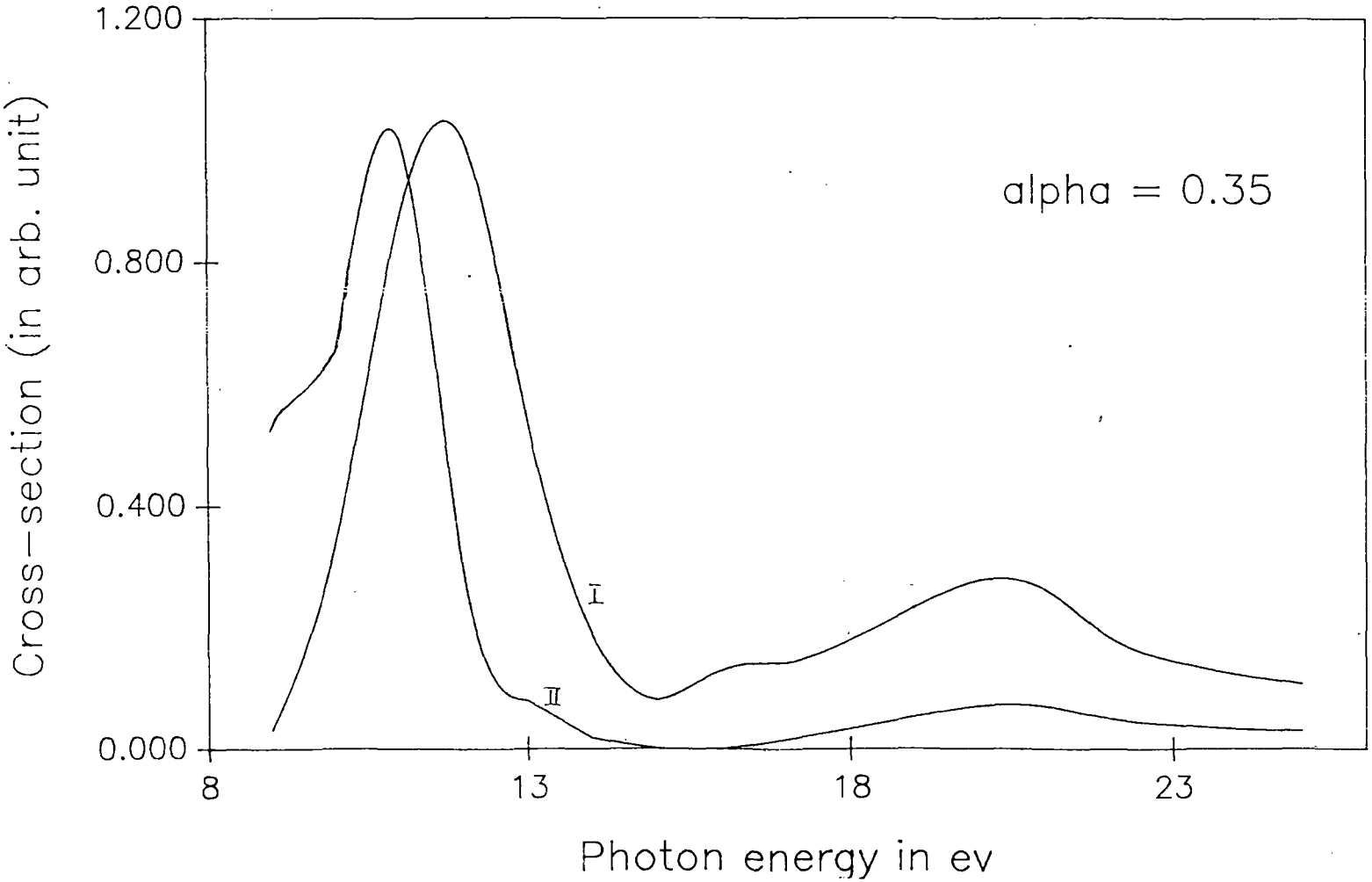

Fig 3.4 Photocurrent versus photon energy for two types: muffin-tin (I) and free-electron (II) potential for aluminium

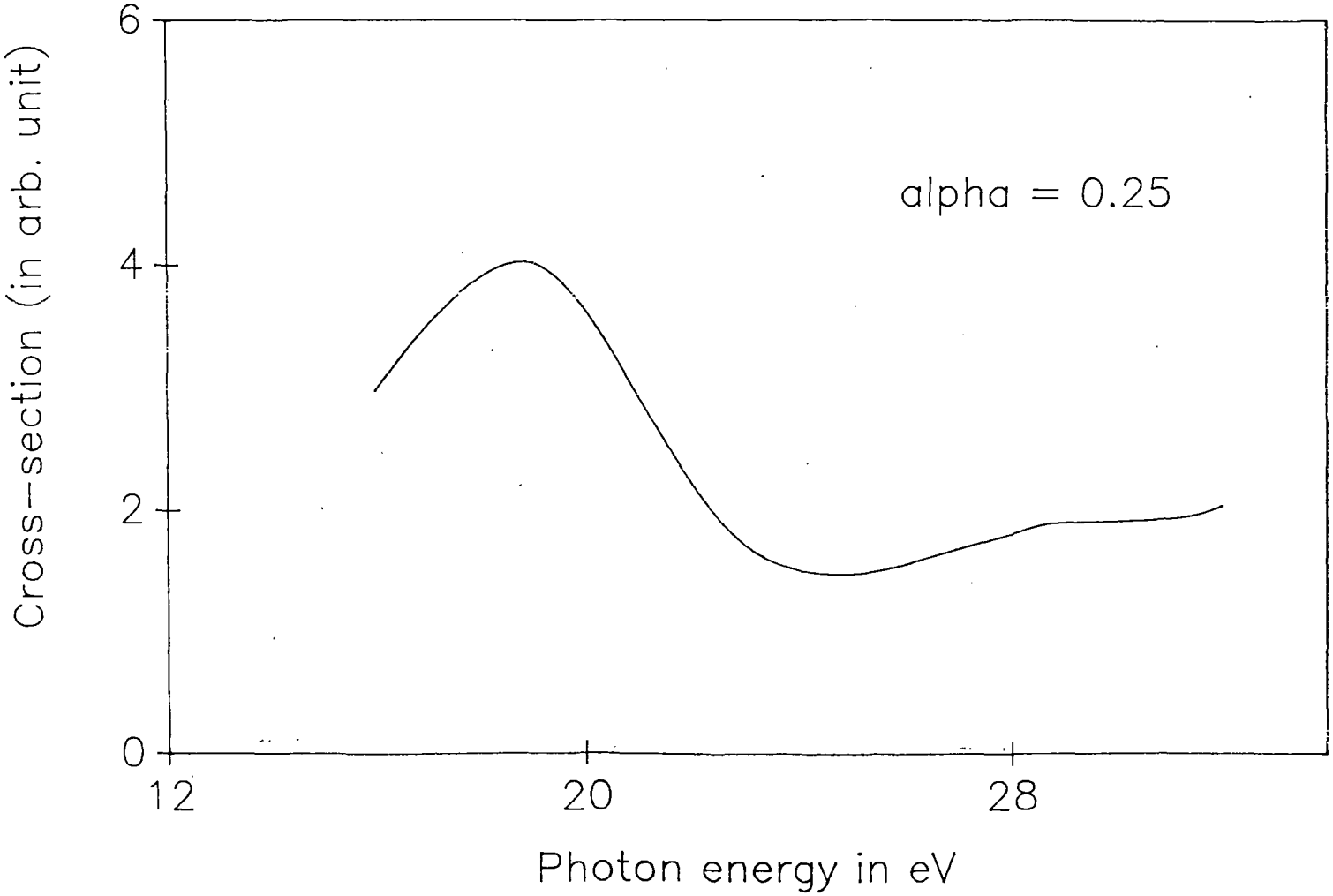

Fig 3.5 Photocurrent against photon energy for normal photoemission from tungsten (100) face

is of the order of 6. Again, if we consider *a* to be equal to the thickness of the first two layers this ratio comes out to be ~23 (curve II in fig 3.3). From the fig.3.3 it is evident that the field variation may be taken to be over the first layer only - at least with this model.

As a further application of our formalism we have considered a bcc lattice (tungsten). For the potential and the other crystal parameters of tungsten we have used the data given by Matheiss[44]. The lattice constant of tungsten is 3.16 A^{0}[37]. For the non-relativistic band structure as given by Matheiss[41], there is no Δ_1 at the Fermi energy, and it is known[42] that the only Δ_1 states can contribute to photocurrent for normal emission when p-polarised radiation is used. We have considered, the current from the Δ_1 band edge about 4 eV below the Fermi level.

Our calculated photoemission cross-section for tungsten as a function of photon energy (fig 3.5) shows a peak around 18 eV and a minima near the plasmon energy (24-25 eV), which is to be expected. It is also seen that the Δ_2 band at that energy makes a negligible contribution to current. However, for tungsten, relativistic spin-orbit effects are also important, so this calculation may be regarded as an example of calculation with bcc crystals.

So, we may conclude that use of band wavefunctions gives better agreement compared to previous calculations with free electron wavefunctions.

CHAPTER-IV

Photoemission calculation with LEED type final state wavefunction

4.1 Introduction

In this chapter, we shall give a formalism for photocurrent calculation where both the initial and final states are wavefunctions corresponding to the potential (in muffin-tin form) and the photon field is also included in the matrix calculation. We have already described how the initial state is constructed, so here we give a brief description of how to construct the final state. We shall be essentially following the method given by Pendry[28].

4.2 Final state wavefunction

If the electron coming to the detector is given by $e^{i\vec{q}.\vec{r}}$, then we consider an electron described by $e^{-i\vec{q}.\vec{r}}$ incident on the surface, and consider the scattering of this by the solid. In the vacuum region, wavefunction will consist of the incident wave and a set of scattered waves, which would be determined by the reflection matrix $R^{b}_{\vec{g}\vec{g}'}$ of the solid. We can also construct the wavefunction in each layer of the solid by starting from the vacuum side and going into the solid layer by layer - using the transmission and reflection matrices for that layer. We can then time reverse the wavefunction in the different regions to get the final state wavefunction.

The final state wavefunction may then be written, following Pendry

$$\sum_L A_{2L}^j e^{i\delta_{21}} f_{21}(R)\, Y_L(\theta,\phi) \quad \text{spherical region}$$

$$\psi_f(\vec{r}) = \sum_{\vec{g}} \left[W_{j\vec{g}}^{+} e^{i\vec{k}_{2\vec{g}}^{+}\cdot\vec{R}} + W_{j\vec{g}}^{-} e^{i\vec{k}_{2\vec{g}}^{-}\cdot\vec{R}} \right] \quad \text{interstitial region}$$

$$e^{i\vec{Q}\cdot(\vec{r}-\vec{r}_0)} + \sum_{\vec{g}'} R_{0\vec{g}'}^{b} e^{-i(\vec{q}_{\parallel}+\vec{g})\cdot(\vec{r}-\vec{r}_0)_{\parallel}} e^{-iQ_{g'z}(z-z_0)} \quad \text{vacuum region}$$

$$\text{where, } \vec{K}_{2\vec{g}}^{\pm} = \left[(\vec{K}_2+\vec{g})_{\parallel}, \pm\sqrt{2(E_i - V_0 + \omega) - |\vec{K}_2+\vec{g}|_{\parallel}^2} \right],$$

$$\vec{Q}_{\vec{g}'} = \left[(\vec{K}_2+\vec{g}')_{\parallel}, \sqrt{2(E_i+\omega) - (\vec{K}_2+\vec{g}')_{\parallel}^2} \right] \text{ and } \vec{q}^2 = 2(E_i+\omega)$$

(4.1)

Here j is the layer index and δ_{21} is the phase-shift corresponding to higher energy state. A^j_{2L} is amplitude of the spherical waves determined by multiple scattering at each layer. $W^{\pm}_{j\vec{g}}$ can be obtained layer by layer by propagating and reflecting the vacuum wavefunction. $R^b_{\vec{g}\vec{g}'}$ is the bulk reflection matrix can be obtained by layer doubling method. For the convergence of the layer doubling method an imaginary part is added to the muffin-tin potential. In our calcualtion subscripts 1 and 2 correspond to initial and final states.

4.3 Matrix element calculation

The matrix element is given by

$$T = \int \psi_f^{*} \left[\vec{A}_\omega \cdot \nabla + \frac{1}{2} (\nabla \cdot \vec{A}_\omega) \right] \psi_i \, d^3r$$

(4.2)

and we have to evaluate the integral all space. Since we have divided up the solid in layers - we shall assume that the surface region for photon field is the same as the first layer as we did in the last chapter. Then we can write the integral as a sum of a number of terms - where each term would correspond to the integral over a certain region

in space. This procedure is essentially the same as in the previous chapter - but the algebra gets to be more complex.

i] Vacuum region

The form of the initial and final state wavefunctions and the photon field at the vacuum region are given by

$$\psi_i(\vec{r}) = \sum_{\vec{g}} T_{\vec{g}} e^{i\vec{K}_{1\vec{g}\parallel}\cdot(\vec{r}-\vec{r}_0)_\parallel} e^{-\chi_{\vec{g}}(z-z_0)}$$

$$\psi_f(\vec{r}) = e^{i\vec{q}\cdot(\vec{r}-\vec{r}_0)} + \sum_{g'} R^{b}_{0\vec{g}'} e^{-i(\vec{q}_\parallel+\vec{g})\cdot(\vec{r}-\vec{r}_0)_\parallel} e^{-iQ_{g'z}(z-z_0)}$$

$$A_\omega(z) = h_1 \epsilon(\omega)$$

Here, h_1 is equal to A_1 of the previous chapter. Using these forms we can calculate the integration in the vacuum region analyticaly as

$$T_1 = \int_{z_0}^{\infty} \psi_f^* \vec{A}_\omega \cdot \vec{\nabla} \psi_i d^3r$$

$$= -S_0 \epsilon(\omega) h_1 \left[\frac{\chi_0 T_0}{\chi_0 + iq_z} + \sum_{\vec{g},\vec{g}'} T_{\vec{g}} R^{b*}_{0\vec{g}'} \frac{\chi_{\vec{g}}}{\chi_{\vec{g}} - iQ_{\vec{g}'}} \delta_{(2\vec{k}_{1\parallel}+\vec{g}+\vec{g}')} \right]$$

(4.3)

The parallel part of the integration appears as a δ-function which shows that there will be no contribution for small $\vec{k}_1$, unless $\vec{k}_1 = 0$ (normal emission).

ii] First layer (Surface region)

Photin field in the surface region is given by

$$A_\omega(z) = \frac{h_1 \epsilon(\omega)}{[1-\epsilon]\left(\frac{z}{a}+\beta_1\right)}$$

$$\text{with } \beta_1 = \frac{1}{[1-\epsilon(\omega)]} - \frac{z_0}{a}$$

The integration for this case is essentially the same as done for the corresponding term in the last chapter. We first perform the integration over the cell and then subtract the contribution from the muffin-tin sphere region, using the same interstitial form for both the initial and final states as follows (equation 3.5)

$$\int_{ist} \psi_f^* H' \psi_i d^3r = \int_{cell} \psi_f^* H' \psi_i d^3r - \int_{mft} \psi_f^* H' \psi_i d^3r$$

The form of the wavefunction for the initial and final states in the interstitial are given by

$$\psi_i(\vec{r}) = \sum_{\vec{g}} \left[u_{\vec{g}} e^{i\vec{k}_{1\vec{g}}^{+}.\vec{r}} + v_{\vec{g}} e^{i\vec{k}_{1\vec{g}}^{-}.\vec{r}} \right]$$

$$\psi_f(\vec{r}) = \sum_{\vec{g}} \left[W_{1\vec{g}}^{+} e^{i\vec{k}_{2\vec{g}}^{+}.\vec{r}} + W_{1\vec{g}}^{-} e^{i\vec{k}_{2\vec{g}}^{-}.\vec{r}} \right]$$

Since we have considered the first layer as the surface layer so, in this layer j is taken to be one.

To calculate the term T_2 for the integration in the interstitial region over the cell we start with the matrix element as

$$T_2 = \int_{-\frac{D}{4}}^{z_0} \psi_f^* \left[\vec{A}_\omega . \vec{\nabla} + \frac{1}{2} (\vec{\nabla} . \vec{A}_\omega) \right] \psi_i d^3r$$

$$= \frac{S_0 \epsilon h_1}{1-\epsilon} \sum_{\vec{g}} \int_{-\frac{D}{4}}^{z_0} \left[\left\{ \frac{iK_{1gz}^{+}}{\frac{z}{a}+\beta_1} - \frac{1}{2a\left(\frac{z}{a}+\beta_1\right)^2} \right\} \left\{ W_{1\vec{g}}^{*+} u_{\vec{g}} e^{i(K_{1\vec{g}}^{+} - K_{2\vec{g}}^{+})_z z} \right.\right.$$

$$\left. + W_{1\vec{g}}^{*-} u_{\vec{g}} e^{i(K_{1\vec{g}}^{+} - K_{2\vec{g}}^{-})_z z} \right\} - \left\{ \frac{iK_{1gz}^{+}}{\frac{z}{a}+\beta_1} + \frac{1}{2a\left(\frac{z}{a}+\beta_1\right)^2} \right\} .$$

$$\left. . \left\{ W_{1\vec{g}}^{*+} v_{\vec{g}} e^{i(K_{1\vec{g}}^{-} - K_{2\vec{g}}^{+})_z z} + W_{1\vec{g}}^{*-} v_{\vec{g}} e^{i(K_{1\vec{g}}^{-} - K_{2\vec{g}}^{-})_z z} \right\} \right] dz$$

(4.4)

where, S_0 is the area of the surface unit cell and D is the lattice constant. The integration over the parallel part becomes a δ-function from which we get only the contribution from term $\vec{g}=\vec{g}'$.

To evaluate the contribution of the muffin-tin region the initial and the final state (interstitial) wavefunctions are expanded in spherical form, using the standard expansion (3.9) and the spherical form (equation 3.7) for the photon field and the result is given by

$$T_3 = \int_0^{r_m} \psi_f^* \left[\vec{A}_\omega . \vec{\nabla} + \frac{1}{2}(\vec{\nabla} . \vec{A}_\omega)\right] \psi_i d^3 r$$

$$= \frac{8\pi\epsilon h_1}{1-\epsilon} \sum_{\vec{g},\vec{g}'} \sum_{L,L'} \frac{i^l C^6_{L,l'}}{2l'+1} \int_0^{r_m} \left[\left\{ iK^+_{1\vec{g}'z} D_{l'}(r) - \frac{B_{l'}(r)}{2a} \right\} . \right.$$

$$. \left\{ W^{*++}_{1\vec{g}} u_{\vec{g}'} Y_L(\vec{K}^+_{1\vec{g}'} - \vec{K}^+_{2\vec{g}}) \, j_l(|\vec{K}^+_{1\vec{g}'} - \vec{K}^+_{2\vec{g}}| r) \right.$$

$$\left. + W^{*-}_{1\vec{g}} u_{\vec{g}'} Y_L(\vec{K}^+_{1\vec{g}'} - \vec{K}^-_{2\vec{g}}) \, j_l(|\vec{K}^+_{1\vec{g}'} - \vec{K}^-_{2\vec{g}}| r) \right\}$$

$$- \left\{ iK^+_{1\vec{g}'z} D_{l'}(r) + \frac{B_{l'}(r)}{2a} \right\} .$$

$$. \left\{ W^{*-}_{1\vec{g}} v_{\vec{g}'} Y_L(\vec{K}^-_{1\vec{g}'} - \vec{K}^+_{2\vec{g}}) \, j_l(|\vec{K}^-_{1\vec{g}'} - \vec{K}^+_{2\vec{g}}| r) \right.$$

$$\left. \left. + W^{*-}_{1\vec{g}} v_{\vec{g}'} Y_L(\vec{K}^-_{1\vec{g}'} - \vec{K}^-_{2\vec{g}}) \, j_l(|\vec{K}^-_{1\vec{g}'} - \vec{K}^-_{2\vec{g}}| r) \right\} \right] r^2 dr$$

where $C^6_{L,l'} = \int_\Omega Y_L(\theta,\phi) \, P_{l'}(\cos\theta) \, d\Omega$

(4.5)

Next, we calculate the integration over the muffin-tin region using the following spherical wavefunction for both the initial and the final states

$$\psi_i(\vec{r}) = \sum_L A_{1L} f_{1l}(r)\, Y_L(\theta,\phi)$$

$$\psi_f(\vec{r}) = \sum_L A^j_{2L} e^{i\delta_{2l}} f_{2l}(r)\, Y_L(\theta,\phi)$$

Photon field has the same form as in interstitial region and in the atomic region form of the integration (T_4) would be

$$T_4 = \int_0^{r_m} \psi_f^* \left[\vec{A}_\omega . \vec{\nabla} + \frac{1}{2}(\vec{\nabla}.\vec{A}_\omega)\right] \psi_i d^3r$$

$$= \frac{2h_1\epsilon}{1-\epsilon} \sum_{L,L',L''} \frac{1}{2l''+1} A^{1*}_{2L} A_{1L'} e^{-i\delta_{2l}} \left[\int_0^{r_m} f_{2l}(r) \,.\right.$$

$$.\left\{D_{l''}(r)\left\{C^1{}_{L,L',L''} r^2 \left[\frac{\partial}{\partial r} f_{1l'}(r)\right] - C^2{}_{L,L',L''} r f_{1l'}(r)\right\}\right.$$

$$\left.\left. - \frac{C^3{}_{L,L'L''}}{2a} B_{l''}(r) f_{1l'}(r)\, r^2\right\}\right] dr$$

(4.6)

In the above equation C^1, C^2 and C^3 are the angular parts of the integration given by

$$C^1_{L,L',L''} = \int_\Omega Y^*_L Y_{L'} P_{L''}(\cos\theta)\cos\theta d\Omega$$

$$C^2_{L,L',L''} = \int_\Omega Y^*_L \left[\frac{\partial}{\partial\theta} Y_{L'}\right] \sin\theta P_{L''}(\cos\theta)\, d\Omega$$

$$C^3_{L,L',L''} = \int_\Omega Y_L{}^* P_{l''}(\cos\theta)\, Y_{L'} d\Omega$$

Using equation (4.4-6) for defferent terms T_2, T_3 and T_4 we can calculate the surface layer contribution to the matrix element as $T_S = (T_2 - T_3) + T_4$.

iii] Subsequent layers

For the bulk layers we calculate the integration over the

interstitial and muffin-tin region separately as we have done in the surfcae layer. It is to be noted that, the photon field is a constant here and in the integration we have no term involving the variation of A(z). In bulk layers the calculations are simpler than that of the 1st layer and we have calculated some of the integrations analytically.

Term T_5 is integration term over the whole cell with the interstitial form for both the initial and final state wavefunctions, similar to the term T_2 of surface layer given by

$$T_5 = \int_{-\frac{D}{4}}^{\frac{D}{4}} \psi_f^* \vec{A}_\omega . \vec{\nabla} \psi_i d^3R$$

$$= 2S_0 h_1 \sum_{\vec{g}} K_{1\vec{g}z}^{+} \Big[W_{f\vec{g}}^{*+} u_{\vec{g}} \frac{\sin[(K_{1\vec{g}}^{+} - K_{2\vec{g}}^{+})_z \frac{D}{4}]}{(K_{1\vec{g}}^{+} - K_{2\vec{g}}^{+})_z}$$

$$- W_{f\vec{g}}^{*+} v_{\vec{g}} \frac{\sin[(K_{1\vec{g}}^{-} - K_{2\vec{g}}^{+})_z \frac{D}{4}]}{(K_{1\vec{g}}^{-} - K_{2\vec{g}}^{+})_z} + W_{f\vec{g}}^{*-} u_{\vec{g}} \frac{\sin[(K_{1\vec{g}}^{+} - K_{2\vec{g}}^{-})_z \frac{D}{4}]}{(K_{1\vec{g}}^{+} - K_{2\vec{g}}^{-})_z}$$

$$- W_{f\vec{g}}^{*-} v_{\vec{g}} \frac{\sin[(K_{1\vec{g}}^{-} - K_{2\vec{g}}^{-})_z \frac{D}{4}]}{(K_{1\vec{g}}^{-} - K_{2\vec{g}}^{-})_z} \Big]$$

(4.7)

We again subtract off the contribution to this term from the muffin-tin region, using the spherical expansion of the exponential terms, as was done for term T_3

$$T_6 = \int_0^{r_m} \psi_f^* \vec{A}_\omega . \vec{\nabla} \psi_i d^3R$$

$$= 2\sqrt{\pi} i h_1 \sum_{\vec{g},\vec{g}'} K^+_{1\vec{g}'z} \Big[\int_0^{r_m} \Big\{ W^{*+}_{f\vec{g}} u_{\vec{g}'} Y_0(\vec{K}^+_{1\vec{g}'} - \vec{K}^+_{2\vec{g}}) \, j_0(|\vec{K}^+_{1\vec{g}'} - \vec{K}^+_{2\vec{g}}|R)$$

$$- W^{*+}_{f\vec{g}} v_{\vec{g}'} Y_0(\vec{K}^-_{1\vec{g}'} - \vec{K}^+_{2\vec{g}}) \, j_0(|\vec{K}^-_{1\vec{g}'} - \vec{K}^+_{2\vec{g}}|R)$$

$$+ W^{*-}_{f\vec{g}} u_{\vec{g}'} Y_0(\vec{K}^+_{1\vec{g}'} - \vec{K}^-_{2\vec{g}}) \, j_0(|\vec{K}^+_{1\vec{g}'} - \vec{K}^-_{2\vec{g}}|R)$$

$$- W^{*-}_{f\vec{g}} v_{\vec{g}'} Y_0(\vec{K}^-_{1\vec{g}'} - \vec{K}^-_{2\vec{g}}) \, j_0(|\vec{K}^-_{1\vec{g}'} - \vec{K}^-_{2\vec{g}}|) \Big\} R^2 dR \Big]$$

(4.8)

The contribution for the muffin-tin sphere region for such a layer can also be evaluated as for the surface layer (term T_4) with the further simplification that A is constant and may be written as

$$T_7 = \int_0^{r_m} \psi_f^* \vec{A}_\omega . \vec{\nabla} \psi_i d^3R$$

$$= h_1 \sum_{L,L'} A^{j*}_{2L} A_{1L'} e^{-i\delta_{21}} \Big[\int_0^{r_m} f_{21}(R) \, .$$

$$. \Big\{ \Big[\frac{\partial}{\partial R} f_{11'}(R) \Big] R^2 C^4_{L,L'} - C^5_{L,L'} f_{11'}(R) \, R \Big\} dR \Big]$$

(4.9)

The expression for angular parts of the integration are the following

$$C^4_{L,L'} = \int_\Omega Y_L^* Y_{L'} \cos\theta \, d\Omega$$

$$C^5_{L,L'} = \int_\Omega Y_L^* \Big[\frac{\partial}{\partial \theta} Y_{L'} \Big] \sin\theta \, d\Omega$$

Summing over the different terms T_5, T_6 and T_7 (eqn 4.7-9) we get the j-th layer contribution to the matrix element as $T_B^j = (T_5 - T_6) + T_7$.

The general expression for the photoemission cross-section in terms of $T_V (= T_i)$, T_S and T_B (using eqn. 1.1 & 3.3 in atomic unit) would be .

(4.10) $$\frac{d\sigma}{d\Omega} \sim \frac{k_f^2}{\omega} |T_V + T_S + \sum_j T_B^j|^2$$

The number of layers should be taken such that convergence is ensured. Application of our formalism to any real syatem can be done after the completion of the computation of photoemission cross-section.

This work has been accepted for publication in Modern Physics Letters B[23].

CHAPTER-V

Calculation of dipolar fields near the surface

5.1 Introduction

The local, or effective electric field for a polarisable infinite lattice has been studied for a long time (see for example, Born and Wolf[46]). Nijboer & Wette[47] (1958) evaluated the dipole field for both the cubic and non cubic (tetragonal, hexagonal, orthorhombic and monoclinic) lattices. They have considered a slab of dielectric material and obtained the dipole field by plane-wise summation. Using the same plane-wise summation method Kar & Bagchi[48](1978) calculated the dipole moment and the self-consistent local field near the surface of some cubic lattices. In this chapter, we consider three other structures, simple hexagonal, hexagonal close-packed (hcp) and diamond structure. The first two do not belong to the cubic system and so the Lorentz-Lorenz relation is not expected to hold (although, for the ideal hcp structure, the relation does hold); the Bravais lattice for the diamond structure is face-centred cubic, but the fact that there exists a two atom basis means that in addition to the atomic sites for the face-centred cubic structure there would be an equal number of atoms in other sites and the local field in the surface plane is quite different from the face-centred cubic case, as we shall discuss later.

The procedure for calculating the self-consistent local field is essentially the same as in ref 48; we have also used similar notations. A slab geometry of finite number of lattice plane have been considered - the lattice planes are assumed to be infinite, parallel to the surface. We have considered an electric field normal to the surface plane; the polarizability tensor was assumed to be diagonal; the molecules in each site would be polarised - these were taken as point dipoles - and all the dipoles lying in one plane would be parallel to one another and would have the same magnitude. The first step is to

compute the field from an infinite two-dimensional lattice of parallel dipoles of equal moment. This can be evaluated either by explicit sum within a finite region and approximating the rest by an integration with uniform dipole density[49] or by transforming the discrete lattice sum to a highly convergent sum analytically[47,50,51]. We have used the former technique to evaluate the two dimensional lattice sum. A major part of this work has already been published[52].

Let us denote different planes by the index ν and take $\vec{P}_\nu$ to be the local dipole moment density for the lattice plane ν. We shall consider $\nu=0$ to be the reference plane - positive values of ν denote planes with a positive value of z (above the reference plane) and negative ν values refer to planes below the reference plane. We shall consider an applied field $\vec{E}_0 = E_0\hat{z}$ in the z- direction. The field from the dipoles in the plane ν will depend linearly on $\vec{P}_\nu$ and the z-component of the total contribution of all the dipole fields may be written as

$$E_{d,z} = \sum_\nu \xi_\nu P_\nu \qquad (5.1)$$

where the sum over ν includes in principle all the planes in the slab we are considering and the coefficient ξ_ν has to be determined for each lattice structure. However, only a few of the ξ_ν's have non-zero values - at least to the accuracy we are concerned with.

We now consider a slab of L lattice planes. The local electric field at a lattice point in the μ-th plane, (μ=1,2, . . . L) may be written as

$$E^{\mu}_{loc,z} = E_0 + \sum_{\nu} \xi_{\mu-\nu} P_{\nu}$$

(5.2)

where the sum over ν is from 1 to L (although, in practice, only those terms for which ξ's are non-zero have to be retained).

Taking the volume polarisabilty to be Γ, the self-consistency condition for the local dipole moment density, given below

$$P_{\mu} = \Gamma E^{\mu}_{loc,z}$$

will yield the matrix equation

$$\sum_{\nu} M_{\mu\nu} P_{\nu} = \Gamma E_0 , \qquad \mu = 1, 2, \ldots L$$

$$\text{where } M_{\mu\nu} = \left[(1 - \Gamma\xi_0)\,\delta_{\mu\nu} - \Gamma\xi_{\mu-\nu}(1-\delta_{\mu\nu}) \right]$$

(5.3)

Inversion of the matrix M, where it is permissible, gives us the self-consistent dipole moment density on each plane; in particular, it would give the behaviour near the surface. Then, by using formula (5.2) we can compute the dipolar field on each plane.

In the following we shall consider the three structures - simple hexagonal, hexagonal close-packed and diamond, separately. In each case we shall give expressions for ξ and compute the self-consistent dipole moment and the dipolar field plane by plane. We shall also discuss the significance of the results obtained.

5.2 SIMPLE HEXAGONAL STRUCTURE

In fig. 5.1 we have shown a hexagonal close-packed structure where, the zero'th plane and the second (even) planes are the same for the simple hexagonal structure. For the simple hexagonal lattice, the sites in a plane with reference to an origin at a lattice point may be written as

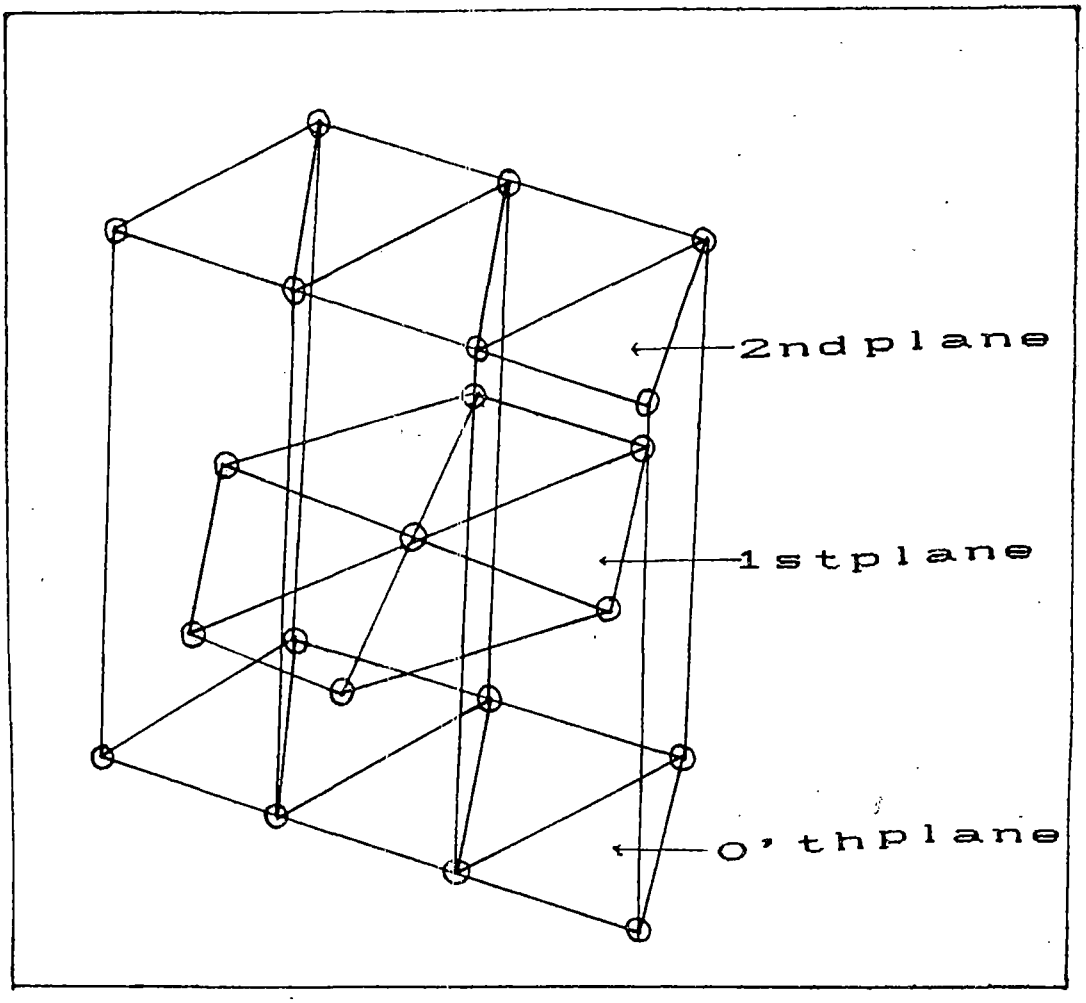

Fig 5.1 Schematic representation of hexagonal close-packed structure

$$\vec{R} = a\left[(n_1+\frac{n_2}{2})\hat{x}+\frac{\sqrt{3}}{2}n_2\hat{y}\right]$$

and for any other plane parallel to it, we may write

$$\vec{R} = a\left[(n_1+\frac{n_2}{2})\hat{x}+\frac{\sqrt{3}}{2}n_2\hat{y}+\alpha n_3\hat{z}\right]$$

where α=c/a and the surface is taken to be perpendicular to the z-axis. The electric field due to a dipole of moment $\vec{d}_i$ at point $\vec{r}_i$ is

$$\vec{E}_d=\sum_i' \frac{3(\vec{d}_i.\vec{r}_i).\vec{r}_i-r_i^2\vec{d}_i}{r_i^5}$$

(5.4)

If we consider $\vec{r}_i$ as the lattice vectors in the reference plane and noting that if $\vec{d}_\mu$ is the dipole moment for the dipole in the plane μ, then the dipole moment density for that plane $\vec{P}_\mu$ is

$$\vec{P}_\mu = \frac{2\vec{d}_\mu}{\sqrt{3}\alpha a^3}$$

Using equation (5.1 & 5.4) we can obtain the expression for ξ_0 as

$$\xi_0 = -(\frac{\sqrt{3}}{2}\alpha)\sum'_{n_1,n_2}\frac{1}{\left[n_1^2+n_2^2+n_1n_2\right]^{\frac{3}{2}}}$$

(5.5)

(the point $n_1=n_2=0$ is excluded)

Similarly, for the other planes we note that $\xi_\mu=\xi_{-\mu}$ and

$$\xi_\mu = (\frac{\sqrt{3}}{2}\alpha)\sum_{n_1,n_2}\frac{3n_3^2\alpha^2-\left[n_1^2+n_2^2+n_1n_2+\alpha^2n_3^2\right]}{\left[n_1^2+n_2^2+n_1n_2+\alpha^2n_3^2\right]^{\frac{5}{2}}}$$

(5.6)

with the plane index $\mu=n_3$, $n_3=1, 2, \ldots$ etc. The values of ξ_0, ξ_1, etc. calculated from equation (5.5-6) are shown in Table 1 for

Table 1: ξ_μ for various planes for simple hexagonal, hcp and diamond structure.

Plane Index μ	ξ_μ			
	Hexagonal	Hexagonal Close-Packed		Diamond
	a = 1.59	a = 1.63	a = 1.86	
0	-15.6046	-7.8023	-7.8023	-3.1939
1	0.0043	-0.2868	-0.1460	-2.0862
2	0.0000	0.0015	0.0003	-0.5054
3	0.0000	0.0006	0.0000	-0.0062
4	0.0000	0.0000	0.0000	0.0080
5	0.0000	0.0000	0.0000	0.0000

$a=1.59$ (this value is typical of simple hexagonal structures). These are in agreement with the previously computed values[47,51]. Further, to the accuracy we are interested in, it is necessary to take only ξ_0 and ξ_1 into account - so the sum in equation(5.2) would be restricted to $|\mu - \nu| \leq 1$.

We have also calculated[52] P_μ/P_b and E_μ/E_b (where P_b and E_b are the bulk values of the dipole moment and the dipole field) for a 21- layer film with a number of values of the volume polarizability Γ. In figure 5.2, we have plotted E_μ/E_b and P_μ/P_b for $\Gamma = -0.1$, but there is virtually no change if we take any other value of Γ. We have seen that 21 layers are enough to ensure convergence; actually, in this case convergence may be achieved even with a fewer number of layers. Except for a very small range near $\Gamma = -0.064$ for which the matrix cannot be inverted, the results look the same - with virtually no change at the surface plane for the dipole moment or the dipolar field. This is not unexpected - since we have seen that $|\xi_0/\xi_1| \sim 3.6\times10^3$, almost the entire contribution to the dipolar field comes from the in-plane dipoles - and so there is almost no variation in P_μ/P_b or E_μ/E_b from plane to plane.

5.3 HEXAGONAL CLOSE-PACKED STRUCTURE

For this structure, in addition to the lattice planes for the simple hexagonal case we have another set of planes halfway between the former ones as shown in Figure 5.1. The coefficient ξ_0 can be calculated using the same formula (5.5) as in the case of simple hexagonal structure, with an additional factor of 1/2 which comes in as there are now two atoms per unit cell. The original planes of the simple hexagonal lattice now become even numbered planes, and we may use equation (5.6) to calculate ξ_μ, with an additional factor of 1/2 with $\mu=2n_z$. For the odd-numbered planes we note that the sites may be denoted

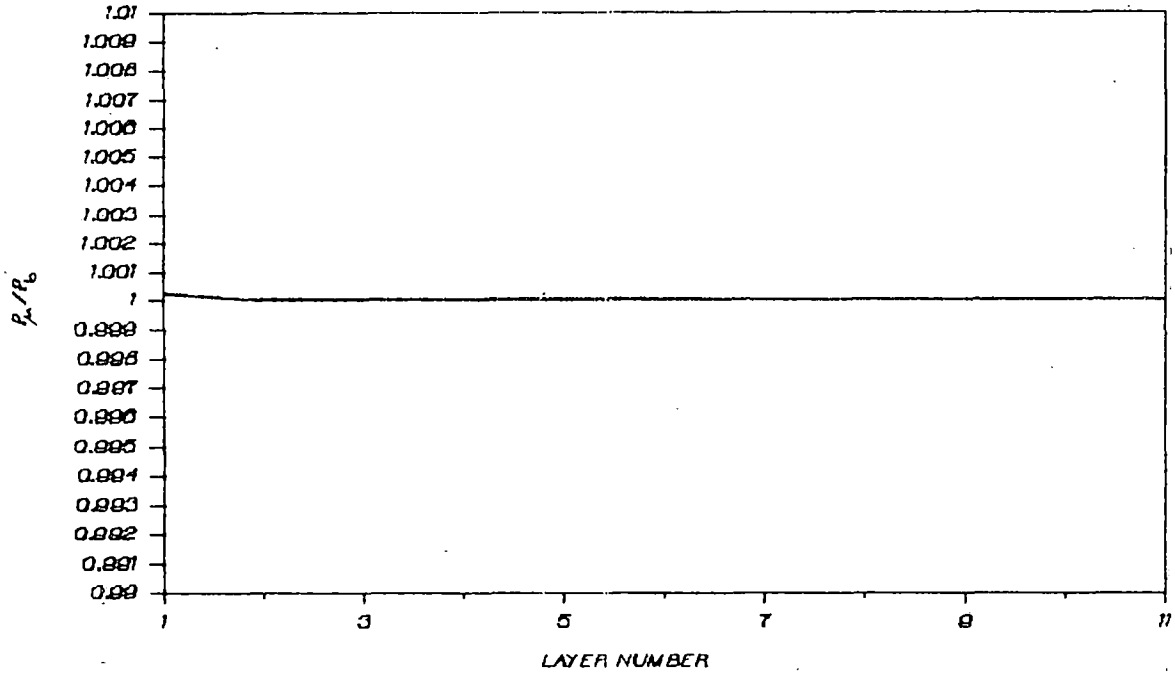

[a]

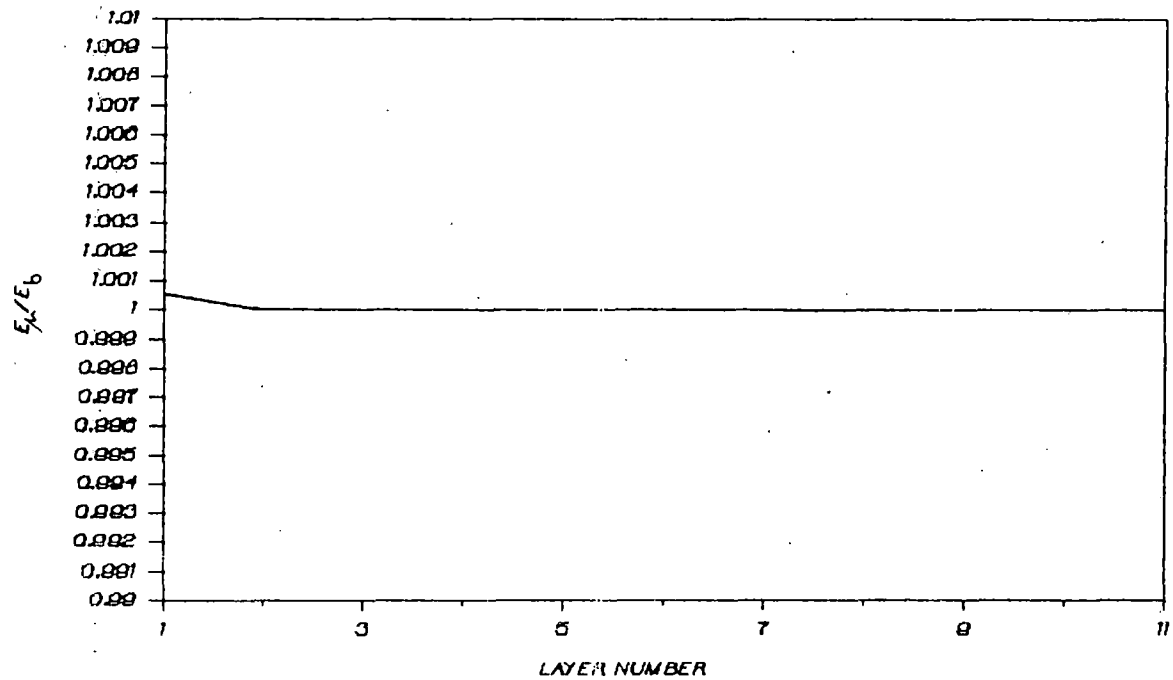

[b]

Fig 5.2 Variation of [a] ($P\mu/P_b$) and [b] ($E\mu/E_b$) against μ for Γ =-0.1 in simple hexagonal lattice

by the vectors

$$\vec{R} = (n_1+\frac{1}{3})\vec{a}_1 + (n_2+\frac{1}{3})\vec{a}_2 + (n_3+\frac{1}{2})\vec{a}_3$$

$$\text{with} \quad \vec{a}_1 = a\hat{x}, \; \vec{a}_2 = \frac{1}{2}a\hat{x} + \frac{\sqrt{3}}{2}a\hat{y}, \; \vec{a}_3 = c\hat{z}$$

We can then write, for odd planes

$$\xi_\mu = \frac{\sqrt{3}}{4}\alpha \sum_{n_1,n_2} \frac{3\alpha^2(n_3+\frac{1}{2})^2 - \left[(n_1+\frac{n_2}{2}+\frac{1}{2})^2 + \frac{3}{4}(n_2+\frac{1}{3})^2 + \alpha^2(n_3+\frac{1}{2})^2\right]}{\left[(n_1+\frac{n_2}{2}+\frac{1}{2})^2 + \frac{3}{4}(n_2+\frac{1}{3})^2 + \alpha^2(n_3+\frac{1}{2})^2\right]^{\frac{5}{2}}}$$

(5.7)

with $\mu = 2n_3+1$

In Table 1, we have shown the computed values of ξ_μ obtained from equation (5.5-7) for two values of α, 1.63 (corresponding to IDEAL HCP structure) and 1.86. For cubic symmetry, it is known that

$$\sum_\mu \xi_\mu = -\frac{8\pi}{3}$$

which gives the familiar Lorentz-Lorenz result. We note that for the ideal HCP structure also, this relation holds - although the symmetry is not cubic. For α=1.86 however, the sum over ξ_μ does not give $-8\pi/3$. This is perhaps another illustration of the close relationship between the face-centred cubic and ideal hexagonal close-packed structure.

For determining the dipole moment and the dipolar field in the surface region, we have taken a 21 layer slab and constructed the matrix M in equation (5.3) and inverted it to obtain the dipole moments $\vec{P}_\mu$ and the dipolar field, layer by layer. It may be mentioned here that taking 21 layer ensures convergence and increasing the number of layers does not change P_μ/P_b or E_μ/E_b, at least to the accuracy we are interested

in. For α=1.63, in figure 5.3, we show P_μ/P_b and E_μ/E_b for three values of Γ. Actually the points for integral values of μ are relevant - these points have been joined by lines for visual aid. Γ =-0.10 and Γ =-0.14 correspond to values of Γ just beyond the range for which the matrix **M** may not be inverted. For Γ =-0.14. i.e. just below the forbidden range, we see the maximum enhancement in the dipolar field for the surface layer - although the enhancement is not very large. The behaviour for both E_μ/E_b and P_μ/P_b is both oscillatory for this value of Γ - again the similarity of behaviour with face-centred cubic case[48] may be noted. For Γ =-0.10, just above the forbidden range and Γ =0.1, the variation in the dipolar field for the surface layer is smaller and the oscillatory behaviour is also absent. For α=1.86, we have plotted (fig 5.4) P_μ/P_b and E_μ/E_b for the same three values of Γ - and the behaviour is qualitatively the same - but the difference between the surface and bulk values for E_μ (or P_μ) is smaller than for the ideal case.

5.4 DIAMOND STRUCTURE

The diamond structure has the face-centred cubic lattice as the underlying Bravais lattice with a two atom basis. In this case we have, therefore, in addition to FCC lattice planes, an equal number of planes interspaced between these as shown in fig 5.5. Here, the expression for dipole moment density would be

$$\vec{P}_\mu = \frac{8\vec{d}_\mu}{a^3}$$

and for the reference plane,

$$\vec{R} = \frac{a}{\sqrt{2}}(n_1\hat{i}+n_2\hat{j})$$

ξ_0 is given by

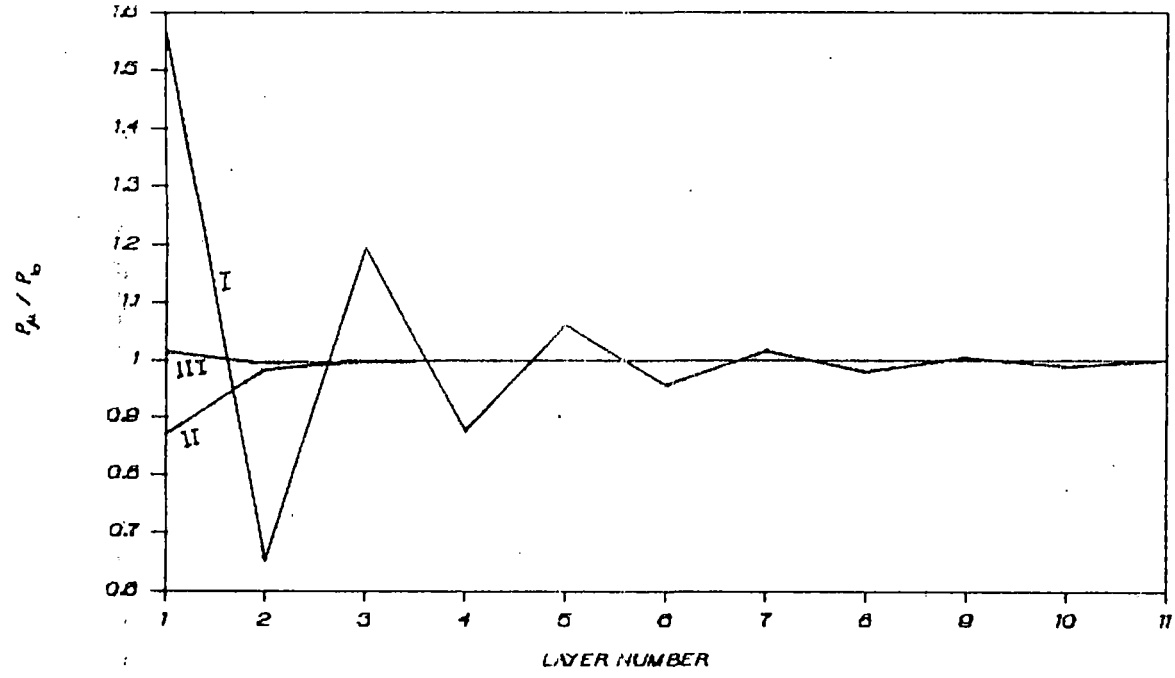

[a]

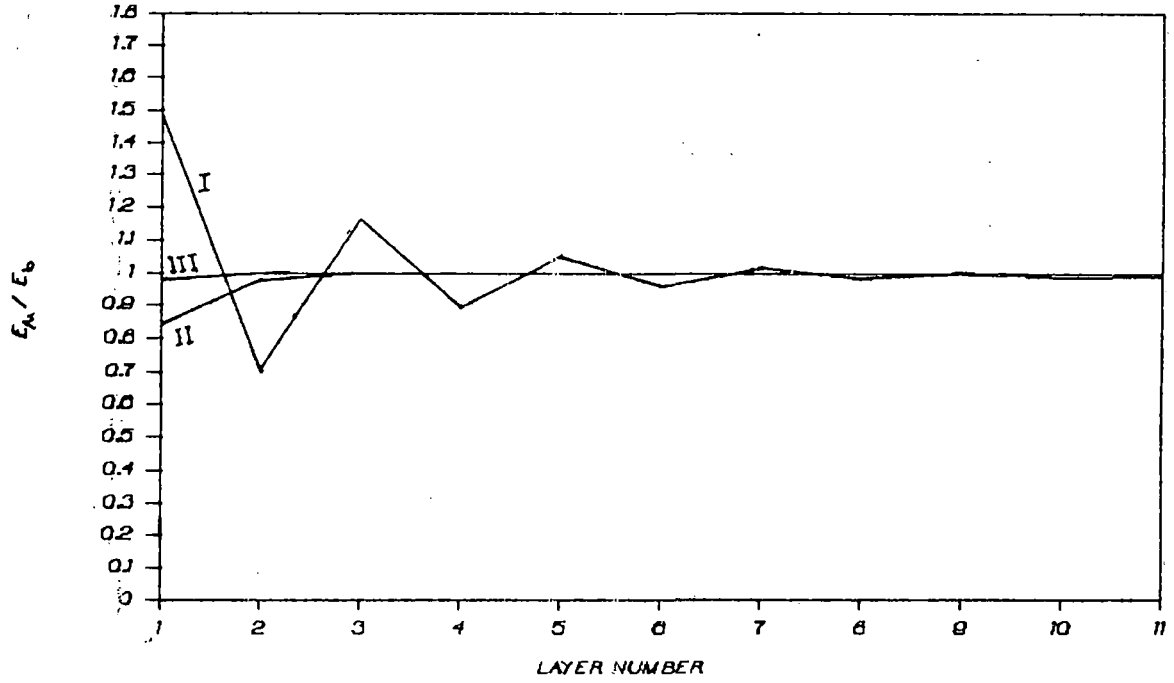

[b]

Fig 5.3 Variation of [a] $P\mu/P_b$ and [b] $E\mu/E_b$ against μ, for Γ =-0.14 (I), -0.1 (II) and 0.1 (III) in ideal hcp sturucture

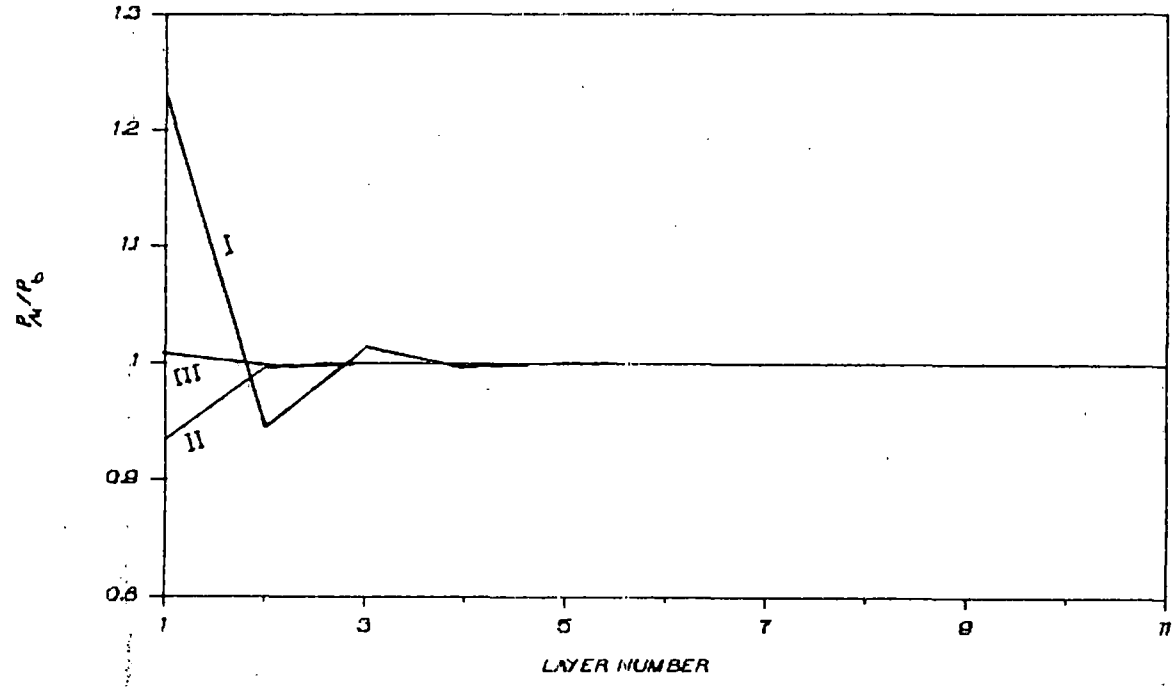

[a]

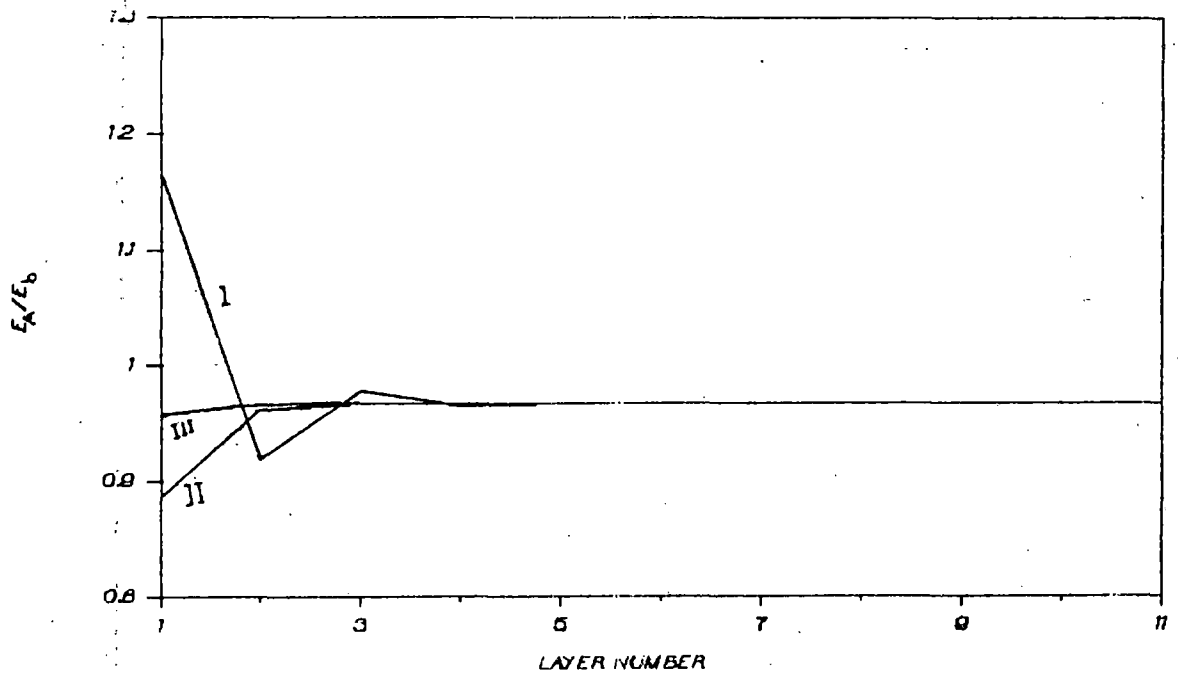

[b]

Fig 5.4 Variation of [a] $P\mu/P_b$ and [b] $E\mu/E_b$ against μ, for Γ =-0.14 (I), -0.1 (II) and 0.1 (III) in hcp structure with α=1.86

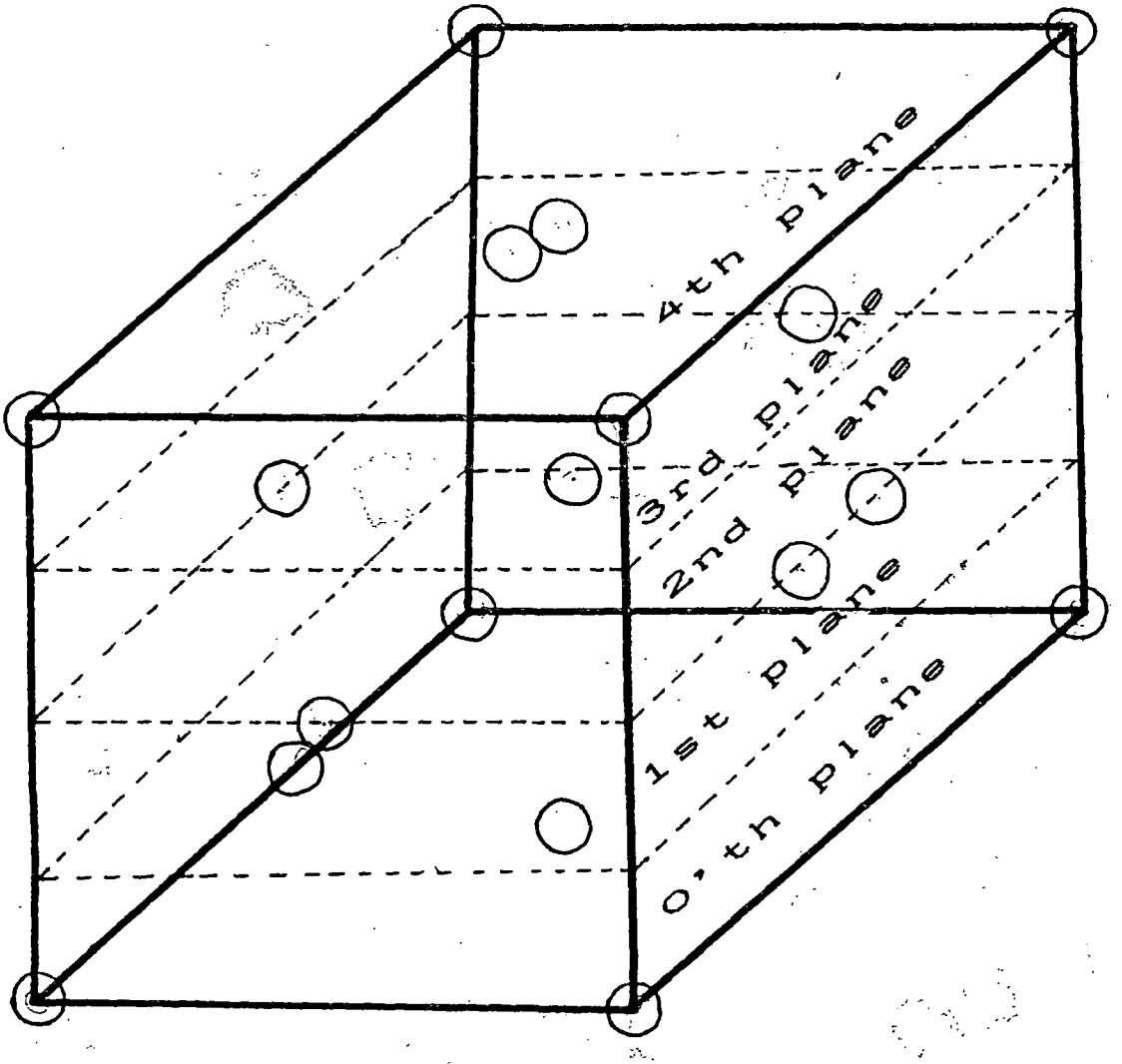

Fig 5.5 Schematic representation of diamond structure

$$\xi_0 = -\frac{1}{8}\sum\nolimits'_{n_1,n_2} \frac{1}{\left[\frac{1}{2}(n_1^2+n_2^2)\right]^{\frac{3}{2}}}$$

(5.8)

For planes located at distance (n+1/4)a from the reference plane (i,e. 1st plane, 5th plane etc.) i.e.,

$$\vec{R} = a\left[\frac{\hat{i}}{\sqrt{2}}n_1 + \frac{\hat{j}}{\sqrt{2}}(n_2+\frac{1}{2}) + \hat{k}(n_3+\frac{1}{4})\right]$$

we have

$$\xi_\mu = \frac{1}{8}\sum\nolimits_{n_1,n_2} \frac{3(n_3+\frac{1}{4})^2 - \left[\frac{n_1^2}{2} + \frac{1}{2}(n_2+\frac{1}{2})^2 + (n_3+\frac{1}{4})^2\right]}{\left[\frac{n_1^2}{2} + \frac{1}{2}(n_2+\frac{1}{2})^2 + (n_3+\frac{1}{4})^2\right]^{\frac{5}{2}}}$$

$$\text{with } \mu = 4n_3+1 \quad (n_3 = 0,1,2,\ldots)$$

(5.9)

For planes at distance (n+1/2)a from the reference plane (i.e. 2nd, 6th etc.) given by

$$\vec{R} = a\left[\frac{\hat{i}}{\sqrt{2}}(n_1+\frac{1}{2}) + \frac{\hat{j}}{\sqrt{2}}(n_2+\frac{1}{2}) + \hat{k}(n_3+\frac{1}{2})\right]$$

$$\xi_\mu = \frac{1}{8}\sum\nolimits_{n_1,n_2} \frac{3(n_3+\frac{1}{2})^2 - \left[\frac{1}{2}(n_1+\frac{1}{2})^2 + \frac{1}{2}(n_2+\frac{1}{2})^2 + (n_3+\frac{1}{2})^2\right]}{\left[\frac{1}{2}(n_1+\frac{1}{2})^2 + \frac{1}{2}(n_2+\frac{1}{2})^2 + (n_3+\frac{1}{2})^2\right]^{\frac{5}{2}}}$$

$$\text{with } \mu = 4n_3+2 \quad (n_3 = 0,1,2,..etc)$$

(5.10)

Similarly, for planes denoted by $\mu = 3,7,..$ etc

$$\vec{R} = a\left[\frac{\hat{i}}{\sqrt{2}}(n_1+\frac{1}{2}) + \frac{\hat{j}}{\sqrt{2}}(n_2+1) + \hat{k}(n_3+\frac{3}{4})\right]$$

$$\xi_\mu = \frac{1}{8}\sum_{n_1,n_2} \frac{3(n_3+\frac{3}{4})^2 - \left[\frac{1}{2}(n_1+\frac{1}{2})^2+\frac{1}{2}(n_2+1)^2+(\frac{3}{4}+n_3)^2\right]}{\left[\frac{1}{2}(n_1+\frac{1}{2})^2+\frac{1}{2}(n_2+1)^2+(\frac{3}{4}+n_3)^2\right]^{\frac{5}{2}}}$$

$$\text{with} \quad \mu = 4n_3+3 \quad (n_3 = 0,1,2,..)$$

(5.11)

and for planes denoted by $\mu=4,8$ ....etc.,

$$\vec{R} = a\left[\frac{1}{\sqrt{2}}(n_1\hat{i}+n_2\hat{j})+n_3\hat{k}\right]$$

$$\xi_\mu = \frac{1}{8}\sum_{n_1,n_2} \frac{3n_3^2 - \left[\frac{1}{2}(n_1^2+n_2^2)+n_3^2\right]}{\left[\frac{1}{2}(n_1^2+n_2^2)+n_3^2\right]^{\frac{5}{2}}}$$

$$\text{with} \quad \mu = 4n_3 \quad (n_3 = 1,2,...)$$

(5.12)

The even numbered planes are those in common with the FCC structure - the odd numbered planes are the new ones. As in the previous cases, here also $\xi_\mu = \xi_{-\mu}$; we give the values of ξ_μ in Table 1 and some portions of the computer programs are given in appendix IV. Again to the accuracy we are interested, only ξ_0, ξ_1, ξ_2, ξ_3, and ξ_4 (calculated from equation 5.8-12) have non-zero values - the rest of them can be taken to be zero. We note also that $\Sigma_\mu \xi_\mu = -8\pi/3$ (to 0.05 percent) as is to be expected, since diamond structure has cubic symmetry.

To determine the local field near the surface, we consider for this case a 33 layer slab - we take a larger number of layers as now there are more non-zero ξ_μ's and also because, in contrast to the other cases, the influence of the other two planes above and below the reference plane is comparable to the reference plane itself.

The results for the dipole moment density and the dipolar field obtained by inverting the matrix M also show (Fig.5.6) some interesting

results. There is a large range of Γ, from $-0.12(\sim -3/8\pi)$ to very large negative values, for which the inversion process breaks down. We have shown the results for Γ =-0.1 just above this range. We see the behaviour similar to the other cases - both P_μ/P_b and E_μ/E_b are less than one on the surface plane and monotonically goes to one as we go into the bulk. For large positive values of Γ, P_μ/P_b and E_μ/E_b behave in a different manner. We show in figure(5.6), the results for Γ =10. We see that P_μ/P_b has a large oscillatory behaviour. The first layer has a P_μ greater than twice the bulk value - while the second layer has a negative value - i.e. the dipole moment is in the direction opposite that of the bulk ! The dipolar field is also oscillatory - but the dipolar fields for the first and second layers are $0.98E_b$ and $1.01E_b$ - which is quite a contrast to the behaviour for the dipole moments. This can happen, because, as we have remarked above, the influence of the two neighbouring planes together is actually greater than that of the reference plane. The oscillations in P_μ are such that their total effect is to make the dipolar field for each layer remains almost the same. For Γ =0.5, the results shown in figure (5.6), are similar - but now the oscillations in P_μ/P_b are smaller. For values of Γ larger than 10, the oscillations grow larger and at some stage 33 layers are inadequate to achieve convergence. However, for the values of Γ shown in the Fig. 5.6 convergence was achieved with 33 layers. In fig 5.7 we show the polarisation for Γ=-0.18, where our method is not strictly valid, as no convergence can be achieved. It is clear from looking at the figure why convergence cannot be achieved - the almost perfect oscillatory behaviour is a strong indication that for this value of Γ a polarisation wave mode is supported by the system. However, our results for this value of Γ is only indicative, as our method is not formally valid for

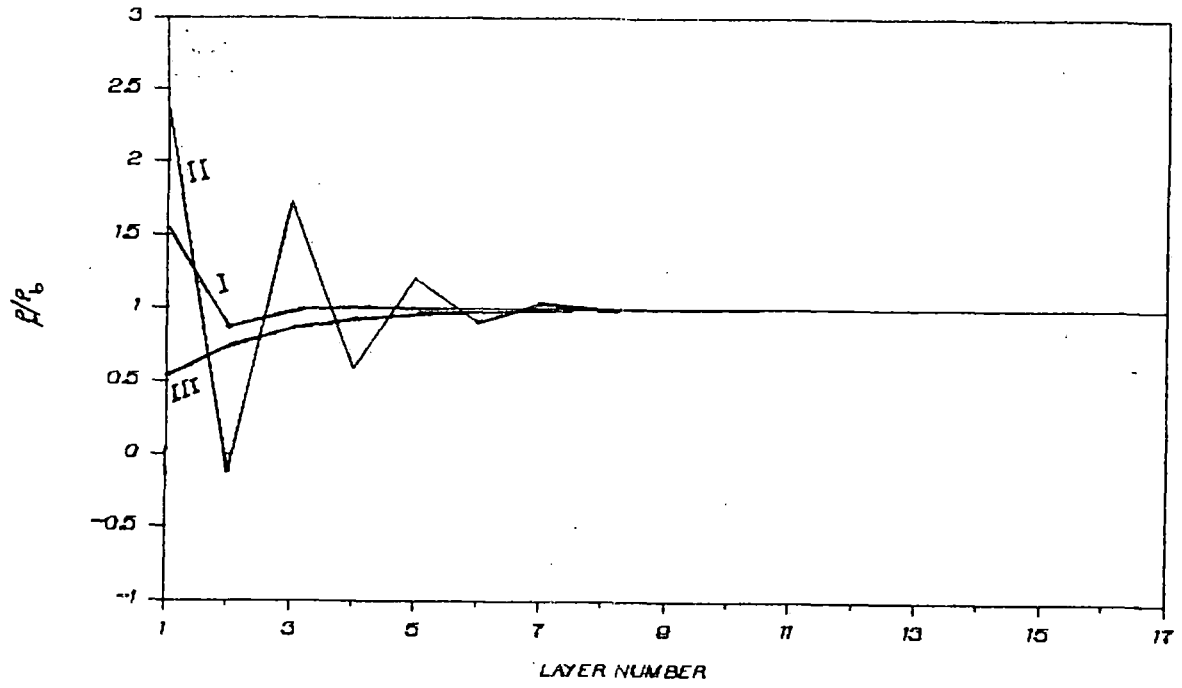

[a]

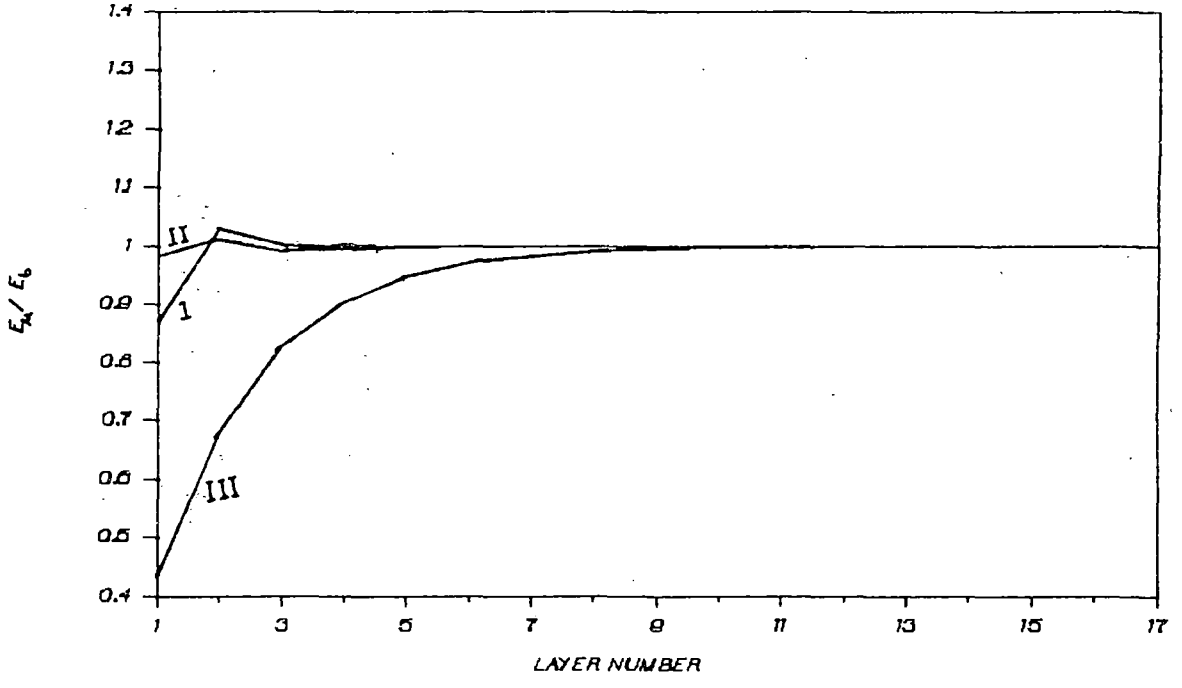

[b]

Fig 5.6 Variation of [a] $P\mu/P_b$ and [b] $E\mu/E_b$ againnst μ for Γ =0.5 (I), 10.0 (II) and −0.1 (III) in diamond structure

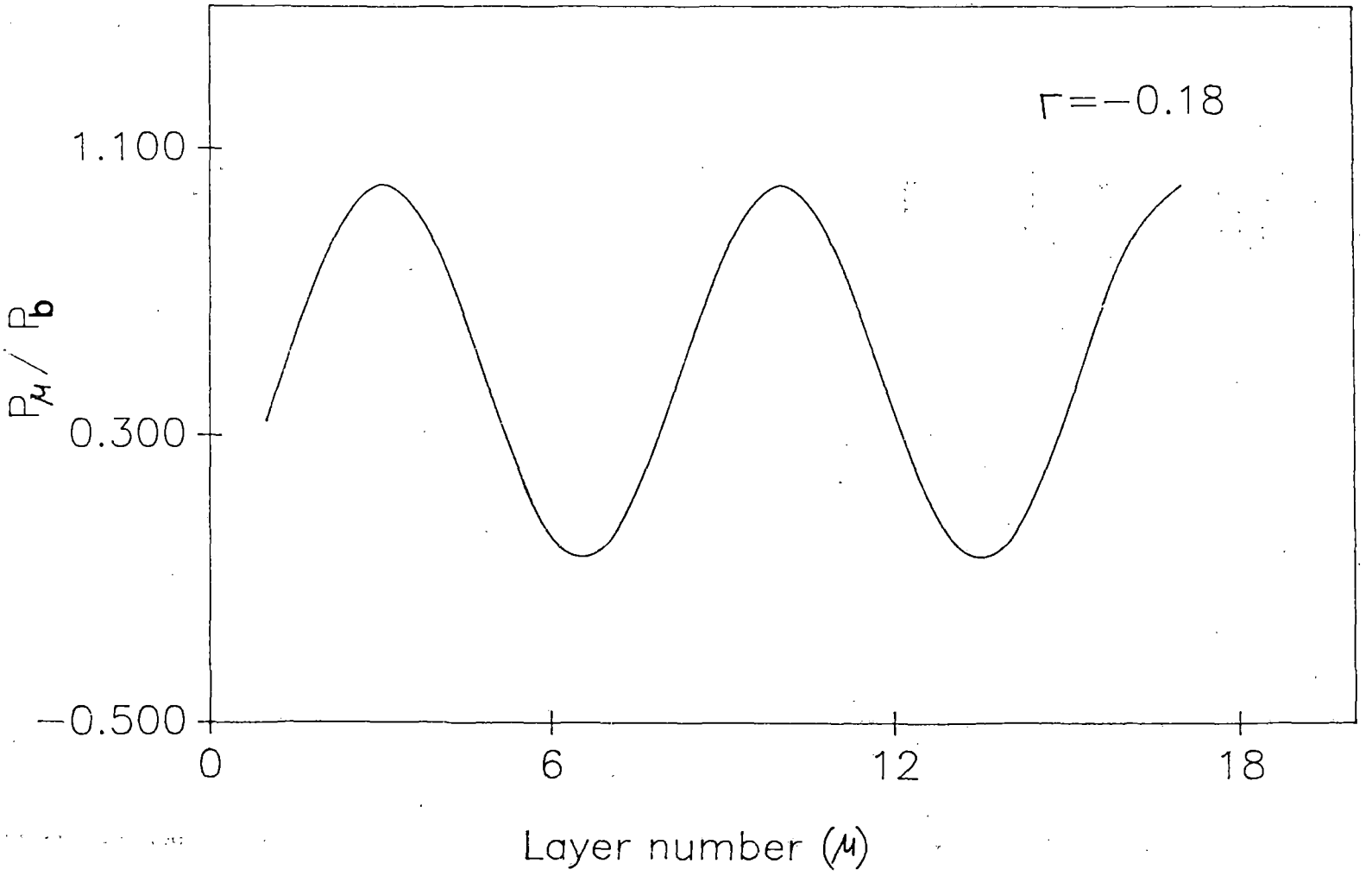

Fig 5.7 Variation of P_μ/P_b against μ in diamond structure for $\Gamma = -0.18$

$\Gamma<-0.12$.

The results for diamond structure are therefore, the most interesting ones. First, there is a large range of Γ for which our procedure breaks down - i.e., for these values of Γ the system can support spontaneous polarization modes. Second, for positive Γ values, we see large changes in dipole moment from layer to layer, but the dipolar field shows much smaller variation. We think that this behaviour can be traced to the fact $|\xi_1| \sim |\xi_0|$, in particular $|2\xi_1/\xi_0| > 1$, which again has its origin in the fact this interlayer spacing (a/4) is smaller than the distance of the in-plane nearest neighbour ($a/\sqrt{2}$).

5.4 Discussion

We have here considered three structures for which the self-consistent dipole moment density and the dipolar fields have been determined layer by layer. From a comparison of our results[52] along with those for the simple cubic, face-centred cubic and body-centred cubic systems, we are led to believe that for the structures (and for the crystallographic directions) for which the interplanar spacing becomes much smaller compared to the distance of the nearest neighbour in the plane, the behaviour of the dipole moment and the local field would be more interesting. However, in no case we have seen an enhancement in the dipolar field for the surface by an order of magnitude or more. This is consistent with the conclusions reached with the cubic structures. It may be mentioned that, our calculation was a formal one where we have considered all values of the polarizability - both positive and negative. We were interested to find whether any order of magnitude change in the local field takes place for the surface plane for any value of Γ. We did not consider any application to any real system - in which case only the positive values of the polarizability have physical

significance. This method may be used to study several phenomena e.g., light propagation near a semiconductor surface, importance of local fields in photoemission from insulators and adsorbate metals, etc.

CHAPTER VI

CONCLUSIONS

6.1 Summary and conclusions

Our main objective was to include the photon field variation in the photoemission calculation. For actual photoemission calculation, one has to calculate the initial and final sates involved in the matrix element (equation 1.1). The free electron potential model with a step potential functions at the surface was used for calculating the wavefunctions. We have used the simple model given by Bagchi & Kar[33] for the photon field at the surface. This model was employed for the case of aluminium for which the photocurrent from the Fermi level was calculated. The matrix element has been evaluated numerically and our results[38] show a reasonable agreement with experiment[20] and previous calculations[22] with other models for the fields. The results were analyzed for various values of the surface region, the decay length due to inelastic collisions etc., and the behaviour of the photocurrent as a function of photon energy was studied. It was observed that although some features of the calculated photocurrent (e.g., the minimum at the plasmon frequency were not sensitive to the length of the surface region, some other features (e.g., the ratio of the peak heights below and above the plasmon frequency) were sensitive to it. Also it appeared that even for a reasonable choice of the length 'a' of the surface region - the peak below the plasmon frequency was much sharper in our calculation than was obtained experimentally. However, for the proper description of the metal one has to include the crystal potential to get the correct band structure and the density of states. We have next considered the case of replacing the free electron initial state by a state where the crystal potential, in muffin-tin form was included. Normal photocurrent for the aluminium (100) face was again computed[41] and

compared with the experimental data as well as the free electron calculation. It seems that the results look better when the surface region for the photon field was taken to be the same as the first layer as compared to first two layers. this probably is an artifact of the model rather than the real situation.

We have also derived the formalism for considering both initial and final states in the presence of crystal potential in muffin-tin form. The calculation of these states are along the lines given by Pendry[28], but the presence of the spatially varying field makes the computation of the matrix much more involved. Numerical results for this calculation are not yet available. It may be mentioned here that, although we have used a particular form of the spatially varying photon field, any form of the photon field which is a function of z can be used in our photocurrent calculation. Also, our formalism to calculate photoemission cross-section is applicable to elements whose band structure can be computed with muffin-tin potential.

We have calculated[52] the self-consistent local dipole field near the surface of dipolar lattices. Here we have considered three different structures - the simple hexagonal, hexagonal close-packed and diamond. For the computation of the self-consistent local field we consider a slab geometry of a finite number of lattice planes parallel to the surface. We have carried out the dipole summation plane by plane parallel to the surface of the slab from any chosen origin inside the slab. We also calculated the dipole moment for each plane for three different lattice structures and compared with the experimental data. We have studied diamond structure in more detail and obtained some interesting features. In case of diamond, for some values of the volume polarizability the dipole moments show a oscillatory behaviour -

although the oscillations in the dipolar fields are small. The fields in the surface layer are somewhat different from the bulk local field except for the simple hexagonal structure. We have seen a close resemblance between hexagonal close-packed structure and the fcc structure in the calculation of dipole fields.

6.2 List of Publications

a)Journals:

i] Photoemission Calculation with a Simple Model for the Photon Field: Application to Aluminium ; P Das, R K Thapa & N Kar, *Mod. Phys. Lett.* B, 5 65 (1991) (copy enclosed)

ii] Dipolar Fields Near the Surface for Crystals with Simple Hexagonal, Hexagonal Close Packed and Diamond Structure ; P Das and N Kar; *Mod. Phys Lett.* B, 6 1263 (1992) (copy enclosed)

iii]Electromagnetic fields near metal surfaces; R K Thapa, P Das, N Kar & R A Lal; *Bull. Mat. Sci.* **16** 29 (1993)

iv] Photoemission Calculation with Kronig-Penney Model; R.K. Thapa, P. Das & N. Kar, Mod. Phys. Lett. B,8 361 (1994) (copy enclosed)

v] Photoemission Calculation Including Both Band Structure Effects and Photon Field Variation; P.Das and N.Kar; Phys. stat. sol. (b) **187**, 551 (1995) (copy enclosed)

b) Proceedings of Symposium/Seminar

i] Local field near the surface of a lattice with diamond structure: P Das & N Kar, *DAE Solid State Physics Symposium* 34C, 392 (1991)

ii] Photoemission calculation including both band structure effects and photon field variation ; P Das & N Kar, *DAE Solid State Physics Symposium* 34C, 393 (1991)

iii] Photoemission calculation with free electron wavefunctions and 'local' model of surface ; R K Thapa, P Das & N Kar, *DAE Solid State Physics Symposium* 32C, 396(1989)

iv] Frequency-dependent photoemission from aluminium using a simple dielectric model ; R K Thapa, P Das & N Kar, (Presented at the Young Physicists' Colloquium 1990), *Physics Teacher*, **33** 21 (1991)

v] Photoemission from the surface of silicon using a simple local dielectric model ; R K Thapa, P Das & N Kar, *Proceedings of Conference on Physics and Technology of Semiconductor Devices and Integrated Circuits*, 5-7 Feb'1992, page-318-20.

vi] Photoemission Calculation Including Photon Field variation In The Surface Region; P.Das, DAE SSP symposium'93, **36C** 46 (1993)

vii] Photoemission Calculation from the Fermi Level of Aluminium; P.Das, R.K.Thapa & N.Kar, DAE SSP symposium'93, **36C** 485 (1993)

6.3 References

1. H Hertz, *Ann. Physik* 31 983 (1887)

2. A Einstein, *Ann. Physik* 17 132 (1905)

3. D R Penn, *Phys. Rev. Lett.* 28 1041 (1972)

4. D D Koelling, G Arbman, *J Phys.* F5 2041 (1975)

5. P M Haltham *et al*, *J Phys* F7 635 (1977)

6. H L Skriver, *Phys. Rev.* B14 5187 (1976) & B15 1894 (1977)

7. J P Jan *et al*, *J Phys.* F7 957 (1977)

8. R V Kasowski, *Phys. Rev.* B8 1378 (1973), *Phys. Rev. Lett.* 33 83 (1974), *Solid. St. Commun.* 14 103 (1974) & 17 179 (1975)

9. O Jepsen, *Phys. Rev.* B12 2988 (1975)

10. O Jepsen *et al*, *Phys. Rev.* B12 3084 (1975)

11. G D Mahan, *Phys. Rev.* B2 4332 (1970), *Phys. Rev. Lett.* 24

12. I Adawi, *Phys. Rev.* 134 A788 (1964)

13. N W Ashcroft & W L Schaich, *Solid St. Commun.* 8 1959 (1970), *Phys. Rev.* B3 2452 19 (1971)

14. J G Endriz, *Phys. Rev.* B7 3464 (1973)

15. K Mitchell, *Proc. R. Soc.* A 146 442 (1934), *Proc Camb. Philos. Soc.* 31 416 (1935)

16. R E B Makinson, *Proc. R. Soc.* A 162 367 (1937)

17. K L Kliewer, *Phys. Rev. Lett.* 33 900 (1974) *Phys. Rev.* B14 1412 (1976)

18. T Maniv & H Metiu, *Phys. Rev.* 22 4731 (1980),

19. P J Feibelman, *Phys. Rev.* B12 1319 (1975), *Phys Rev. Lett.* 34 1092 (1975)

20. H J Levinson, E W Plummer & P J Feibelman, *Phys. Rev. Lett.* 43 953 (1979); *J. Vac. Sci. Technol* 17 216 (1980)

21. K Kempa & F Forstman, *Surf Sci.* **129** 516 (1983); K Kempa & R R Gerhardts, *Sol. State Comm.* 53 579 (1985)

22. N Barberan & J E Inglesfield, *J. Phys.* **C 14** 3114 (1981)

23. B C Meyers & T E Feuchtwang, *Phys. Rev.B* **27** 2030 (1983)

24. J T Lee & W L Schaich, *Phys. Rev. B* **38** 3747 (1988)

25. N D Lang & W Kohn, *Phys. Rev.* B1 4555 (1970)

26. G Mukhopadhay & S Lundsqvist, *Physica Scripta* **17** 69 (1978)

27. A Liebsch, *Phys. Rev. Lett.* **32** 1203 (1974),*Phys. Rev.* B13 544 (1976), *Solid St. Commun.* **19** 1193 (1976)

28. J B Pendry, *Surf. Sci.* **57** 679 (1976), *Photoemission and the Electronic Properties of Surfaces*, eds, B Feurbacher, Fitton and R F Willis (Wiley, NY, 1978)

29. J B Pendry & J F L Hopkinson, *J. Phys. F Met. Phys.* **8** 1009 (1978)

30. N Kar, *J. of Phys.* **C 14** 2185 (1981)

31. A Ishii & T Aisaka, *Surf. Sci.* **242** 250 (1991)

32. H J Levinson, F Greuter & E W Plummer, *Phys. Rev.* **B 27** 727 (1983)

33. A Bagchi & N.Kar, *Phys. Rev.* **B 18** 5248 (1978)

34. R K Thapa, P Das *et al*, Bull. Mat. Sci **16** 29 (1993)

35. J Weaver, *Hand Book of Chemistry and Physics of Solids* (CRC Press Boca Raton, Ohio, 1978)E-377

36. J B Pendry, *Low Energy Electron Diffraction* (Academic Press, 1974)

37. N W Ashcroft & N D Mermin, *Solid State Physics* (Holt, Reinhart and Winston, NY, 1976)p- 38

38. P Das, R K Thapa & N Kar, Mod. Phys. Lett. **B 5** 65 (1991)

39. R.K.Thapa & N.Kar; *Phys. Rev.* B 51 1995 (to be published)

40. R.K.Thapa, P.Das & N.Kar, *Mod. Phys. Lett.* **B 8** 361 (1994); R.K.Thapa; *Phys. Stat. Sol (b)* 179, 621 (1993)

41. P.Das and N.Kar, *Phys. Stat. Sol.* (b) **187**, 551 (1995)

42. I S Gradshteyn & I M Ryzhik, *Table of Integrals* (Academic Press, 1980)

43. F L Hopkinson, J B Pendry & D J Titterington, *Comput. Phys. Commun.* **19** 69 (1980)

44. L F Matheiss, *Phys. Rev.* **139** A 1893 (1965)

45. J Hermanson, *Solid St. Commun.* **22** 9 (1977)

46. M Born and E Wolf, *Principles of Optics*, section 2.3, Pergamon press, New York (1970)

47. B R A Nijboer & F W de Wette, *Physica* **24**, 422(1958)

48. N Kar and A Bagchi, *Solid St. Commun.* **33**,645(1980)

49. R Shuttleworth, *Proc. Phys. Soc.* (London) **A62**, 67 (1949)

50. G D Mahan, *J. Chem. Phys.* **43**, 1569 (1965)

51. F W De Wette, *Phys. Rev.* **123**, **103** (1961)

52. P Das & N Kar, *Mod. Phys. Lett.* **B 6** 1263 (1992)

53. P Das & N Kar, Mod. Phys. Lett. **B**, (accepted for publication)

APPENDICES

APPENDIX I

a) Eigenvalue equation to obtain u_g and v_g

$$\begin{pmatrix} I & -R \\ 0 & MT \end{pmatrix} \begin{pmatrix} u \\ v \end{pmatrix} = e^{-ik_z d_z} \begin{pmatrix} TP & 0 \\ -MRP & I \end{pmatrix} \begin{pmatrix} u \\ v \end{pmatrix}$$

where, $M_{g,g'} = e^{-i\vec{g}.\vec{d}_i} e^{i\vec{K}'_{gx} d_x} \delta_{g,g'}$ and $P_{g,g'} = e^{i\vec{g}.\vec{d}_i} e^{i\vec{K}'_{gx} d_x} \delta_{g,g'}$

d is a lattice translation vector, R and T are the reflection and transmission matrices between the layers and their expressions have been given by Pendry[36].

b) Expressions for $B_l(r)$ and $D_l(r)$, the radial part of the photon field for different values of l

$$B_0(r) = 2\int_0^{\pi} \frac{P_0(\cos\theta)}{\frac{r}{a}\cos\theta + \beta_1} \sin\theta d\theta$$

$$= \frac{2a}{r} \ln\left[\frac{\frac{r}{a} + \beta_1}{-\frac{r}{a} + \beta_1}\right]$$

$$B_1(r) = \frac{2}{3}\int_0^{\pi} \frac{P_1(\cos\theta)\sin\theta d\theta}{\frac{r}{a}\cos\theta + \beta_1}$$

$$= \frac{2}{3}\left[\frac{2a}{r} - \beta_1 \left(\frac{a}{r}\right)^2 \frac{\frac{r}{a} + \beta_1}{-\frac{r}{a} + \beta_1}\right]$$

$$B_2(r) = \frac{2}{5}\int_0^{\pi} \frac{P_2(\cos\theta)\sin\theta d\theta}{\frac{r}{a}\cos\theta + \beta_1}$$

$$= \frac{2}{5}\left[-3\beta_1 \left(\frac{a}{r}\right)^2 + \frac{3}{2}\beta_1^2 \left(\frac{a}{r}\right)^3 \ln\frac{\frac{r}{a} + \beta_1}{-\frac{r}{a} + \beta_1} - \frac{a}{2r} \ln\frac{\frac{r}{a} + \beta_1}{-\frac{r}{a} + \beta_1}\right]$$

$$B_3(r) = \frac{2}{7}\int_0^{\pi} \frac{P_3(\cos\theta)\sin\theta d\theta}{\frac{r}{a}\cos\theta+\beta_1}$$

$$=\frac{1}{7}\left[5\left\{\frac{2a}{3r}+2\left(\frac{a}{r}\right)^3\beta_1^2-\beta_1^3\left(\frac{a}{r}\right)^4\ln\frac{\frac{r}{a}+\beta_1}{-\frac{r}{a}+\beta_1}\right\}-\frac{15}{2}B_2(r)\right]$$

$$B_4(r) = \frac{2}{9}\int_0^{\pi} \frac{P_4(\cos\theta)\sin\theta d\theta}{\frac{r}{a}\cos\theta+\beta_1}$$

$$=\frac{1}{36}\left[35\left\{-\frac{2}{3}\beta_1\left(\frac{a}{r}\right)^2-2\beta_1^3\left(\frac{a}{r}\right)^4+\beta_1^4\left(\frac{a}{r}\right)^5\ln\frac{\frac{r}{a}+\beta_1}{-\frac{r}{a}+\beta_1}\right\}\right.$$

$$-30\left\{-2\beta_1^3\left(\frac{a}{r}\right)^2+\beta_1^2\left(\frac{a}{r}\right)^3\ln\frac{\frac{r}{a}+\beta_1}{-\frac{r}{a}+\beta_1}\right\}$$

$$\left.+3\frac{a}{r}\ln\frac{\frac{r}{a}+\beta_1}{-\frac{r}{a}+\beta_1}\right]$$

$$D_0(r) = 2\int_0^{\pi} \frac{P_0(\cos\theta)\sin\theta d\theta}{\left(\frac{r}{a}\cos\theta+\beta_1\right)^2}$$

$$=-\frac{2}{\beta_1^2-\frac{r^2}{a^2}}$$

$$D_1(r) = \frac{2}{3}\int_0^{\pi} \frac{P_1(\cos\theta)\sin\theta d\theta}{\left(\frac{r}{a}\cos\theta+\beta_1\right)^2}$$

$$=\frac{2a}{3r}\left[-\frac{2\beta_1}{\beta_1^2-\frac{r^2}{a^2}}+\frac{a}{r}\ln\frac{\frac{r}{a}+\beta_1}{-\frac{r}{a}+\beta_1}\right]$$

$$D_2(r) = \frac{2}{5}\int_0^{\pi} \frac{P_2(\cos\theta)\sin\theta\, d\theta}{(\frac{r}{a}+\beta_1)^2}$$

$$= \frac{2}{5}\Big[\frac{3}{2}\Big\{2(\frac{a}{r})^2+2\beta_1(\frac{a}{r})^2\frac{1}{\beta_1^2-\frac{r^2}{a^2}}$$

$$-2\beta_1(\frac{a}{r})^3\ln\frac{\frac{r}{a}+\beta_1}{-\frac{r}{a}+\beta_1}\Big\}-\frac{1}{\beta_1^2-\frac{r^2}{a^2}}\Big]$$

$$D_3(r) = \frac{2}{7}\int_0^{\pi} \frac{P_3(\cos\theta)\sin\theta\, d\theta}{(\frac{r}{a}+\beta_1)^2}$$

$$=\Big[-4\beta_1(\frac{a}{r})^3-2\beta_1^3(\frac{a}{r})^3\frac{1}{\beta_1^2-\frac{r^2}{a^2}}$$

$$+3\beta_1^2(\frac{a}{r})^4\ln\frac{\frac{r}{a}+\beta_1}{-\frac{r}{a}+\beta_1}\Big]$$

$$D_4(r) = \frac{2}{9}\int_0^{\pi} \frac{P_4(\cos\theta)\sin\theta\, d\theta}{(\frac{r}{a}\cos\theta+\beta_1)^2}$$

$$=\frac{1}{36}\Big[35\Big\{\frac{2}{3}(\frac{a}{3})^2+6\beta_1^2(\frac{a}{r})^4+2\beta_1^4(\frac{a}{r})^4\frac{1}{\beta_1^2-\frac{r^2}{a^2}}-4\beta_1^3(\frac{a}{r})^5\ln\frac{\frac{r}{a}+\beta_1}{-\frac{r}{a}+\beta_1}\Big\}$$

$$-30\Big\{2(\frac{a}{r})^2+2\beta_1^2(\frac{a}{r})^2\frac{1}{\beta_1^2-\frac{r^2}{a^2}}-2\beta_1(\frac{a}{r})^3\ln\frac{\frac{r}{a}+\beta_1}{-\frac{r}{+}\beta_1}\Big\}+\frac{6}{\beta_1^2-\frac{r^2}{a^2}}\Big]$$

APPENDIX II

```
C       PHOTOEMISSION PROGRAM WITH FREE ELECTRON WAVEFUNCTION
        COMPLEX A1,B1,CI,T1,T2,T3,T4,EPS,CMPLX
        COMMON AKI,AKP,AKF,AQ,A,ALPHA,CI
        CI=(0.,1.)
        READ (1,*) NP,NINT
        READ(1,*)WP,EI,THETA,A,ALPHA,VZ,NE
        WRITE(NP,4) WP,EI,THETA,A,ALPHA,VZ
        AKI=SQRT(2.*EI)
        AKP=SQRT(2.*(VZ-EI))
        DO 99 IE=1,NE
        READ(1,*) W,EPS1,EPS2
        AKF=SQRT(2.*(EI+W))
        AQ=SQRT(2.*(EI+W-VZ))
        WRITE(NP,2) W,AKI,AKP,AKF,AQ
        EPS=CMPLX(EPS1,EPS2)
        CALL REFRAC(W,WP,THETA,EPS,A1,B1)
        CALL TERM1 (A1,T1)
        CALL TERM2 (A1,B1,EPS,T2,NINT)
        CALL TERM3 (A1,EPS,T3)
        CALL TERM4 (A1,B1,EPS,T4,NINT)
        WRITE(NP,3) W,T1,T2,T3,T4
        CUR=CABS(T1+T2+T3+T4)
        CUR=CUR*CUR*AKF*AKF/W
 99     WRITE(NP,5)W,EPS,CUR
  2     FORMAT(3X,5(E12.4,3X))
  3     FORMAT(1X,F7.3,8(2X,E10.3))
  4     FORMAT(15X,6F12.4)
  5     FORMAT(2X,'W=',F7.4,'EPS=',2F10.4,'CURRENT=',E12.4)
        STOP
        END
C
         SUBROUTINE TERM3(A1,EPS,T3)
         COMPLEX A1,R1,CI,T3,EPS,Q,R2
         COMMON AKI,AKP,AKF,AQ,A,ALPHA,CI
         Q=SQRT(AKI/AQ) *AKP*EPS
         R2=1./(AKP-CI*AQ)
         R1=1./(CI*AQ+AKP)
         T3=R1+R2*(AQ-AKF)/(AQ+AKF)
         T3=-Q*T3*CI
         T3=T3*A1/(-AKP+CI*AKI)
         RETURN
         END
C
        SUBROUTINE TERM1(A1,T1)
         COMPLEX A1,T1,C1,C2,CI
         COMMON AKI,AKP,AKF,AQ,A,ALPHA,CI
         Q=SQRT(AKI*AQ)
         Q=0.5*Q/(AQ+AKF)
         AH=A*(AKI-AKF)
         C1=COS(AH)-CI*SIN(AH)
         C1=C1*EXP(-ALPHA*A)/(ALPHA+CI*(AKI-AKF))
         AG=A*(AKI+AKF)
         C2=COS(AG)+CI*SIN(AG)
```

```
      C2=C2*(CI*AKI+AKP)/(CI*AKI-AKP)
      C2=C2*EXP(-ALPHA*A)/(ALPHA-CI*(AKI+AKF))
      T1=2.*CI*A1*Q*(C1-C2)
      RETURN
      END
C
      SUBROUTINE TERM2 (A1,B1,EPS,T2,NINT)
      COMPLEX A1,B1,EPS,T2,CI,F1,F2,R1,R2,Q
      DIMENSION F1(1001),F2(1001)
      COMMON AKI,AKP,AKF,AQ,A,ALPHA,CI
      Q=CI*A*A1*EPS*SQRT(AQ*AKI)/(AQ+AKF)
      AL=-A
      AH=0.
      D=(AH-AL)/(NINT-1)
      DO 10 I=1,NINT
      X=AL+(I-1)*D
      F1(I)=COS((AKI-AKF)*X)+CI*SIN((AKI-AKF)*X)
      F1(I)=F1(I)*EXP(ALPHA*X)/(B1*X+A)
      F2(I)=COS((AKI+AKF)*X)-CI*SIN((AKI-AKF)*X)
10    F2(I)=F2(I)*EXP(ALPHA*X)/(B1*X+A)
      CALL SINT (AL,AH,F1,NINT,R1)
      CALL SINT (AL,AH,F2,NINT,R2)
      T2=R1-R2*(AKP+CI*AKI)/(CI*AKI-AKP)
      T2=Q*T2
      RETURN
      END
C
      SUBROUTINE TERM4 (A1,B1,EPS,T4,NINT)
      COMPLEX A1,B1,EPS,T4,F1,F2,R1,R2,Q
      DIMENSION F1(1001),F2(1001)
      COMMON AKI,AKP,AKF,AQ,A,ALPHA,CI
      Q=-0.5*B1*A1*A*EPS*SQRT(AQ/AKI)/(AQ+AKF)
      AL=-A
      AH=0.
      D=(AH-AL)/(NINT-1)
      DO 10 I=1,NINT
      X=AL+(I-1)*D
      F1(I)=COS((AKI-AKF)*X)+CI*SIN((AKI-AKF)*X)
      F2(I)=COS((AKI+AKF)*X)-CI*SIN((AKI+AKF)*X)
      F1(I)=F1(I)*EXP(ALPHA*X)/((B1*X+A)**2)
10    F2(I)=F2(I)*EXP(ALPHA*X)/((B1*X+A)**2)
      CALL SINT (AL,AH,F1,NINT,R1)
      CALL SINT (AL,AH,F2,NINT,R2)
      T4=R1+R2*(CI*AKI+AKP)/(CI*AKI-AKP)
      T4=Q*T4
      RETURN
      END
```

APPENDIX III

```
$DEBUG
CPHOTOEMISSION program with band wavefunction
      DIMENSION U(9),V(9),X(200),ATP(200),YGP(25),YGM(25),F2(200)
      DIMENSION YGFP(25),YGFM(25),YK(25),YH1(9,25),YH2(9,25)
      DIMENSION YH3(9,25),YH4(9,25),FR0(5),D4(5,200),D5(5,200)
      DIMENSION ZP(4,4,4,4),WP(4,4,4),VP(4,4,4),EPKF1(9),EMKF1(9)
      DIMENSION  PQ(2,9),PQF(2,9),IPQF(2,9),PKZ(9),XP(4,4,4,4)
      DIMENSION AR1(2),AR2(2),B1(2),B2(2),YP(4,4,4,4),F(200)
      DIMENSION A2(5,200),A3(5,200),E1(5,200),F1(200),F3(200)
      COMPLEX A2,A3,E1,FR0,CT1,CTM,ST1,STM,CF1,UX,UY,ZP,WP,VP
      COMPLEX EPS,EMKF1,U,V,CMPLX,CEXP,YK,YGP,YGM,YGFP,YGFM,EPKF1
      COMPLEX XA,YA,CT,ST,CF,A1,AB1,F1,F2,F3,F,XP,YP,PKZ
      COMPLEX EXKF,CSQRT,CI,YH1,YH2,YH3,YH4,CTP,STP,EPKF
      COMPLEX T1,T3,T4,T6,T8,T9,T10,CUR1,CUR2,EP2,D4,D5,EMKF
      COMMON/X1/R0,DD,TV
      COMMON/X2/AKF,AKP,AQ,ALPHA,PKZ,EXKF,AQKF
      COMMON/X3/U,V,E,EMKF1,YH1,YH2,YH3,YH4,YK,SQE,A1,AB1,FR0,
     &EPKF1,AD
      COMMON/X4/D4,D5,A2,A3,E1
      COMMON/X5/X,ATP,Z,CL,EE,NMESH,KRMT,JRKI,NF,INDP,IP
      COMMON/X6/F1,F2,F3,F,XP,YP,ZP,WP,VP
      DATA CZ,CI,PI/(0.0,0.0),(0.0,1.0),3.14159265/
      READ(1,*)Z,LMAX,R0
      READ(1,*)N,NINT,NMESH,NF,KRMT,INDP,IP
      READ(1,*)E,THETA,ALPHA,VZ,NW
      AKP=SQRT(2.*(VZ-E))
      SQE=SQRT(2.*E)
      READ(2,73)(X(J),ATP(J),J=1,NMESH)
 73   FORMAT(2E14.6)
      VPI=0.0
      DD=7.65306
      AD=R0+DD/4.
      AR1(1)=DD/2
      AR1(2)=DD/2
      AR2(1)=-DD/2
      AR2(2)=DD/2
      TV=ABS(AR1(1)*AR2(2)-AR1(2)*AR2(1))
      RTV=2.0*PI/TV
      B1(1)=AR2(2)*RTV
      B1(2)=-AR2(1)*RTV
      B2(1)=-AR1(2)*RTV
      B2(2)=AR1(1)*RTV
      IPQF(1,1)=0
      IPQF(2,1)=0
      IPQF(1,2)=1
      IPQF(2,2)=0
      IPQF(1,3)=-1
      IPQF(2,3)=0
      IPQF(1,4)=0
      IPQF(2,4)=1
      IPQF(1,5)=0
      IPQF(2,5)=-1
      IPQF(1,6)=1
```

```
      IPQF(2,6)=1
      IPQF(1,7)=1
      IPQF(2,7)=-1
      IPQF(1,8)=-1
      IPQF(2,8)=1
      IPQF(1,9)=-1
      IPQF(2,9)=-1
      WRITE(*,101) N
      DO 1 J=1,N
      WRITE (*,101) IPQF(1,J),IPQF(2,J)
      PQF(1,J)=FLOAT(IPQF(1,J))
      PQF(2,J)=FLOAT(IPQF(2,J))
      PQ(1,J)=B1(1)*PQF(1,J)+B2(1)*PQF(2,J)
 1    PQ(2,J)=B1(2)*PQF(1,J)+B2(2)*PQF(2,J)
      I2=1
      I3=1
      AK2=FLOAT(I2-1)*DK
      AK3=FLOAT(I3-1)*DK
101   FORMAT(2I3)
      READ(3,33)(U(IG),IG=1,9)
      READ(3,33)(V(IG),IG=1,9)
33    FORMAT(2E12.4)
      LMX=LMAX+2
      LMMAX=(LMAX+3)**2
      CT=CMPLX(1.0,0.0)
      ST=CZ
      CF=CMPLX(1.0,0.0)
      CALL SPHRM4(YK,CT,ST,CF,3)
      CALL SPLM(LMAX,NINT)
      DO 99 IW=1,NW
      READ(1,*)W,EPS1,EPS2
      EPS=CMPLX(EPS1,EPS2)
      AKF=SQRT(2.*(E+W))
      AQ=SQRT(2.*(E+W-VZ))
      AQKF=AQ+AKF
      EXKF=CEXP(CI*AKF*R0)
      YA=CMPLX(2.*E,-2.0*VPI+0.0000001)
      YA=CSQRT(YA)
      DO 31 JG=1,N
      BK2=PQ(1,JG)+AK2
      BK3=PQ(2,JG)+AK3
      CA=BK2*BK2+BK3*BK3
      XA=CMPLX(2.0*E-CA,-2.0*VPI+0.0000001)
      XA=CSQRT(XA)
      PKZ(JG)=XA
      EP1=2.*E+AKF*AKF
      EP2=2.*AKF*XA
      EPKF=EP1-EP2
      EPKF=CSQRT(EPKF)
      EMKF=EP1+EP2
      EMKF=CSQRT(EMKF)
      EPKF1(JG)=EPKF
      EMKF1(JG)=EMKF
      BX1=0.0
      CF1=CMPLX(1.0,0.0)
```

```
      IF(CA-1.0E-7)3,3,2
 2    BX1=SQRT(CA)
      CF1=CMPLX(BK2/BX1,BK3/BX1)
 3    CT1=XA/YA
      UX=XA-AKF
      CTP=UX/EPKF
      ST1=BX1/YA
      STP=BX1/EPKF
      UY=-XA-AKF
      CTM=UY/EMKF
      STM=BX1/EMKF
      CALL SPHRM4(YGP,CT1,ST1,CF1,LMX)
      CALL SPHRM4(YGM,-CT1,ST1,CF1,LMX)
      CALL SPHRM4(YGFP,CTP,STP,CF1,LMX)
      CALL SPHRM4(YGFM,CTM,STM,CF1,LMX)
      DO 31 K=1,LMMAX
      YH1(JG,K)=YGP(K)
      YH2(JG,K)=YGM(K)
      YH3(JG,K)=YGFP(K)
 31   YH4(JG,K)=YGFM(K)
      CALL REFRAC(THETA,A1,AB1,EPS,AD,R0)
      CALL TERM1(T1,NINT,EPS)
      CALL TERM3(T3,N,EPS)
      CALL TERM9(T9)
      CALL TERM6(T6,NINT,LMAX,EPS,N)
      CALL TERM4(T4,LMAX,NINT,N,EPS)
      CALL TERM8(T8,N)
      CALL TERM10(T10,NINT,LMAX,N)
      ALP1=ALPHA*R0
      ALP2=ALPHA*(R0+DD/2)*2.
      ALP3=ALPHA*(R0+DD)*2.
      CUR1=T9-T8+T10
      CUR2=(EXP(-ALP1)*(T1-T4+T6))+T3
      C1=CABS(CUR1)
      C1=C1*C1
      C2=CABS(CUR2)
      C2=C2*C2
      C1=(EXP(-ALP2)+EXP(-ALP3))*C1
      CUR=C1+C2
      CUR=CUR*AKF*AKF/W
 91   FORMAT(1X,'CUR',E12.4,1X,'W=',F7.4)
      WRITE(4,91)CUR,W
      WRITE(4,129)
 129  FORMAT(/)
 99   CONTINUE
      STOP
      END
C
     SUBROUTINE SPLM(LMAX,NINT)
      DIMENSION XP(4,4,4,4),YP(4,4,4,4),ZP(4,4,4,4),VP(4,4,4)
      DIMENSION F1(200),F2(200),F3(200),F(200),WP(4,4,4)
      COMPLEX F1,F2,F3,F,XP,YP,S2,S3,S4,ZP,S5,S6,WP,VP
      COMMON/X6/F1,F2,F3,F,XP,YP,ZP,WP,VP
      LM=LMAX+1
      DO 10 IL3=1,LM
```

```
      L3=IL3-1
      DO 10 IL2=1,LM+1
      L2=IL2-1
      DO 10 IL1=1,LM+1
      L1=IL1-1
      DO 10 M1=0,L1
      IM1=M1+1
      CALL PLM1(L1,M1,L2,L3,NINT,S2,S3,S4,S5,S6)
      YP(IL3,IL2,IL1,IM1)=S2
      XP(IL3,IL2,IL1,IM1)=S3
      ZP(IL3,IL2,IL1,IM1)=S4
      WP(IL3,IL1,IM1)=S5
      VP(IL3,IL1,IM1)=S6
10    CONTINUE
      RETURN
      END
C
      SUBROUTINE PLM1(L1,M1,L2,L3,NINT,S2,S3,S4,S5,S6)
      DIMENSION F2(200),F3(200),F1(200),F(200),F31(200),F21(200)
      DIMENSION XP(4,4,4,4),YP(4,4,4,4),ZP(4,4,4,4),WP(4,4,4)
      DIMENSION VP(4,4,4)
      COMPLEX F1,F2,F3,F,S2,S3,XP,YP,S4,ZP,F31,F21,S5,S6,WP,VP
      COMMON/X6/F1,F2,F3,F,XP,YP,ZP,WP,VP
      AL=0.
      AH=3.14159265
      C=(AH-AL)/(NINT-1)
      U=FLOAT((L3+M1)*(L3-M1+1))
      DO 1 K=1,NINT
      XN=AL+(K-1)*C
      X1=PLM(XN,L1,M1)
      IF(M1.GT.L3) THEN
      X2=0.
      ELSE
      X2=PLM(XN,L3,M1)
      ENDIF
      IF(M1+1.GT.L3) THEN
      X3=0.
      ELSE
      X3=PLM(XN,L3,M1+1)
      ENDIF
      X5=PLM(XN,L2,0)
      IF(M1-1.LT.0) THEN
      X4=0.
      ELSE
      X4=PLM(XN,L3,M1-1)
      ENDIF
      PX1=X1*X2
      PX2=X1*X3
      PX3=X1*X4*U
      S=SIN(XN)
      F3(K)=PX1*S*COS(XN)
      F31(K)=F3(K)*X5
      F2(K)=(PX2-PX3)*S*S
      F21(k)=F2(K)*X5
      F(K)=PX1*S*X5
```

```
 1    CONTINUE
      CALL SINT(AL,AH,F31,NINT,S3)
      CALL SINT(AL,AH,F21,NINT,S2)
      CALL SINT(AL,AH,F,NINT,S4)
      CALL SINT(AL,AH,F3,NINT,S5)
      CALL SINT(AL,AH,F2,NINT,S6)
      IF(CABS(S5).LE.1.0E-6) S5=0.
      IF(CABS(S6).LE.1.0E-6) S6=0.
      IF(CABS(S4).LE.1.0E-6) S4=0.
      IF(CABS(S3).LE.1.0E-6) S3=0.
      IF(CABS(S2).LE.1.0E-6) S2=0.
      RETURN
      END
C
      SUBROUTINE REFRAC(THETA,A1,B1,EPS,AD,R0)
      COMPLEX A1,CX,CSQRT,EPS,B1
      S2=SIN(2.*THETA)
      S1=SIN(THETA)
      C1=COS(THETA)
      B1=1./(1.-EPS)-R0/AD
      CX=EPS-S1*S1
      CX=CSQRT(CX)
      A1=-S2/(CX+EPS*C1)
      RETURN
      END
C
      SUBROUTINE TERM1(T1,NINT,EPS)
      DIMENSION F1(200),F2(200),U(9),V(9),F3(200),F(200),WP(4,4,4)
      DIMENSION PKZ(9),XP(4,4,4,4),YP(4,4,4,4),ZP(4,4,4,4),F4(200)
      DIMENSION YH1(9,25),YH2(9,25),YH3(9,25),YH4(9,25),YK(25)
      DIMENSION VP(4,4,4),EPKF1(9),EMKF1(9),FR0(5)
      COMPLEX F1,F2,EPS,R1,T1,U,V,CI,Q,EXKF,EMKF1,EPKF1,XP,YP,ZP
      COMPLEX YK,F3,CEXP,YH1,YH2,YH3,YH4,A1,AB1,Y,F,FR0,WP
      COMPLEX PKZ,F4,VP
      COMMON/X1/R0,DD,TV
      COMMON/X2/AKF,AKP,AQ,ALPHA,PKZ,EXKF,AQKF
      COMMON/X3/U,V,E,EMKF1,YH1,YH2,YH3,YH4,YK,SQE,A1,AB1,FR0,
     &EPKF1,AD
      COMMON/X6/F1,F2,F3,F,XP,YP,ZP,WP,VP
      CI=CMPLX(0.0,1.0)
      Q=(2.*AQ*A1*EPS)/(AQKF*(1.-EPS))
      Q=Q*TV*EXKF
      AL=-DD/4
      AH=R0
      C=(AH-AL)/(NINT-1)
      P1=SQE-AKF
      P2=-SQE-AKF
      DO 10 I=1,NINT
      X=AL+(I-1)*C
      Y=1./(X/AD+AB1)
      F1(I)=U(1)*CEXP(CI*P1*X)
      F2(I)=V(1)*CEXP(CI*P2*X)
      F3(I)=F1(I)-F2(i)
      F4(I)=F1(I)+F2(i)
 10   F(I)=F3(I)*(CI*SQE*Y)-0.5*Y*Y*F4(i)/AD
```

```
      CALL SINT(AL,AH,F,NINT,R1)
      T1=R1*Q
      RETURN
      END
C
      SUBROUTINE TERM3(T3,N,EPS)
      DIMENSION T(9),YH1(9,25),YH2(9,25),YH3(9,25),YH4(9,25),YK(25)
      DIMENSION U(9),V(9),FR0(5),PKZ(9),EPKF1(9),EMKF1(9)
      COMPLEX EPS,CI,T3,R1,R2,R,T,Q,EXKF,EMKF1,A1,AB1
      COMPLEX YH1,YH2,YH3,YH4,YK,U,V,FR0,EPKF1,PKZ
      COMMON/X1/R0,DD,TV
      COMMON/X2/AKF,AKP,AQ,ALPHA,PKZ,EXKF,AQKF
      COMMON/X3/U,V,E,EMKF1,YH1,YH2,YH3,YH4,YK,SQE,A1,AB1,FR0,
     &EPKF1,AD
      CI=CMPLX(0.0,1.0)
      Q=A1*EPS*AKP
      R1=1./(AKP+CI*AQ)
      R2=(AQ-AKF)/(AQKF)
      R2=R2/(AKP-CI*AQ)
      R=R1+R2
      CALL TG(T,N)
      T3=Q*T(1)*R*TV
      T3=-T3
      RETURN
      END
C
      SUBROUTINE TG(T,N)
      DIMENSION U(9),V(9),T(9),YK(25),FR0(5),PKZ(9),EPKF1(9)
      DIMENSION YH1(9,25),YH2(9,25),YH3(9,25),YH4(9,25)
      DIMENSION ZK(9),ENKF1(9)
      COMPLEX T,CI,U,V,EXKF,EMKF1
      COMPLEX YK,YH1,YH2,YH3,YH4,A1,AB1,FR0,EPKF1,PKZ,ZK
      COMMON/X1/R0,DD,TV
      COMMON/X2/AKF,AKP,AQ,ALPHA,PKZ,EXKF,AQKF
      COMMON/X3/U,V,E,EMKF1,YH1,YH2,YH3,YH4,YK,SQE,A1,AB1,FR0,
     &EPKF1,AD
      CI=CMPLX(0.0,1.0)
      DO 10 I=1,N
      ZK(I)=PKZ(I)*R0*CI
10    T(I)=U(I)*CEXP(ZK(I))+V(I)*CEXP(-ZK(I))
      RETURN
      END
C
      SUBROUTINE RADIAL(C4,C5,R)
      COMPLEX A1,AB1,Q3,Q4,Q5,C4,C5,CLOG,Q6,EPKF1,Q10,Q12
      DIMENSION C4(5),C5(5),YK(25),FR0(5),EPKF1(9),EMKF1(9)
      DIMENSION YH1(9,25),YH2(9,25),YH3(9,25),YH4(9,25),U(9),V(9)
      COMPLEX YH1,YH2,YH3,YH4,YK,U,V,EMKF1,FR0,Q41,Q42,Q7,Q8,Q9
      COMMON/X1/R0,DD,TV
      COMMON/X3/U,V,E,EMKF1,YH1,YH2,YH3,YH4,YK,SQE,A1,AB1,FR0,
     &EPKF1,AD
      PI=3.14159265
      SQP=SQRT(PI)
      Q1=AD/R
      Q2=Q1*Q1
```

```
      Q3=AB1*AB1
      Q11=1./Q1
      Q41=(AB1+Q11)/(AB1-Q11)
      Q42=CLOG(Q41)
      Q4=Q1*Q42
      Q6=-2.*AB1*Q2+Q3*Q2*Q4
      Q5=1./(Q3-Q11*Q11)
      Q7=2.*Q1-AB1*Q1*Q4
      Q8=(Q1*Q2*Q3*Q4*AB1)
      Q9=Q2*Q1*Q3
      Q10=2.*Q3*Q3*Q2*Q2*Q5
      Q12=4.*Q3*AB1*Q2*Q2*Q4
      SQ3=SQRT(3.*PI)
      SQ5=SQRT(5.*PI)
      I=1
      C4(I)=SQP*Q4
      C4(I+1)=SQ3*Q7
      C4(I+2)=SQ5*((3./2.)*Q6-0.5*Q4)
      C4(I+3)=SQRT(7.*PI/4.)*(5.*((2./3.)*Q1+2.*Q9-Q8)-3.*Q7)
      C4(I+4)=35.*((-2./3.)*AB1*Q2-2.*Q3*AB1*Q2*Q2+Q3*Q3*Q2*Q2*Q4
     &)-30.*(-2.*AB1*Q2+Q3*Q4*Q2)+3.*Q4
      C4(I+4)=C4(I+4)*(3./8.)*SQP
      C5(I)=2.*SQP*Q5
      C5(I+1)=SQ3*Q1*(-2.*AB1*Q5+Q4)
      C5(I+2)=SQ5*(3.*Q2-3.*AB1*Q2*Q4+Q5*(3.*Q3*Q2-1))
      C5(I+3)=SQRT(7.*PI/4.)*(5.*(-4.*AB1*Q1*Q2-2.*Q3*AB1*Q2*Q1*Q5+
     &3.*Q3*Q4*Q2*Q1)-3.*C5(I+1)/SQ3)
      C5(I+4)=35.*((2./3)*Q2+6.*Q3*Q2*Q2+Q10-Q12)-
     &30.*(2.*Q2+2.*Q3*Q2*Q5-2.*AB1*Q2*Q4)+6.*Q5
      C5(I+4)=C5(I+4)*(3./8.)*SQP
      RETURN
      END
C
      SUBROUTINE TERM4(T4,LMAX,NINT,N,EPS)
      DIMENSION F1(200),F2(200),F3(200),WP(4,4,4),VP(4,4,4)
      DIMENSION YK(25),U(9),V(9),F(200),FR0(5),PKZ(9),EPKF1(9)
      DIMENSION YH1(9,25),YH2(9,25),YH3(9,25),YH4(9,25)
      DIMENSION D4(5,200),D5(5,200),XP(4,4,4,4),YP(4,4,4,4),F4(200)
      DIMENSION A2(5,200),A3(5,200),E1(5,200),ZP(4,4,4,4),EMKF1(9)
      COMPLEX D4,D5,A2,A3,E1,E2M,EPKF1,E2P,F4
      COMPLEX CI,YK,U,V,Q,P2,F,T4,EXKF,EMKF1,A1,AB1
      COMPLEX EPS,YH1,YH2,YH3,YH4,Y1,Y2,P1,XP,YP,ZP
      COMPLEX F1,F2,F3,R1,FR0,WP,VP,PKZ,BJ1,BJ2,BN1,BN2
      COMMON/X1/R0,DD,TV
      COMMON/X2/AKF,AKP,AQ,ALPHA,PKZ,EXKF,AQKF
      COMMON/X3/U,V,E,EMKF1,YH1,YH2,YH3,YH4,YK,SQE,A1,AB1,FR0,
     &EPKF1,AD
      COMMON/X4/D4,D5,A2,A3,E1
      COMMON/X6/F1,F2,F3,F,XP,YP,ZP,WP,VP
      DATA CI,PI/(0.0,1.0),3.14159265/
      Q=8.*PI*A1*EPS*AQ*EXKF
      Q=Q/(AQKF*(1.-EPS))
      T4=0.0
      AL=0.
      AH=R0
```

```
      M=0
      C=(AH-AL)/(NINT-1)
      DO 20 IG=1,N
      DO 10 IL=1,LMAX+3
      L=IL-1
      CL=FLOAT(L)
      LC=L*(L+1)+M+1
      Y1=YH3(IG,LC)
      Y2=YH4(IG,LC)
      IF((CABS(Y1).EQ.0.).AND.(CABS(Y2).EQ.0.))GOTO 10
      P1=CI**L
      DO 40 K=1,NINT
      IF(K.EQ.1)GOTO 31
      X=AL+(K-1)*C
      E2P=EPKF1(IG)*X
      E2M=EMKF1(IG)*X
      CALL CALXBF(E2P,CL,BJ1,BN1)
      CALL CALXBF(E2M,CL,BJ2,BN2)
      F1(K)=U(iG)*Y1*BJ1
      F2(K)=V(iG)*Y2*BJ2
      F(K)=F1(K)-F2(K)
      F4(K)=F1(k)+F2(K)
      F3(K)=(F(K)*CI*PKZ(IG)*D4(IL,K)-0.5*D5(IL,K)*F4(K)/AD)*X*X
      GO TO 40
 31   F3(K)=0.
 40   CONTINUE
      CALL SINT(AL,AH,F3,NINT,R1)
      P2=R1*P1
      T4=T4+P2
 10   CONTINUE
 20   CONTINUE
      T4=T4*Q
      RETURN
      END
C
      SUBROUTINE ALM(AL1,N,L,M)
      DIMENSION U(9),V(9),YK(25),YH1(9,25),YH2(9,25)
      DIMENSION YH3(9,25),YH4(9,25),FR0(5),EPKF1(9),EMKF1(9)
      COMPLEX A1,AB1,AL1,R,S1,BJ,BN,S,CONJG,FR0,CI,EPKF1
      COMPLEX YK,U,V,EMKF1,YH1,YH2,YH3,YH4,Y1,Y2,Y3,Q
      COMMON/X1/R0,DD,TV
      COMMON/X3/U,V,E,EMKF1,YH1,YH2,YH3,YH4,YK,SQE,A1,AB1,FR0,
     &EPKF1,AD
      DATA CI,PI/(0.0,1.0),3.14159265/
      Q=4.*PI
      S=0.0
      LC=L*(L+1)+M+1
      CL=FLOAT(L)
      S1=SQE*R0
      CALL CALXBF(S1,CL,BJ,BN)
      DO 20 IG=1,N
      Y1=CONJG(YH1(IG,LC))
      Y2=CONJG(YH2(IG,LC))
      IF((CABS(Y1).EQ.0.).AND.(CABS(Y2).EQ.0.))GOTO 20
      Y3=Y1*U(IG)+Y2*V(IG)
```

```
      S=S+Y3*BJ
 20   CONTINUE
      R=(CI**L)*S*Q
      AL1=R/FR0(L+1)
      RETURN
      END
C
      SUBROUTINE TERM6(T6,NINT,LMAX,EPS,N)
      DIMENSION F1(200),F2(200),F3(200),YK(25),F(200)
      DIMENSION FI(200),DFI(200),ATP(200),X(200),PKZ(9)
      DIMENSION U(9),V(9),C4(5),C5(5),XP(4,4,4,4),YP(4,4,4,4)
      DIMENSION YH1(9,25),YH2(9,25),YH3(9,25),YH4(9,25)
      DIMENSION A3(5,200),A2(5,200),E1(5,200),D4(5,200),FR0(5)
      DIMENSION D5(5,200),ZP(4,4,4,4),WP(4,4,4),EPKF1(9)
      DIMENSION XL(4),FJ(4),DFJ(4),VP(4,4,4),EMKF1(9)
      COMPLEX FJ,DFJ,EPKF1,XP,YP,ZP,WP,VP
      COMPLEX A2,A3,E1,D4,D5,R1,C2,Y2,Y1
      COMPLEX YH1,YH2,YH3,YH4,A1,AB1,C4,C5
      COMPLEX FL,DFL1,DFL,DFL3,X1,X2,X3,FIR0,FR0
      COMPLEX YK,FI,DFI,U,V,EPS,EXKF,EMKF1,T6,Q1
      COMPLEX DEL,BJ1,BN1,S1,F,F1,F2,F3,CI,AL1,PKZ
      COMMON/X1/R0,DD,TV
      COMMON/X2/AKF,AKP,AQ,ALPHA,PKZ,EXKF,AQKF
      COMMON/X3/U,V,E,EMKF1,YH1,YH2,YH3,YH4,YK,SQE,A1,AB1,FR0,
     &  EPKF1,AD
      COMMON/X4/D4,D5,A2,A3,E1
      COMMON/X5/X,ATP,Z,CL,EE,NMESH,KRMT,JRKI,NF,INDP,IP
      COMMON/X6/F1,F2,F3,F,XP,YP,ZP,WP,VP
      DATA CI,PI/(0.0,1.0),3.14159265/
      Q1=16.*PI*AQ*A1*EPS*EXKF*PI
      Q1=Q1/((1.-EPS)*AQKF)
      T6=0.0
      JRKI=NF
      EE=E
      AL=0.
      AH=R0
      C=(AH-AL)/(NINT-1)
      LX=LMAX+3
      DO 10 IL=1,LX
      L=IL-1
      CL=FLOAT(L)
      CALL CALXFI(FI,DFI,DEL,E,L,FIR0)
      FR0(IL)=FIR0/R0
      DO 10 K=2,NINT
      XN=AL+(K-1)*C
      IF(L.GT.0)GO TO 25
      CALL RADIAL(C4,C5,XN)
      DO 28 LL=1,5
      D4(LL,K)=C4(LL)
 28   D5(LL,K)=C5(LL)
 25   S1=AKF*XN
      CALL CALXBF(S1,CL,BJ1,BN1)
      E1(IL,K)=BJ1
      FI(K)=FI(K)/XN
      DFI(K)=(DFI(K)-FI(K))/XN
```

```
      DO 60 ITEST=1,200
      IF(X(ITEST).GT.XN)GOTO 61
60    CONTINUE
61    JL=ITEST
      IF(ITEST.LE.2)JL=3
      XL(1)=X(JL-2)
      XL(2)=X(JL-1)
      XL(3)=X(JL)
      XL(4)=X(JL+1)
      FJ(1)=FI(JL-2)
      FJ(2)=FI(JL-1)
      FJ(3)=FI(JL)
      FJ(4)=FI(JL+1)
      DFJ(1)=DFI(JL-2)
      DFJ(2)=DFI(JL-1)
      DFJ(3)=DFI(JL)
      DFJ(4)=DFI(JL+1)
      CALL INTERP(XL,FJ,XN,FL,DFL1)
      CALL INTERP(XL,DFJ,XN,DFL,DFL3)
      A2(IL,K)=FL
      A3(IL,K)=DFL
10    CONTINUE
      LM=LMAX+1
      LM1=LM+1
      DO 12 IL3=1,LM
      L3=IL3-1
      DO 12 IL2=1,LM1
      L2=IL2-1
      DO 14 IL1=1,LM1
      L1=IL1-1
      DO 14 M1=-L1,L1
      IM1=IABS(M1)
      IF(IM1.GT.L3)GOTO 14
      CALL ALM(AL1,N,L3,M1)
      LC=L1*(L1+1)+M1+1
      Y1=YK(LC)
      IF(CABS(Y1).EQ.0.)GOTO 14
      Y2=AL1
      Y2=Y2*Y1
      Y2=Y2*(-CI**L1)
      C1=FLOAT(((2*L1+1)*(2*L2+1)*(2*L3+1)*FAK(L1-IM1)*FAK(L3-IM1))
     &/(FAK(L1+IM1)*FAK(L3+IM1)*4.*PI))
      C1=SQRT(C1)/(4.*PI)
      C2=C1*Y2
      X1=XP(IL3,IL2,IL1,IM1+1)
      X2=YP(IL3,IL2,IL1,IM1+1)
      X3=ZP(IL3,IL2,IL1,IM1+1)
      IF((CABS(X1).EQ.0.).AND.(CABS(X2).EQ.0.).AND.(CABS(X3).EQ.
     &0.))GOTO 14
      DO 15 K=2,NINT
      XN=AL+(K-1)*C
      F1(K)=X1*XN*XN*A3(IL3,K)
      F2(K)=(F1(K)+0.5*X2*A2(IL3,K)*XN)*D4(IL2,K)
      F3(K)=F2(K)-0.5*X3*A2(IL3,K)*D5(IL2,K)*XN*XN/AD
      F(K)=F3(K)*E1(L1+1,K)
```

```
 15   CONTINUE
      CALL SINT(AL,AH,F,NINT,R1)
      T6=T6+R1*C2
 14   CONTINUE
 12   CONTINUE
      T6=T6*Q1
      WRITE(*,108)T6
 108  FORMAT(1X,'T6',2E12.4)
      RETURN
      END
C
      SUBROUTINE TERM9(T9)
      DIMENSION U(9),V(9),YK(25),YH1(9,25),YH2(9,25),YH3(9,25)
      DIMENSION YH4(9,25),FR0(5),PKZ(9),EPKF1(9),EMKF1(9)
      COMPLEX U,V,T9,Q1,EXKF,EMKF1,X1,X2,X3,CI,PKZ
      COMPLEX YK,YH1,YH2,YH3,YH4,A1,AB1,FR0,EPKF1
      COMMON/X1/R0,DD,TV
      COMMON/X2/AKF,AKP,AQ,ALPHA,PKZ,EXKF,AQKF
      COMMON/X3/U,V,E,EMKF1,YH1,YH2,YH3,YH4,YK,SQE,A1,AB1,FR0,
     &EPKF1,AD
      CI=CMPLX(0.0,1.0)
      Q1=4.*AQ*A1*CI*CEXP(CI*AKF*(R0+DD/2))
      Q1=Q1*TV*SQE
      Y1=(SQE-AKF)
      Y2=(SQE+AKF)
      X1=U(1)/Y1
      X1=X1*SIN(Y1*DD/4)
      X2=V(1)/Y2
      X2=X2*SIN(Y2*DD/4)
      X3=X1-X2
      T9=Q1*X3
      WRITE(*,11)T9
 11   FORMAT(1X,'T9',2E12.4)
      RETURN
      END
C
      SUBROUTINE TERM8(T8,N)
      DIMENSION YK(25),U(9),V(9),F(200),YH1(9,25),YH2(9,25),FR0(5)
      DIMENSION YH3(9,25),YH4(9,25),F1(200),F2(200),F3(200)
      DIMENSION A2(5,200),A3(5,200),E1(5,200)
      DIMENSION PKZ(9),D4(5,200),D5(5,200),XP(4,4,4,4),YP(4,4,4,4)
      DIMENSION ZP(4,4,4,4),WP(4,4,4),VP(4,4,4),EPKF1(9),EMKF1(9)
      COMPLEX XP,YP,ZP,WP,VP,PKZ
      COMPLEX A2,A3,E1,FR0,CONJG,EPKF1,D4,D5
      COMPLEX YH1,YH2,YH3,YH4,A1,AB1,F1,F2,F3,Y1,Y2
      COMPLEX CI,YK,U,V,F,Q,EXKF,EMKF1,T8,E2M,E2P
      COMMON/X1/R0,DD,TV
      COMMON/X2/AKF,AKP,AQ,ALPHA,PKZ,EXKF,AQKF
      COMMON/X3/U,V,E,EMKF1,YH1,YH2,YH3,YH4,YK,SQE,A1,AB1,FR0,
     &EPKF1,AD
      COMMON/X4/D4,D5,A2,A3,E1
      COMMON/X6/F1,F2,F3,F,XP,YP,ZP,WP,VP
      DATA CI,PI/(0.0,1.0),3.14159265/
      Q=8.*PI*CI*A1/AQKF
      Q=Q*AQ*2.*SQRT(PI)*CEXP(CI*AKF*(R0+DD/2))
```

```
      T8=0.
      LC=1
      DO 20 IG=1,N
      Y1=CONJG(YH3(IG,LC))
      Y2=CONJG(YH4(IG,LC))
      IF((CABS(Y1).EQ.0.).AND.(CABS(Y2).EQ.0.))GOTO 20
      F1(IG)=CSIN(EPKF1(IG)*R0)/(EPKF1(IG)**3)
      F2(IG)=R0*CCOS(EPKF1(IG)*R0)/(EPKF1(IG)*EPKF1(IG))
      F2(IG)=(F1(IG)-F2(iG))*Y1*U(IG)
      F3(IG)=CSIN(EMKF1(IG)*R0)/(EMKF1(IG)**3)
      F(IG)=R0*CCOS(EMKF1(IG)*R0)/(EMKF1(IG)*EMKF1(IG))
      F(IG)=(F3(IG)-F(IG))*Y2*V(IG)
      T8=T8+PKZ(IG)*(F2(IG)-F(IG))
 20   CONTINUE
      T8=Q*T8
      WRITE(*,22)T8
 22   FORMAT(1X,'T8',2E12.4)
      RETURN
      END
C
      SUBROUTINE TERM10(T10,NINT,LMAX,N)
      DIMENSION F1(200),F2(200),YK(25),F3(200),F(200),XP(4,4,4,4)
      DIMENSION FR0(5),PKZ(9),D4(5,200),YP(4,4,4,4)
      DIMENSION U(9),V(9),YH1(9,25),YH2(9,25),YH3(9,25),YH4(9,25)
      DIMENSION A2(5,200),A3(5,200),E1(5,200),D5(5,200)
      DIMENSION ZP(4,4,4,4),WP(4,4,4),VP(4,4,4),EPKF1(9),EMKF1(9)
      COMPLEX A2,A3,E1,EPKF1,XP,ZP,YP,WP,VP
      COMPLEX YK,EMKF1,U,V,CI,FR0,D4,D5
      COMPLEX EXKF,T10,Q1,R1,F3,Y1,Y2,C2,PKZ
      COMPLEX YH1,YH2,YH3,YH4,A1,AB1,F,F1,F2,AL1,X1,X2
      COMMON/X1/R0,DD,TV
      COMMON/X2/AKF,AKP,AQ,ALPHA,PKZ,EXKF,AQKF
      COMMON/X3/U,V,E,EMKF1,YH1,YH2,YH3,YH4,YK,SQE,A1,AB1,FR0,
     &EPKF1,AD
      COMMON/X4/D4,D5,A2,A3,E1
      COMMON/X6/F1,F2,F3,F,XP,YP,ZP,WP,VP
      DATA CI,PI/(0.0,1.0),3.14159265/
      Q1=16.*AQ*A1*PI
      Q1=Q1*PI*CEXP(CI*AKF*(R0+DD/2))/AQKF
       T10=0.0
       AL=0.
       AH=R0
       C=(AH-AL)/(NINT-1)
       LM=LMAX+1
       DO 10 IL3=1,LM
       L3=IL3-1
       DO 12 IL1=1,LMAX+2
       L1=IL1-1
       DO 12 M1=-L1,L1
       IM1=IABS(M1)
       IF(IM1.GT.L3)GOTO 12
       CALL ALM(AL1,N,L3,M1)
       Y1=AL1
       LC=L1*(L1+1)+M1+1
       Y2=YK(LC)
```

```
      IF(CABS(Y2).EQ.0.)GOTO 12
      Y2=Y1*Y2
      C1=FLOAT(((2*L1+1)*(2*L3+1)*FAK(L3-IM1)*FAK(L1-IM1))/
     &(FAK(L1+IM1)*FAK(L3+IM1)))
      C1=SQRT(C1)/(4.*PI)
      C2=C1*Y2*(-CI**L1)
      X1=WP(IL3,IL1,IM1+1)
      X2=VP(IL3,IL1,IM1+1)
      IF((CABS(X1).EQ.0.).AND.(CABS(X2).EQ.0.))GOTO 12
      DO 15 K=2,NINT
      XN=AL+(K-1)*C
      F1(K)=X1*A3(IL3,K)*XN*XN
      F2(K)=X2*A2(IL3,K)*XN*0.5
      F3(K)=(F1(K)+F2(K))*E1(IL1,K)
15    CONTINUE
      CALL SINT(AL,AH,F3,NINT,R1)
      T10=T10+R1*C2
12    CONTINUE
10    CONTINUE
      T10=T10*Q1
      RETURN
      END
```

APPENDIX IV

```
C       DIPOLE SUM FOR DIAMOND LATTICE-ZERO'TH PLANE
        DOUBLE PRECISION R1,R2,R3,R4,R5,R6,X3,X1,X2,S
        READ (1,*) M,N3
        X3=FLOAT(N3)
        S=0.0
        M1=(M+1)/2
        R3=X3*X3
        DO 10 I=1,M
        N1=I-M1
        X1=FLOAT(N1)
        DO 20 J=1,M
        N2=J-M1
        X2=FLOAT(N2)
        R1=(X1*X1+X2*X2)*0.5+R3
        R2=3.*R3-R1
        R4=DSQRT(R1)
        R5=R4*R4*R4*R4*R4
        R6=R2/R5
        S=(S+R6)
  20    CONTINUE
        WRITE (6,*) N1,S
  10    CONTINUE
        S1=S/8.
        WRITE(6,32) M,N3,S,S1
32      FORMAT(2X,'M',I5,2X,'N3',I1,5X,'S',E16.7,2X,'S1',E16.7)
        STOP
        END
C       DIPOLE SUM FOR THE 1ST PLANE
        DOUBLE PRECISION X,SUM,R1,R2,R3,R4
        REAL N1,N2
        READ (1,*) M,N3
        SUM=0.0
        DO 3 I=1,M
        N1=FLOAT(I-(M+1)/2)
        DO 2 J= 1,M
        N2= FLOAT(J-(M+1)/2)
        R1=N1**2+N2**2+N1*N2
        R2=(8/3)*N3**2
        R3=DSQRT(R1+R2)
        R4=R3*R3*R3*R3*R3
        X=(2*R2-R1)/R4
        SUM=SUM+X
  2     CONTINUE
        WRITE (1,*) SUM,X
  3     CONTINUE
        WRITE (1,10) M,SUM,N3
 10     FORMAT (2X,'M=',I4,10X,'SUM=',E14.5,8X,'N3=',I2)
        STOP
        END
C       DIPOLE SUM FOR DIAMOND LATTICE-2ND PLANE
        DOUBLE PRECISION R1,R2,R3,R4,R5,R6,R7,RO,X1,X2,X3
        READ(1,*)M,N3
        X3=FLOAT(N3)
```

```
      S=0.0
      M1=(M+1)/2
      RO=FLOAT(M1)
      R3=(X3+0.5)*(X3+0.5)
      DO 10 I=1,M
      N1=I-M1
      X1=FLOAT(N1)
      DO 20 J=1,M
      N2=J-M1
      X2=FLOAT(N2)
      R1=(X1+0.5)*(X1+0.5)*(0.5)
      R2=R1+(X2+0.5)*(X2+0.5)*(0.5)
      R4=R2+R3
      R5=DSQRT(R4)
      IF(R5.GT.RO) GO TO 20
      R6=R5*R5*R5*R5*R5
      R7=(3.*R3-R4)/R6
      S=S+R7
   20 CONTINUE
      IF(I/20.EQ.I/20) WRITE(6,31) N1,S
   10 CONTINUE
      S=S/8.
      WRITE(6,32) M,N3,S
   31 FORMAT(2X,'N1=',I5,2X,'S FOR N1=',E16.7)
   32 FORMAT(2X,'M=',I5,2X,'N3=',I1,5X,'SUM=',E16.7)
      STOP
      END

C     DIPOLE SUM FOR DIAMOND LATTICE-3RD PLANE
      DOUBLE PRECISION R1,R2,R3,R4,R5,R6,R7,RO,X1,X2,X3
      READ(1,*)M,N3
      X3=FLOAT(N3)
      S=0.0
      M1=(M+1)/2
      RO=FLOAT(M1)
      R3=(X3+0.75)*(X3+0.75)
      DO 10 I=1,M
      N1=I-M1
      X1=FLOAT(N1)
      DO 20 J=1,M
      N2=J-M1
      X2=FLOAT(N2)
      R1=(X1+0.5)*(X1+0.5)*(0.5)
      R2=R1+(X2+1)*(X2+1)*0.5
      R4=R2+R3
      R5=DSQRT(R4)
      IF(R5.GT.RO) GO TO 20
      R6=R5*R5*R5*R5*R5
      R7=(3.*R3-R4)/R6
      S=S+R7
   20 CONTINUE
      IF(I/20.EQ.I/20) WRITE(6,31) N1,S
   10 CONTINUE
      WRITE(6,32) M,N3,S
   31 FORMAT(2X,'N1=',I5,2X,'S FOR N1=',E16.7)
```

```
 32   FORMAT(2X,'M=',I5,2X,'N3=',I1,5X,'SUM=',E16.7)
      STOP
      END
C
C     MAIN PROGRAM TO CALCULATE  DIPOLE FIELD AND DIPOLE MOMENT
C     DENSITY
      DIMENSION A(33,33),P(33),X(33),E(33),INT(33)
      EMACH=1.0E-06
      PB=-3.14159*8./3.
      READ(1,*) NMAX,IT,GS,DG
      NR=NMAX
      NC=NMAX
      AZ=-3.193856
      A1=-2.086166
      A2=-0.505366
      A3=-0.00618
      A4=0.0080
      WRITE(6,100) AZ,A1,A2,A3,A4
100   FORMAT(8E12.4)
      DO 999 N=1,IT
      DO 10 I=1,NMAX
      DO 10 J=1,NMAX
10    A(I,J)=0.0
      G=GS+DG*(N-1)
      GZ=-AZ*G
      G1=-A1*G
      G2=-A2*g
      G3=-A3*G
      G4=-A4*G
      WRITE(6,101) G
101   FORMAT (2X,'GAMA=',F7.4)
      DO 20 I=1,NMAX
      X(I)=1.0
      E(I)=0.0
      P(I)=0.0
20    A(I,I)=1.0+GZ
      DO 30 I=1,NMAX
      IF(I-4.EQ.0) GO TO 22
      A(I,I-4)=G4
      A(I-4,I)=G4
 22   CONTINUE
      IF(I-3.LE.0) GO TO 31
      A(I,I-3)=G3
      A(I-3,I)=G3
31    CONTINUE
      IF(I-2.LE.0) GO TO 32
      A(I,I-2)=G2
      A(I-2,I)=G2
32    CONTINUE
      IF(I-1.LE.0) GO TO 33
      A(I,I-1)=G1
      A(I-1,I)=G1
33    CONTINUE
30    CONTINUE
      DO 5 I=1,7
```

```
5       WRITE(6,109) (A(I,J),J=1,7)
109     FORMAT(2X,7E10.3)
        CALL ZGE(A,INT,NR,NC,EMACH)
        CALL ZSU(A,INT,X,NR,NC,EMACH)
        NB=(NMAX+1)/2
        C=X(NB)
        DO 38 I=1,NB
38      WRITE(6,102) I,X(I)
102     FORMAT(2X,'I=',I2,2X,'X(I)=',F8.4)
        DO 40 I=1,NMAX
40      X(I)=X(I)/C
        DO 50 I=1,NB
        P(I)=AZ*X(I)+A1*X(I+1)+A2*X(I+2)+A3*X(I+3)+A4*X(I+4)
        IF(I.GT.1) P(I)=P(I)+A1*X(I-1)
        IF(I.GT.2) P(I)=P(I)+A2*X(I-2)
        IF(I.GT.3) P(I)=P(I)+A3*X(I-3)
        IF(I.GT.4) P(I)=P(I)+A4*X(I-4)
50      E(I)=P(I)/PB
        CC=P(NB)
        DO 60 I=1,NB
        P(I)=P(I)/CC
60      WRITE(6,103) I,X(I),P(I),E(I)
103     FORMAT(2X,'I=',I2,2X,'X=',F16.4,2X,'P=',F16.4,2X,'E=',F16.4)
999     CONTINUE
        STOP
        END
```

INDEX

Modern Physics Letters B, Vol. 5, No. 1 (1991) 65–72

PHOTOEMISSION CALCULATION WITH A SIMPLE MODEL FOR THE PHOTON FIELD: APPLICATION TO ALUMINIUM

P. DAS, R. K. THAPA* AND N. KAR
Department of Physics, University of North Bengal, Siliguri, West Bengal 734 430 India

Received 26 September 1990

Photoemission cross-sections are calculated, using a simple "local" dielectric function for computing the photon field in the surface region and free electron wavefunctions. Comparisons are made with the experimental data for the frequency-dependent normal photoemission from the Fermi level of aluminium, and the importance of the variation of the photon field in the surface region is pointed out.

1. Introduction

Photoemission experiments on surfaces of solids are basically concerned with the excitation of electrons by the incident photon energy. A simple calculation of photo-current (in one-electron approximation) involves the evaluation of matrix elements of the form $\langle\psi_i|H'|\psi_f\rangle$, where $|\psi_i\rangle$ and $|\psi_f\rangle$ denote the initial and final one-electron states whose energies are connected by $E_f - E_i = \hbar\omega$ and $H' = (e/2mc).(\mathbf{p}.\mathbf{A} + \mathbf{A}.\mathbf{p})$, $\mathbf{p}$ being the one-electron momentum operator and $\mathbf{A}$, the vector potential associated with the photon field. The states $|\psi_i\rangle$ and $|\psi_f\rangle$ are modified from the bulk-states by the presence of the surface. Similarly, the photon field also has a spatial variation in the surface region.

In standard photoemission calculations,[1,2] the one-electron states are calculated with a high degree of accuracy — but the variation of the photon field is generally neglected. Depending on the type of experimental data one intends to compare the calculation with, this may or may not be a reasonable approximation. In the case where one looks at the photoemission current as a function of photon energy with a constant initial state, the photon field variation in the surface region needs to be considered more carefully. However, a first principles calculation of the electromagnetic field in the presence of a surface is an extremely complex problem — only for the case of jellium the results are available.[3,4] Bagchi and Kar, on the other hand, computed the field in a simple "local" model, using experimentally determined frequency-dependent dielectric

PACS No.: 79.60
*Present address: Department of Physics, Pachhunga University College, Aizawl, Mizoram 796001, India

functions as parameter, and they used this for calculation of photo-current from the surface state of tungsten.[5] This simple model is applicable to those elements for which the frequency-dependent dielectric functions are known. In this paper, we use this model in conjunction with free-electron wavefunctions for electron states and show that the results obtained agree qualitatively with experimental data and the theoretical results obtained by more sophisticated jellium field calculations. This would indicate that we may use the simple model for calculation of photoemission cross-sections of other metals for which the jellium results would not be applicable.

2. Formalism

The golden-rule expression for the current density[6] may be written as

$$\frac{di(E)}{d\Omega} = \frac{2\pi}{\hbar} \sum |\langle \psi_f | H' | \psi_i \rangle|^2 \delta(E - E_f)\, \delta(E_f - E_i - \hbar\omega) f_0(E - \hbar\omega)[1 - f_0(E)] \,, \tag{1}$$

where H' is the perturbation responsible for photoemission by radiation of frequency ω, $|\psi_i\rangle$ and E_i refer to the initial state wavefunction and energy and $|\psi_f\rangle$ and E_f to the final state wavefunction and energy, and $f_0(E)$ denotes the Fermi occupation function. We are considering the photoemission to take place along z-axis, which is normal to the surface. We may therefore write H' as

$$H' = (e/mc)\left[\tilde{A}_\omega(z)\frac{d}{dz} + \frac{1}{2}\frac{d}{dz}\tilde{A}_\omega(z)\right], \tag{2}$$

where $\tilde{A}_\omega(z) = \dfrac{A_\omega{}^z(z)}{A_0}$ with $A_\omega{}^z(z)$ as the component of vector potential along z-axis, and A_0 is the amplitude of the incident beam. The formula for photoemission cross-section can be written as

$$\frac{d\sigma}{d\Omega} \approx \frac{k^2}{\omega} |\langle \psi_f | \tilde{A}_\omega(z) \frac{d}{dz} + \frac{1}{2}\frac{d}{dz}\tilde{A}_\omega(z) | \psi_i \rangle|^2 \,. \tag{3}$$

The model of Bagchi and Kar is employed for the computation of $\tilde{A}_\omega(z)$. We assume the z-direction to be perpendicular to the nominal surface which is chosen as $z = 0$. The metal is assumed to occupy all space to the left of the $z = 0$ plane. The response of the electromagnetic field is bulk-like everywhere except in the surface region defined by $-a \leq z \leq 0$. In this region the model dielectric function is chosen to be a local one which interpolates linearly between the bulk value inside the metal and the vacuum value (unity) outside. The model frequency-dependent dielectric function is therefore given by

$$\varepsilon(\omega) \equiv \varepsilon_1(\omega) + i\varepsilon_2(\omega) \qquad \text{for } z < -a \,,$$

$$\varepsilon(\omega, z) = 1 + [1 - \varepsilon(\omega)]z/a \quad \text{for} \quad -a \leq z \leq 0 \ ,$$
$$1 \quad \text{for} \quad z > 0 \ . \tag{4}$$

For the complex dielectric function $\varepsilon(\omega, z)$ we use the experimental values given by Weaver.[7] We consider p-polarized light to be incident on the surface plane making an angle θ_i with z-axis. The calculated vector potential of interest, $\tilde{A}_\omega(z)$, in the long-wavelength limit $(\omega a/c) \to 0$ is

$$\tilde{A}_\omega(z) = \begin{cases} -\dfrac{\sin 2\theta_i}{[\varepsilon(\omega) - \sin^2\theta_i]^{1/2} + \varepsilon(\omega)\cos\theta_i} \ , & z < -a \\ -\dfrac{\sin 2\theta_i}{[\varepsilon(\omega) - \sin^2\theta_i]^{1/2} + \varepsilon(\omega)\cos\theta_i} \dfrac{a\,\varepsilon(\omega)}{[1 - \varepsilon(\omega)]z + a} \ , & -a \leq z \leq 0 \\ -\dfrac{\varepsilon(\omega)\sin 2\theta_i}{[\varepsilon(\omega) - \sin^2\theta_i]^{1/2} + \varepsilon(\omega)\cos\theta_i} \ , & z > 0 \ . \end{cases} \tag{5}$$

This expression is to be used in the evaluation of the matrix element.

To evaluate the photoemission cross-section we also need the initial and final state wavefunctions. These are calculated in the free electron model with the potential given by

$$V(z) = V_0\theta(z) \ , \tag{6}$$

where $V_0 = E_F + \phi$, E_F being the Fermi level in the free electron model and ϕ the work function, $\theta(z)$ is the step function, $\theta(z) = 0$ for $z < 0$ and $\theta(z) = 1$ for $z > 0$ (see Fig. 1). By matching the wavefunctions at the surface plane $z = 0$, we may write the initial state wavefunction as

$$\psi_i(r) = \begin{cases} (m/2\pi\hbar^2 k_i)^{1/2} \dfrac{1}{L}\left[e^{ik_i z} + \dfrac{ik_i + \kappa}{ik_i - \kappa} e^{-ik_i z}\right] e^{i\mathbf{k}_\parallel \cdot \mathbf{r}_\parallel} \ , & z < 0 \\ (m/2\pi\hbar^2 k_i)^{1/2} \dfrac{1}{L} \dfrac{2ik_i}{ik_i - \kappa} e^{-\kappa z} e^{i\mathbf{k}_\parallel \cdot \mathbf{r}_\parallel} \ , & z > 0 \ , \end{cases} \tag{7}$$

where $k_i^2 = \dfrac{2m}{\hbar^2} E_i - \mathbf{k}_\parallel^2$, $\kappa^2 = \dfrac{2m}{\hbar^2}(V_0 - E_i) + \mathbf{k}_\parallel^2$, and $\mathbf{k}_\parallel$ and $\mathbf{r}_\parallel$ are the components of $\mathbf{k}$ and $\mathbf{r}$ in the κ-y plane (plane parallel to the surface).

Similarly, the final state wavefunction may be written as

$$\psi_f = \begin{cases} (m/2\pi\hbar^2 q)^{1/2} \dfrac{1}{L} \dfrac{2q}{q + k_f} e^{ik_f z} e^{i\mathbf{k}_\parallel \cdot \mathbf{r}_\parallel} \ , & z < 0 \\ (m/2\pi\hbar^2 q)^{1/2} \dfrac{1}{L}\left[e^{iqz} + \left(\dfrac{q - k_f}{q + k_f}\right) e^{-iqz}\right] e^{i\mathbf{k}_\parallel \cdot \mathbf{r}_\parallel} \ , & z > 0 \end{cases} \tag{8}$$

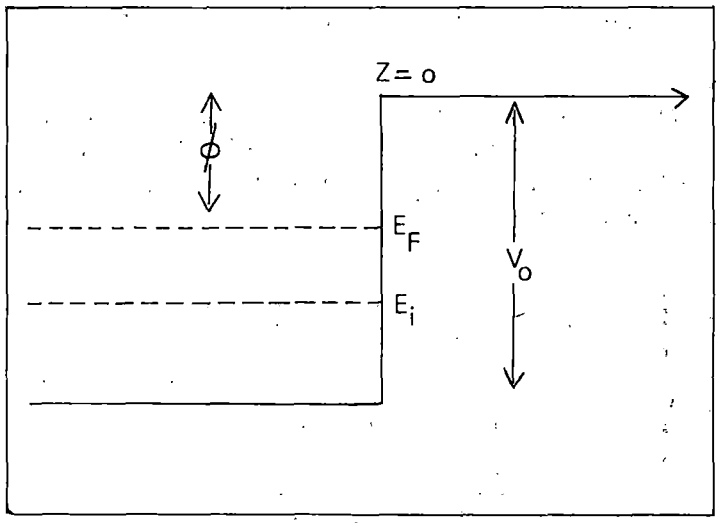

Fig. 1. Model potential used for calculating wavefunctions for initial and final states, $\phi = 4.25$ eV & $V_0 = 15.95$ eV.

where $k_f^2 = \frac{2mE_f}{\hbar^2} - \mathbf{k}_\parallel^2$, $q^2 = \frac{2m}{\hbar^2}(E_f - V_0) - \mathbf{k}_\parallel^2$, $E_f = E_i + \hbar\omega$. The matrix element for photoemission can be evaluated by using the above expressions for the vector potential and the wavefunctions. However, to ensure convergence for $z < 0$, one has to introduce a convergence factor due to lifetime effects. This is a standard procedure in low energy electron diffraction and photoemission calculations (see, for example, Pendry[2]). We do it here by introducing a factor $e^{-\alpha|z|}$ (for $z < 0$) in the calculation of the matrix element – this is to take into account the inelastic scattering of electrons.

3. Application

We have applied our results for computing the normal photoemission from the Fermi level of Aluminium, for which experimental results as well as theoretical calculations using jellium model are available. The experimental results are shown in Fig. 2, the data of Levinson *et al.*[8] having been used. For our calculations, we have taken $\phi = 4.25$ eV and $E_F = 16.7$ eV — these values have been given by Ashcroft and Mermin.[9] Since normal photoemission is considered, $\mathbf{k}_\parallel = 0$; also θ_i is taken to be 45° as in the experiment. Our results for the photoemission cross-section are shown in Fig. 3 (with $a = 10$ atomic units). We see that there is qualitative agreement between the experimental data and calculated photo-currents. The calculated curve shows a peak at 11 eV, a

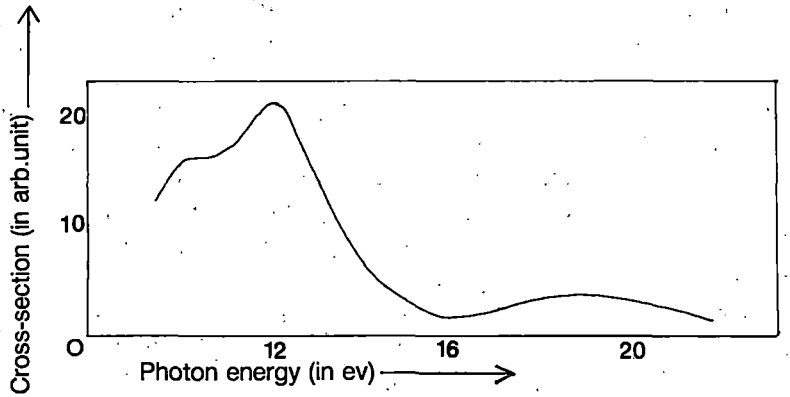

Fig. 2. Experimental data of photoemission cross-section for aluminium for normal emission from Fermi level, (100) face, as a function of photon energy (from Levinson *et al.*[8]).

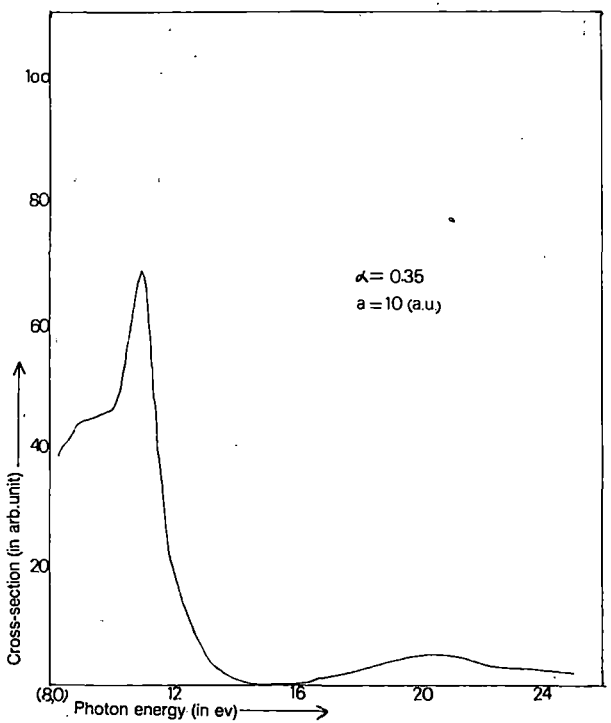

Fig. 3. Calculated photoemission cross-section from Fermi level of aluminium as a function of photon energy.

minimum at 15 eV and again a broad peak around 20.5 eV. These features are also present in the experimental curve — although the shapes of the two curves are different.

We further investigated the origin of the peak at 11 eV in the calculated spectrum and concluded that it is a surface feature. As evidence for that we plot the field $|\tilde{A}_\omega(z)|$ as a function of z in the surface region for $\hbar\omega = 11$ eV (Fig. 4). We see that there is a strong peak in the middle of the surface region. For $\hbar\omega = 15$ eV and 20 eV, on the other hand (Fig. 4), the plot of $|\tilde{A}_\omega(z)|$ does not show any peak in the surface region.

As further evidence of the peak at 11 eV being surface-related, we show the results of a calculation of photo-current with fields given by the Fresnel refraction formulae at the surface, i.e., the fields are given by

$$\tilde{A}_\omega(z) = \begin{cases} -\dfrac{\sin 2\theta_i}{[\varepsilon(\omega) - \sin^2\theta_i]^{1/2} + \varepsilon(\omega)\cos\theta_i}, & z < 0 \\ -\dfrac{\varepsilon(\omega)\sin 2\theta_i}{[\varepsilon(\omega) - \sin^2\theta_i]^{1/2} + \varepsilon(\omega)\cos\theta_i}, & z > 0\,, \end{cases} \tag{9}$$

and the (free-electron) wavefunctions are the same as in Eqs. (7) and (8). We see that, although there is a minimum around 12 eV, there is no peak around

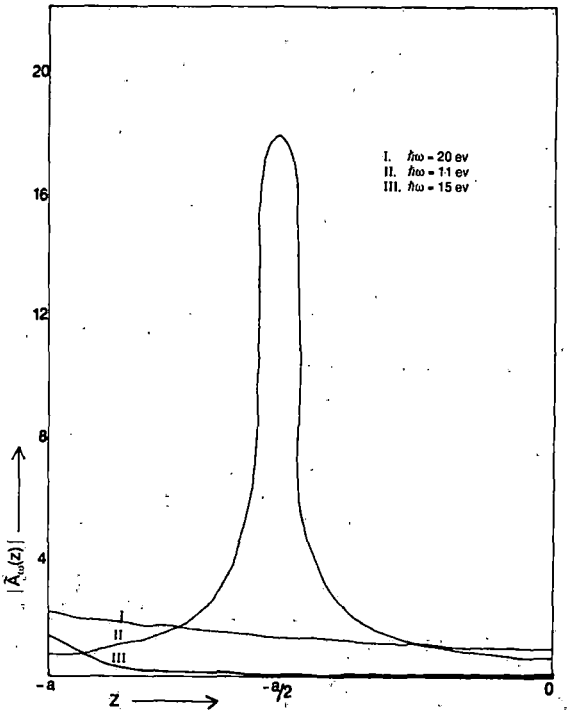

Fig. 4. Plot of $|\tilde{A}_\omega(z)|$ vs. z in the surface region for $\hbar\omega = 11$ eV, 15 eV and 20 eV.

11–12 eV (Fig. 5). Above the plasmon frequency, the curve shows a peak which is much more pronounced than that in the calculation with a surface region. The peak in the experimental data above the plasmon frequency is also much less pronounced. Anyway, it is quite clear that the calculations with the simple Fresnel refraction formulae is not even qualitatively correct – in particular it completely fails to reproduce the peak around 11–12 eV.

We have thus shown that with a simple local model for the dielectric function, we can get a qualitative agreement with experimental data. There have been previous calculations, notably by Levinson *et al.*[8] and Barberan and Inglesfield[10] for aluminium. The calculations of Levinson *et al.*, employing the self-consistent jellium model for fields in the surface region are more sophisticated and their results are in better agreement with the experimental data. However, the calculations for jellium cannot be extended to more complicated cases, e.g., transition metals or semiconductors, while the model we have employed can be extended to these cases. So the qualitative agreement we obtain in aluminium and the previous application to the case of tungsten gives us confidence to apply our model to photoemission calculations for other metals and semiconductors. However, for these cases, we cannot use free electron wavefunctions any more.

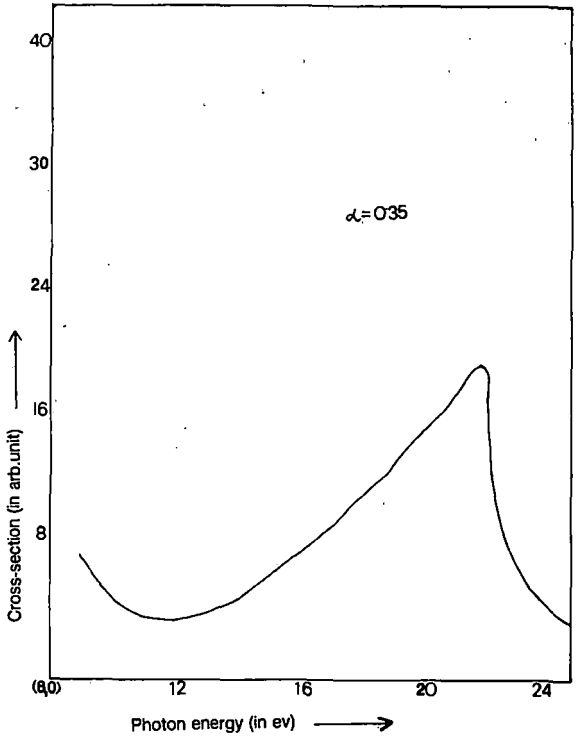

Fig. 5. Photoemission cross-section from Fermi level of aluminium with Fresnel fields.

We are working to combine a better description of the wavefunction with the field given by this model for photo-current calculations of other metals.

In conclusion, although there are shortcomings in the model for electromagnetic field employed here (for example, since experimentally measured dielectric functions are used as inputs, the origin of the surface-related peak cannot be exactly pin-pointed) — it gives results in reasonable agreement with experimental data, and has the potential of being used for a number of metals and semiconductors.

Acknowledgement

One of the authors (N. K.) acknowledges a grant from Council of Scientific and Industrial Research, India.

References

1. A. Liebsch, *Phys, Rev. Lett.* **32** (1974) 1203.
2. J. B. Pendry, *Surf. Sci.* **57** (1976) 679; see also J. B. Pendry in *Photoemission and the Electronic Properties of Surfaces*, eds, B. Feurbacher, B. Fitton and R. F. Willis (Wiley, NY, 1978).
3. P. J. Feibelman, *Phys. Rev. Lett.* **34** (1975) 1092; *Phys. Rev.* **B12** (1979) 1319.
4. G. Mukhopadhayay and S. Lundquist, *Solid State Commun.* **21** (1977) 629.
5. A. Bagchi and N. Kar, *Phys. Rev.* **B18** (1978) 5240.
6. D. R. Penn, *Phys. Rev. Lett.* **28** (1972) 1041.
7. J. Weaver in *Handbook of Chemistry and Physics of Solids* (CRC Press Boca Raton, Ohio, 1987) E-377.
8. H. J. Levinson, E. W. Plummer and P. J. Feibelman, *Phys. Rev. Lett.* **43** (1979) 953 and *J. Vac. Sci. Technol.* **17** (1980) 216.
9. N. W. Ashcroft and N. D. Mermin, *Solid State Physics*, (Holt, Reinhart and Winston, NY, 1976) p. 38.
10. N. Barberan and J. E. Inglesfield, *J. Phys.* **C14** (1981) 3114.

phys. stat. sol. (b) **187**, 551 (1995)

Subject classification: 71.10 and 79.60; S4

Department of Physics, North Bengal University, Siliguri[1])

Photoemission Calculations Including Both Band Structure Effects and Photon Field Variation

By

P. DAS and N. KAR

Photoemission cross-sections are calculated, using band wave functions and a spatially varying photon field. The solid is considered to be composed of a stack of identical layers of atoms parallel to the surface with a potential of muffin-tin form. The photoemission matrix element is calculated by appropriate expansion of the initial and final state wave function and the vector potential of the photon field in the muffin-tin, interstitial, and vacuum regions. The case of normal photoemission from the (100) face of aluminium is considered as an application.

1. Introduction

Experimental data from angle-resolved photoemission measurements have been very useful in surface physics, and to analyze the data, methods for photoemission calculation [1, 2] have been developed where the wave functions for the semi-infinite solid are constructed accurately. However, the variation of the photon field is generally neglected in such calculations. An accurate calculation of the electromagnetic field in the surface region is itself a complex problem and first principles calculations are available [3, 4] only for jellium. It has not been possible so far to construct a theory of photoemission incorporating both LEED-type wave functions and RPA-type field calculation. In any case, transition metals and semiconductors would be beyond the purview of such calculations.

On the other hand, empirical calculations of fields near surfaces with 'local' dielectric function have been used to explain certain qualitative features of photoemission data for tungsten [5], palladium [6], and aluminium [7]. Even with simplistic wave functions, using the measured energy-dependent dielectric function, this approach has been reasonably successful.

This work is an improvement on our previous photocurrent calculations [7] using free electron states. Here we have included the crystal potential in muffin-tin form to calculate the initial state wave function. The formalism has been applied to the case of normal photoemission of electrons at the Fermi level from the (100) face of aluminium and the results have been compared with experimental data as well as previous calculations.

2. Scheme of Calculations

The photoemission cross-section can be written, in the Golden Rule approximation [8], as

$$\frac{\mathrm{d}j(E)}{\mathrm{d}\Omega} = \frac{2\pi}{\hbar} \sum_{\mathrm{f,i}} |\langle \psi_\mathrm{f}| H' |\psi_\mathrm{i}\rangle|^2 \, \delta(E - E_\mathrm{f}) \, \delta(E_\mathrm{f} - E_\mathrm{i} - \hbar\omega) \, f_0(E - \hbar\omega) \, [1 - f_0(E)] \,, \tag{1}$$

[1]) Siliguri 734430, West Bengal, India.

where ψ_i and ψ_f are the initial and final states and $H' = (e/2mc)(\boldsymbol{A}\cdot\boldsymbol{p} + \boldsymbol{p}\cdot\boldsymbol{A})$, $\boldsymbol{A}$ being the vector potential of the photon field and $\boldsymbol{p}$ the one-electron momentum operator. To evaluate the matrix element we have to construct ψ_f and ψ_i and to determine $\boldsymbol{A}$.

We shall assume the solid to be composed of a stack of identical layers of atoms parallel to the surface. Further, within each layer there is one atom per unit cell and the centres of all the atoms lie in the same plane parallel to the surface. We consider the crystal potential to be of muffin-tin form. This description is the same as that for many standard photoemission calculations, e.g. Pendry [2, 9], and we may use the same form for the wave function in each layer.

2.1 Initial and final state wave functions

For each layer, we expand the wave functions in spherical harmonics inside the muffin-tin sphere and in the interstitial regions, since the potential is constant, the wave functions can be expanded into forward and backward travelling plane waves. For the vacuum region, the initial state wave function can be constructed by considering a wave function decaying exponentially outside the surface. With the centre of the muffin-tin sphere in the layer chosen as the origin, the initial state wave function may be written as

$$\psi_i(\boldsymbol{r}) = \begin{cases} \sum_L Z_L f_1(R)\, Y_L(\theta,\varphi)\,; & \text{spherical region}\,, \\ \sum_g [u_g\, e^{iK_g^+\cdot R} + v_g\, e^{iK_g^-\cdot R}]\,; & \text{interstitial region}\,, \\ \sum_g T_g\, e^{iK_g\cdot(r-r_0)_\parallel}\, e^{-\chi_g(z-z_0)}\,; & \text{vacuum region}\,, \end{cases} \tag{2}$$

where

$$\boldsymbol{K}_g^{\pm} = [(\boldsymbol{k}+\boldsymbol{g})_\parallel, \pm\sqrt{2(E_i - V_0) - |\boldsymbol{k}+\boldsymbol{g}|_\parallel^2}]\,,$$

$$\chi_g = \sqrt{-[2E_i - (\boldsymbol{k}+\boldsymbol{g})_\parallel^2]}\,, \quad \text{and} \quad \boldsymbol{R} = \boldsymbol{r} - \boldsymbol{c}_j\,,$$

with $\boldsymbol{g}$ denoting two-dimensional reciprocal lattice vectors and $\boldsymbol{K}_g^{\pm}$ the wave vector of the emitted electrons. $\boldsymbol{c}_j$ is the origin at the j-th layer and V_0 the constant interstitial potential with respect to vacuum. u_g, v_g are determined by LEED-type band structure calculations. Z_L, T_g etc. are determined by matching at the appropriate surface. Here $z = z_0$ is the surface plane with respect to the origin in the first layer.

The final state wave function may also be determined as in LEED calculations, but for computational simplicity we have taken it to be in free electron form. Since we want to apply this method to cases where the principal effect is due to the spatial variation in the photon field, we expect this approximation not to affect our results qualitatively. We may write the final states as [7]

$$\psi_f(\boldsymbol{r}) = \begin{cases} e^{i\boldsymbol{q}\cdot(\boldsymbol{r}-\boldsymbol{r}_0)} + \dfrac{q - k_f}{q + k_f}\, e^{-i\boldsymbol{q}\cdot(\boldsymbol{r}-\boldsymbol{r}_0)}\,; & z > z_0\,, \\ \dfrac{2q}{q + k_f}\, e^{i\boldsymbol{k}_f\cdot(\boldsymbol{r}-\boldsymbol{r}_0)}\,; & z < z_0\,, \end{cases} \tag{3}$$

where

$$k_f^2 = \frac{2mE_f}{\hbar^2} - k_\parallel^2\,, \qquad q^2 = \frac{2m}{\hbar^2}(E_f - V_0) - k_\parallel^2\,, \qquad E_f = E_i + \hbar\omega\,.$$

2.2 *Photon field*

To compute the photon field we use the simple model given by Bagchi and Kar [5] where the metal is assumed to occupy all the space to the left of the surface plane $z = z_0$ and the extent of the surface region is $-a \leqq z \leqq z_0$. We may write the expression for the photon field for the p-polarized light in the long-wavelength limit as

$$A(z) = \begin{cases} A_1\,; & \text{bulk region}\,, \\ \dfrac{A_1\varepsilon(\omega)/[1-\varepsilon(\omega)]}{\dfrac{z}{a}+\beta}\,; & \text{surface region}\,, \\ A_1\varepsilon(\omega)\,; & \text{vacuum region}\,, \end{cases} \tag{4}$$

where A_1 and β are constants, depending on the dielectric function ε, the photon energy $\hbar\omega$, and the angle of incidence θ. We have taken the surface region to be the same as the first layer, otherwise the evaluation of the matrix element becomes too cumbersome. We may also consider the surface layer to be equal to an integral number of layers. Although we are using this form for the vector potential, any vector potential which is a function only of the coordinate normal to the surface may be used.

2.3 *Matrix element*

We may write down the matrix element (in (1)) for the solid as a whole,

$$\langle\psi_\mathrm{f}|\,H'\,|\psi_\mathrm{i}\rangle = \int_{\text{vac.}} \psi_\mathrm{f}^* H'\psi_\mathrm{i}\,\mathrm{d}^3r + \int_{\text{surf.}} \psi_\mathrm{f}^* H'\psi_\mathrm{i}\,\mathrm{d}^3r + \sum_j \int_{\text{bulk}} \psi_\mathrm{f}^* H'\psi_\mathrm{i}\,\mathrm{d}^3r\,, \tag{5}$$

where in each region the wave functions and the vector potentials corresponding to that region have to be used. For the vacuum region the integration can be performed analytically with the appropriate forms for ψ_i, ψ_f, and A. Inside each layer, the integration has to be performed over both the spherical and the interstitial regions.

The evaluations of the integral over the interstitial region is somewhat more complicated because of the shape of the region. To do it, we perform the integration over the whole layer, using the form ψ_i for the interstitial region, then subtract the contribution from the muffin-tin sphere.

The integration over the whole layer is simple and comes out as a one-dimensional integration given by

$$T_1 = p_1 S_0 \int_{z_1}^{z_0} \left[\frac{iK_{gz}^+}{\dfrac{z}{a}+\beta} \{u_0\,\mathrm{e}^{iK_{gfz}^+ z} - v_0\,\mathrm{e}^{iK_{gfz}^- z}\} - \frac{1}{2a\left(\dfrac{z}{a}+\beta\right)^2} \{u_0\,\mathrm{e}^{iK_{gfz}^+ z} + v_0\,\mathrm{e}^{iK_{gfz}^- z}\} \right] \mathrm{d}z\,, \tag{6}$$

where

$$p_1 = \frac{2qA_1\varepsilon\,\mathrm{e}^{i\boldsymbol{k}_\mathrm{f}\cdot\boldsymbol{r}_0}}{(q+k_\mathrm{f})(1-\varepsilon)} \quad \text{and} \quad \boldsymbol{K}_{gf}^{\pm} = \boldsymbol{K}_g^{\pm} - \boldsymbol{k}_\mathrm{f}\,,$$

where S_0 is the area of the surface unit cell and z_1 the layer boundary between the first and second layers.

For evaluating the integral over the muffin-tin sphere, we have to expand wave functions and the z-component of the vector potential spherically. For ψ_i or ψ_f we use the following standard expansion:

$$e^{iK_g^{\pm}\cdot r} = 4\pi \sum_L i^l j_l(|K_g^{\pm}|\, r)\, Y_{lm}(r)\, Y_{lm}^*(K_g^{\pm})\,. \tag{7}$$

To express A_z in spherical coordinates, we write it in the following form:

$$A_z(z) = A_z(r\cos\theta) = \frac{1}{\dfrac{r}{a}\cos\theta + \beta} = \sum_l B_l(r)\, P_l(\cos\theta) \tag{8}$$

with

$$B_l(r) = \frac{2}{2l+1}\int_0^{\pi} A_z(r\cos\theta)\, P_1(\cos\theta)\sin\theta\, d\theta\,.$$

We have calculated the coefficient $B_l(r)$ analytically using standard integration tables [10]. The values of $B_l(r)$ for $l = 0$ and $l = 1$ are given by

$$B_0(r) = \frac{2a}{r}\ln\left[\frac{\dfrac{r}{a}+\beta}{-\dfrac{r}{a}+\beta}\right], \qquad B_1(r) = \frac{2}{3}\left[\frac{2a}{r} - \beta\left(\frac{a}{r}\right)^2 \frac{\dfrac{r}{a}+\beta}{-\dfrac{r}{a}+\beta}\right]. \tag{9}$$

The terms involving A_z' may also be evaluated similarly in terms of $D_l(r)$.

We calculate the matrix element in the muffin-tin region using the interstitial wave functions for the initial state. This term may be written as

$$T_2 = 8\pi p_1 \sum_{g,l} \frac{i^l}{2l+1} \times \left[\left\{iK_{gz}^{+}\int_0^{r_m}\left[u_g P_l(K_p^{+})\, j_l(|K_{gf}^{+}|\, r) - v_g P_l(K_p^{-})\, j_l(|K_{gf}^{-}|\, r)\right] B_l(r)\, r^2\, dr\right\} - \left\{\frac{1}{2a}\int_0^{r_m}\left[u_g P_l(K_p^{+})\, j_l(|K_{gf}^{+}|\, r) + v_g P_l(K_p^{-})\, j_l(|K_{gf}^{-}|\, r)\right] D_l(r)\, r^2\, dr\right\}\right], \tag{10}$$

where $K_p^{\pm} = K_{gf}^{\pm}\cdot\hat{z}$ and r_m is the muffin-tin radius.

Using the radial wave functions for the initial state inside the muffin-tin sphere we calculate the integration as a product of a radial part, which has to be evaluated numerically and another one involving the Clebsch-Gordan coefficients. The integral may be written as

$$T_3 = 8\pi p_1 \sum_{L_1,l_2,L_3} \frac{Z_{L_3}(-i)^{l_1}\, Y_{L_1}(k_f)}{2l_2+1}\int_0^{r_m}\left[\left\{C_{L_1 l_2 L_3}^{1}\left[\frac{\partial}{\partial r} f_{L_3}(r)\right] r^2 + C_{L_1 l_2 L_3}^{2} f_{l_3}(r)\, r\right\} \times B_{l_2}(r) - \frac{1}{2a}\, C_{L_1 l_2 L_3}^{3} f_{l_3}(r)\, r^2 D_{l_2}(r)\right] j_{l_1}(k_f r)\, dr\,, \tag{11}$$

where C_l are the Clebsch-Gordan coefficients. Therefore, the surface layer contribution to the matrix element can be obtained from the relation $T_s = T_1 - T_2 + T_3$.

For the bulk layers the matrix element can similarly be calculated for the muffin-tin and interstitial regions but since the photon field is a constant here, integrations are simpler compared to that for the surface layer. Almost all of these integrations have to be performed numerically.

3. Application

We have applied this method to normal photoemission from the Fermi level of aluminium as a function of photon energy. The muffin-tin potential and the crystal parameters used are those given by Pendry [9]. For the band structure calculation the imaginary part of the crystal potential has been taken to be zero.

For the photon field calculation, the data given by Weaver [11] for the complex dielectric function of aluminium as a function of photon energy were used. Since the final state was taken to be free electron like, a convergence factor of exp $(-\alpha z)$ was introduced in the final state. We have taken [12] $E_f = 11.7$ eV, $V_0 = 15.95$ eV, and the lattice constant for aluminium as 0.405 nm. In Fig. 1 we show the result [13] obtained for normal photoemission ($k_{\|} = 0$) for a p-polarized photon incident at 45° to the surface normal. The two curves shown correspond to two different values for the parameter a defining the surface region in the field calculation (4). The curve with open circles is for a taken to be the same as the thickness of the first layer while the plot with filled circles is for a equal to the thickness of the first two layers. We note here that we have taken the first layer width to be different from the other layers — this was done so that the surface plane can be taken to be tangential to the last layer of muffin-tins. The scales of photocurrent for the two curves are not the same, we have plotted them so that the peaks around 11 eV are of comparable height. The value of α was taken to be 0.35 (the same value used earlier with free electron initial and final states).

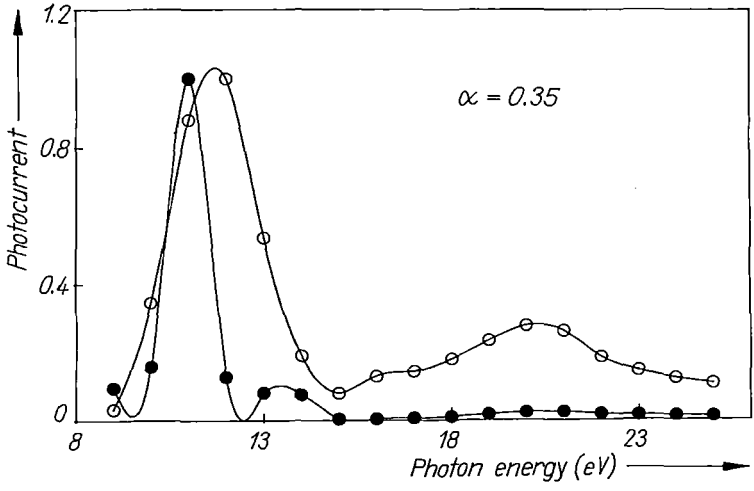

Fig. 1. Variation of the photocurrent (arb. units) with photon energy for normal photoemission from the Fermi level of the aluminium (100) face with the surface region a for field variation. Open circles for a taken equal to the thickness of the first layer, full circles for a equal to the thickness of the first two layers

The calculated photocurrent shows a peak at 11.5 eV followed by a minimum at the plasmon energy ($\approx$16 eV) and a broad maximum around 20 eV. We have seen that these features are also present in the experimentally observed results [14, 15] and in our previously calculated [7] photocurrents. In the experimental curve for the photocurrent, we have seen that the ratio of the peak heights of the two peaks (below and above the plasmon energy) is of the order of 6 and in our previous result it was 15 but now this ratio comes out to be $\approx$3.6 for a equal to the thickness of the first layer only and $\approx$23 for a equal to the thickness of the first two layers.

So, we may conclude that use of band wave functions gives better agreement compared to previous calculations with free electron wave functions. From Fig. 1 it is evident that the field variation may be taken to be over the first layer only, at least with this model. For a complete calculation of photocurrent we have included LEED-type final states and work for that is in progress part of which has already been reported.

Acknowledgements

Some of the subroutines and the muffin-tin potential for aluminium have been taken from the book Low Energy Electron Diffraction written by Pendry [9]. One of the authors (P. D.) thanks CSIR, India for a research fellowship and the other author (N. K.) thanks CSIR for a research grant.

References

[1] A. LIEBSCH, Phys. Rev. Letters **32**, 1203 (1974).
[2] J. B. PENDRY, Surface Sci. **57**, 679 (1976); Photoemission and the Electronic Properties of Surfaces, Ed. B. FEURBACHER, B. FITTON, and R. F. WILLIS, Wiley, New York 1978.
[3] P. J. FEIBELMAN, Phys. Rev. Letters **34**, 1092 (1975); Phys. Rev. B **12**, 1319 (1975).
[4] G. MUKHOPADHYAY and S. LUNDQUIST, Solid State Commun. **21**, 629 (1977).
[5] A. BAGCHI and N. KAR, Phys. Rev. B **18**, 5240 (1978).
[6] R. K. THAPA, phys. stat. sol. (b) **179**, 391 (1993).
[7] P. DAS, R. K. THAPA, and N. KAR, Mod. Phys. Letters B **5**, 65 (1991).
[8] D. R. PENN, Phys. Rev. Letters **28**, 1041 (1972).
[9] J. B. PENDRY, Low Energy Electron Diffraction, Academic Press, London 1974.
[10] I. S. GRADSHTEYN and I. M. RYZHIK, Tables of Integrals, Academic Press, London/New York 1980.
[11] J. WEAVER, Handbook of Chemistry and Physics of Solids, CRC Press, Inc., Boca Raton (Ohio) 1978 (E-377).
[12] N. W. ASHCROFT and N. D. MERMIN, Solid State Physics, Holt, Reinehart, and Winston Publ., New York 1976 (p. 38).
[13] P. DAS, DAE SSP Symp. '93, **46**, 36C (1993).
[14] H. J. LEVINSON, E. W. PLUMMER, and P. J. FEIBELMAN, Phys. Rev. Letters **43**, 953 (1979); J. Vacuum Sci. Technol. **17**, 216 (1980).
[15] N. BARBERAN and J. E. INGLESFIELD, J. Phys. C **14**, 3114 (1981).

(Received June 24, 1994)

Modern Physics Letters B, Vol. 6, No. 20 (1992) 1263–1272

DIPOLAR FIELDS NEAR THE SURFACE FOR CRYSTALS WITH SIMPLE HEXAGONAL, HEXAGONAL CLOSE-PACKED AND DIAMOND STRUCTURE

P. DAS and N. KAR
Physics Department, North Bengal University, Siliguri, West Bengal 734 430, India

Received 7 July 1992

The dipolar local field near the surface for simple hexagonal, hexagonal close-packed and diamond structure has been computed by considering a slab geometry. The technique of plane by plane summation for dipolar fields has been used and self-consistent field determined with large enough number of layers.

The local, or effective electric field for a polarizable infinite lattice has been studied for a long time (see for example, Born and Wolf[1]). The self-consistent local electric field near the surface of a dipolar lattice for simple cubic, face-centred and body centred cubic structures have also been calculated.[2] In this paper, we consider three other structures, simple hexagonal, hexagonal close-packed (hcp) and diamond structure. The first two do not belong to the cubic system and so the Lorentz–Lorenz relation is not expected to hold (although, for the "ideal" hcp structure, the relation does hold); the Bravais lattice for the diamond structure is face-centred cubic, but the fact that there exists a two-atom basis means that in addition to the atomic sites for the face-centred cubic structure there would be an equal number of atoms in other sites and the local field in the surface plane is quite different from the face-centred cubic case, as we shall discuss later.

The procedure for calculating the self-consistent local field is essentially the same as in Ref. 2; we have also used similar notations. A slab geometry of finite number of lattice plane have been considered — the lattice planes are assumed to be infinite, parallel to the surface. We have considered an electric field normal to the surface plane; the polarizability tensor was assumed to be diagonal; the molecules in each site would be polarized — these were taken as point dipoles — and all the dipoles lying in one plane would be parallel to one another and would have the same magnitude. The first step is to compute the field from an infinite two-dimensional lattice of parallel dipoles of equal moment. This can be evaluated either by explicit sum within a finite region and approximating the rest by an integration

PACS No.: 78.20.

with uniform dipole density[3] or by transforming the discrete lattice sum to a highly convergent sum analytically.[4–6] We have used the former technique to evaluate the two-dimensional lattice sum.

Let us denote different planes by the index ν and take $\mathbf{P}_\nu$ to be the local dipole moment density for the lattice plane ν. We shall consider $\nu = 0$ to be the reference plane—positive values of ν denote planes with a positive value of z (above the reference plane) and negative ν values refer to planes below the reference plane. We shall consider an applied field $\mathbf{E}_0 = E_0 \hat{z}$ in the z-direction. The field from the dipoles in the plane ν will depend linearly on P_ν and the z-component of the total contribution of all the dipole fields may be written as

$$E_{d,z} = \sum\nolimits_\nu \xi_\nu P_\nu \,, \tag{1}$$

where the sum over ν includes in principle all the planes in the slab we are considering and the coefficient ξ_ν has to be determined for each lattice structure. However, only a few of the ξ_ν's have non-zero values—at least to the accuracy we are concerned with. We shall give expressions for evaluating ξ_ν for each of the structures we consider.

We now consider a slab of L lattice planes. The local electric field at a lattice point in the μth plane, ($\mu = 1, 2, \ldots L$) may be written as

$$E^\mu_{\mathrm{loc},z} = E_0 + \sum\nolimits_\nu \xi_{\mu-\nu} P_\nu \,, \tag{2}$$

where the sum over ν is from 1 to L (although, in practice, only those terms for which ξ's are non-zero have to be retained).

Taking the volume polarizability to be Γ, the self-consistency condition for the local dipole moment density, given below:

$$P_\mu = \Gamma E^\mu_{\mathrm{loc},z} \tag{3}$$

will yield the matrix equation

$$\sum\nolimits_\nu M_{\mu\nu} P_\nu = \Gamma E_0 \,, \quad \mu = 1, 2, \ldots L \tag{4}$$

where

$$M_{\mu\nu} = [(1 - \Gamma\xi_0)\delta_{\mu\nu} - \Gamma\xi_{\mu-\nu}(1 - \delta_{\mu\nu})] \,. \tag{5}$$

Inversion of the matrix M, where it is permissible, gives us the self-consistent dipole moment density on each plane; in particular, it would give the behaviour near the surface. Then, by using formula (2) we can compute the dipolar field on each plane.

In the following we shall consider the three structures—simple hexagonal, hexagonal close-packed and diamond, separately. In each case we shall give expressions for ξ and compute the self-consistent dipole moment and the dipolar field plane by plane. We shall also discuss the significance of the results obtained.

1. Simple Hexagonal Structure

For the simple hexagonal lattice, the sites in a plane with reference to an origin at a lattice point may be written as

$$\mathbf{R} = a\left[\left(n_1 + \frac{n_2}{2}\right)\hat{x} + \frac{\sqrt{3}}{2}\, n_2 \hat{y}\right] \tag{6}$$

and for any other plane parallel to it, we may write

$$\mathbf{E} = a\left[\left(n_1 + \frac{n_2}{2}\right)\hat{x} + \frac{\sqrt{3}}{2}\, n_2 \hat{y} + \alpha n_3 \hat{z}\right] \tag{7}$$

where $\alpha = c/a$ and the surface is taken to be perpendicular to the z-axis. The electric field due to a dipole of moment $\mathbf{d}_i$ at point $\mathbf{r}_i$ is

$$\mathbf{E}_\mathbf{d} = \sum_i{}' \frac{3(\mathbf{d}_i - \mathbf{r}_i) - r_i^2 \mathbf{d}_i}{r_i^j}\,. \tag{8}$$

If we consider $\mathbf{r}^j$ as the lattice vectors in the reference plane (given by (6)) and noting that if $\mathbf{d}\mu$ is the dipole moment for the dipole in the plane μ, then the dipole moment density for that plane is

$$\mathbf{P} = \frac{2\mathbf{d}_\mu}{\sqrt{3}\,\alpha a^3}\,. \tag{9}$$

We can write the expression for ξ_0 as

$$\xi_0 = -\left(\frac{\sqrt{3}}{2}\,\alpha\right) \sum_{n_1, n_2}{}' \frac{1}{[n_1^2 + n_2^2 + n_1 n_2]^{\frac{3}{2}}} \tag{10}$$

(the point $n_1 = n_2 = 0$ is excluded).

For the other planes, we note that $\xi\mu = \xi - \mu$ and

$$\xi_\mu = \left(\frac{\sqrt{3}}{2}\,\alpha\right) \sum_{n_1, n_2} \frac{3n_3^2\alpha^2 - [n_1^2 + n_2^2 + n_1 n_2 + \alpha^2 n_3^2]}{[n_1^2 + n_2^2 + n_1 n_2 + \alpha^2 n_3^2]^{\frac{5}{2}}} \tag{11}$$

with the plane index $\mu = n_3$. The values of ξ_0, ξ_1, etc. calculated from (10) and (11) are shown in Table 1 for $\alpha = 1.59$ (this value is typical of simple hexagonal structures). These are in agreement with the previously computed values.[4,6] Further, to the accuracy we are interested in, it is necessary to take only ξ_0 and ξ_1 into account, so the sum in (2) would be restricted to $|\mu - \nu| \leq 1$.

We have also calculated P_μ/P_b and E_μ/E_b (where P_b and E_b are the bulk values of the dipole moment and the dipole field) for a 21-layer film with a number of values

Table 1. ξ_μ for various planes for simple hexagonal, hexagonal close-packed and diamond structure.

Plane Index	ξ_μ			
	Hexagonal	Hexagonal close-packed		Diamond
μ	$\alpha = 1.59$	$\alpha = 1.63$	$= 1.86$	
0	−15.6046	−7.8023	−7.8023	−3.1939
1	0.0043	−0.2868	−0.1460	−2.0862
2	0.0000	0.0015	0.0003	−0.5054
3	0.0000	0.0006	0.0000	−0.0062
4	0.0000	0.0000	0.0000	0.0080
5	0.0000	0.0000	0.0000	0.0000

of Γ. (We have seen that 21 layers are enough to ensure convergence; actually, in this case convergence may be achieved even with a fewer number of layers). Except for a very small range near $\Gamma = -0.064$ for which the matrix cannot be inverted, the results look the same—with virtually no change at the surface plane for the dipole moment or the dipolar field. This is not unexpected, since we have seen that $|\xi_0/\xi_1| \sim 3.6 \times 10^3$, almost the entire contribution to the dipolar field comes from the in-plane dipoles, and so there is almost no variation in P_μ/P_b or E_μ/E_b from plane to plane. In Fig. 1, we have plotted E_μ/E_b and P_μ/P_b for $\Gamma = 0.1$, but there is virtually no change if we take any other value of Γ.

3. Hexagonal Close-Packed Structure

For this structure, in addition to the lattice planes for the simple hexagonal case, we have another set of planes halfway between the former ones. The coefficient ξ_0 can be calculated using the same formula (10) as in the case of simple hexagonal structure, with an additional factor of 1/2 which comes in as there are now two atoms per unit cell. The original planes of the simple hexagonal lattice now become even numbered planes, and we may use (11) to calculate ξ_μ, with an additional factor of 1/2 with $\mu = 2n_3$. For the odd-numbered planes we note that the sites may be denoted by the vectors

$$\mathbf{R} = \left(n_1 + \frac{1}{3}\right)\mathbf{a}_1 + \left(n_2 + \frac{1}{3}\right)\mathbf{a}_2 + \left(n_3 + \frac{1}{2}\right)\mathbf{a}_3$$

$$\text{with } \mathbf{a}_1 = a\hat{x}\,, \quad \mathbf{a}_2 = \frac{1}{2}\,a\hat{x} + \frac{\sqrt{3}}{2}\,a\hat{y}\,, \quad \mathbf{a}_3 = c\hat{z}\,.$$

We can then write, for odd planes

$$\xi_\mu = \frac{\sqrt{3}}{4}\,\alpha \sum_{n_1, n_2} \frac{3\alpha^2\left(n_3 + \frac{1}{2}\right)^2 - \left[\left(n_1 + \frac{n_2}{2} + \frac{1}{2}\right)^2 + \frac{3}{4}\left(n_2 + \frac{1}{3}\right)^2 + \alpha^2\left(n_3 + \frac{1}{2}\right)^2\right]}{\left[\left(n_1 + \frac{n_2}{2} + \frac{1}{2}\right)^2 + \frac{3}{4}\left(n_2 + \frac{1}{3}\right)^2 + \alpha^2\left(n_3 + \frac{1}{2}\right)^2\right]^{\frac{5}{2}}} \tag{12}$$

with $\mu = 2n_3 + 1$.

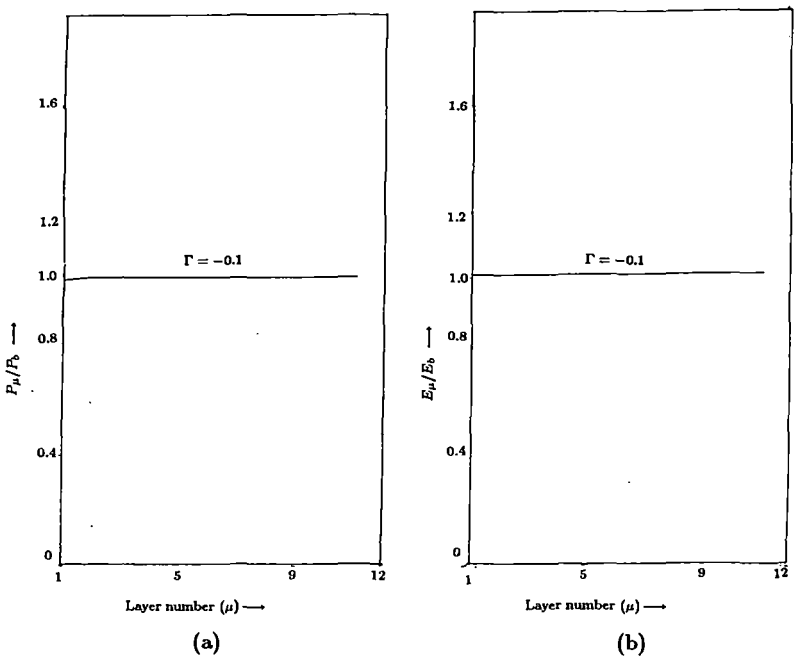

Fig. 1. (a) Variation of dipole moment density, normalized to the uniform bulk value, (P_μ/P_b) against μ, the plane index, for the volume polarizability $\Gamma = -0.1$ in simple hexagonal lattice. (b) Variation of the local dipolar field normalized to its bulk value, (E_μ/E_b) against $\Gamma = -0.1$ in simple hexagonal lattice.

In Table 1, we have shown the computed values of ξ_μ obtained from Eqs. (10), (11) and (12) for two values of α, 1.63 (corresponding to "IDEAL" HCP structure) and 1.86. For cubic symmetry, it is known that

$$\sum\nolimits_\mu \xi_\mu = -\frac{8\pi}{3} \tag{13}$$

which gives the familiar Lorentz–Lorenz result. We note that for the "ideal" HCP structure also, this relation holds, although the symmetry is not cubic. For $\mu = 1.86$ however, the sum over ξ_μ does not give $-8\pi/3$. This is perhaps another illustration of the close relationship between the face-centred cubic and "ideal" hexagonal close-packed structure.

For determining the dipole moment and the dipolar field in the surface region, we have taken a 21 layer slab and constructed the matrix M in (4) and inverted it to obtain the dipole moments P_μ and the dipolar field, layer by layer. It may be mentioned here that taking 21 layer ensures convergence and increasing the number of layers does not change P_μ/P_b or E_μ/E_b, at least to the accuracy we are interested in. For $\alpha = 1.63$, in Fig. 2, we show P_μ/P_b and E_μ/E_b for three values of Γ. Actually the points for integral values of μ are relevant — these points have been joined by lines for visual aid. $\Gamma = -0.10$ and $\Gamma = -0.14$ correspond to

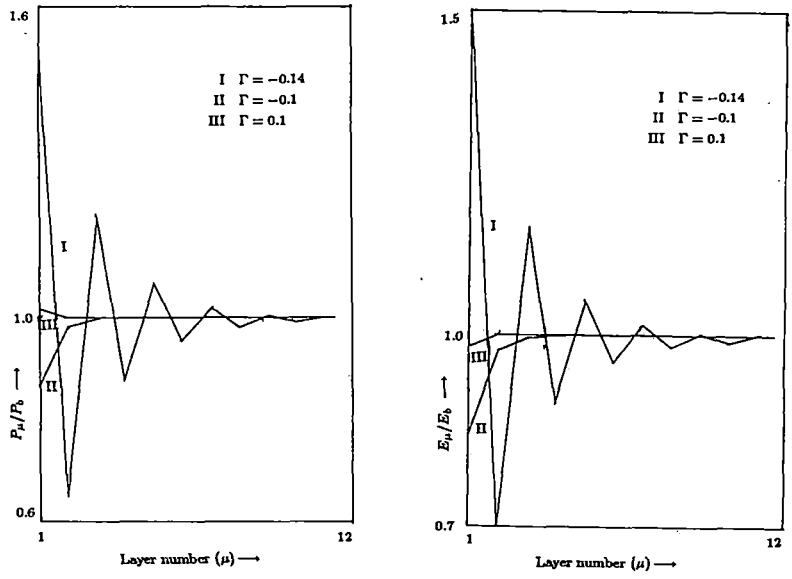

Fig. 2. (a) Variation of P_μ/P_b against μ, the plane index, for $\Gamma = -0.14$, -0.1 and 0.1 in "ideal" hexagonal close-packed structure. (b) Variation of E_μ/E_b against μ, for $\Gamma = -0.14$, -0.1 and 0.1 in "ideal" hexagonal close-packed structure.

values of Γ just beyond the range for which the matrix M may not be inverted. For $\Gamma = -0.14$, i.e., just below the forbidden range, we see the maximum enhancement in the dipolar field for the surface layer, although the enhancement is not very large. The behaviour for both E_μ/E_b and P_μ/P_b is both oscillatory for this value of Γ, again the similarity of behaviour with face-centred cubic case[2] may be noted. For $\Gamma = -0.10$, just above the forbidden range and $\Gamma = 0.1$, the variation in the dipolar field for the surface layer is smaller and the oscillatory behaviour is also absent. For $\alpha = 1.86$, we have plotted P_μ/P_b and E_μ/E_b for the same three values of Γ, and the behaviour is qualitatively the same, but the difference between the surface and bulk values for P_μ (or P_μ) is smaller than for the "ideal" case.

4. Diamond Structure

The diamond structure has the face-centred cubic lattice as the underlying Bravais lattice with a two-atom basis. In this case we have, therefore, in addition to FCC lattice planes, an equal number of planes interspaced between these. For the reference plane, ξ_0 is given by:

$$\xi_0 = -\frac{1}{8}\sum{}'_{n_1,n_2} \frac{1}{\left[\frac{1}{2}(n_1^2+n_2^2)\right]^{\frac{3}{2}}}. \tag{14}$$

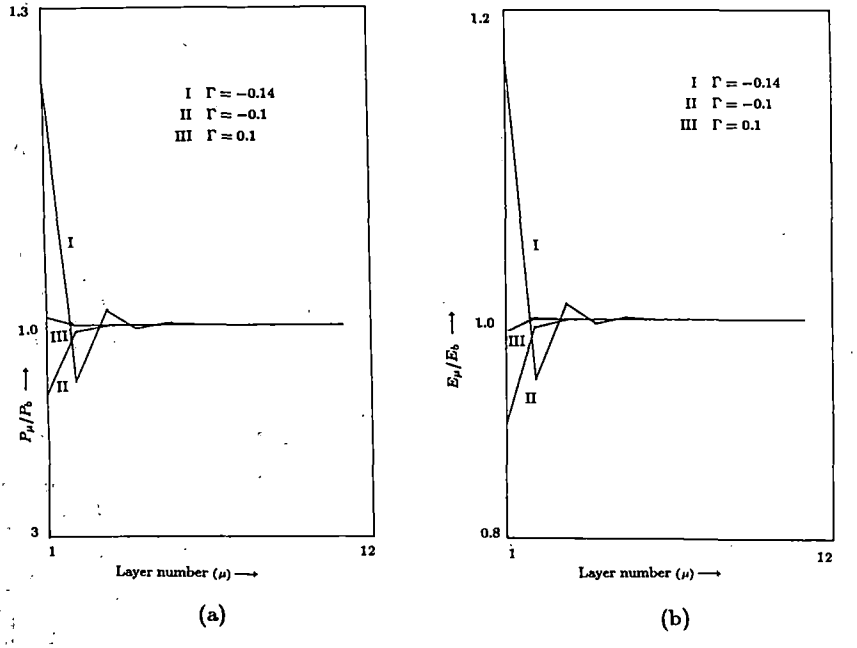

Fig. 3. (a) Variation of P_μ/P_b against μ, for $\Gamma = -0.14$, -0.1 and 0.1 in hexagonal close-packed structure with $\alpha = 1.86$. (b) Variation of E_μ/E_b against μ, for $\Gamma = -0.14$, -0.1 and 0.1 in hexagonal close-packed structure with $\alpha = 1.86$.

For planes located at distance $(n + 1/4)a$ from the reference plane (i.e., 1st plane, 5th plane etc.) we have

$$\xi_\mu = \frac{1}{8} \sum_{n_1,n_2} \frac{3\left(n_3 + \frac{1}{4}\right)^2 - \left[\frac{n_1^2}{2} + \frac{1}{2}\left(n_2 + \frac{1}{2}\right)^2 + \left(n_3 + \frac{1}{4}\right)^2\right]}{\left[\frac{n_1^2}{2} + \frac{1}{2}\left(n_2 + \frac{1}{2}\right)^2 + \left(n_3 + \frac{1}{4}\right)^2\right]^{\frac{5}{2}}} \tag{15}$$

$$\text{with } \mu = 4n_3 + 1 \quad (n_3 = 0, \pm 1, \pm 2, \ldots).$$

For planes at distance $(n + 1/2)a$ from the reference plane (i.e., 2nd, 6th etc.)

$$\xi_\mu = \frac{1}{8} \sum_{n_1,n_2} \frac{3\left(n_3 + \frac{1}{2}\right)^2 - \left[\frac{1}{2}\left(n_1 + \frac{1}{2}\right)^2 + \frac{1}{2}\left(n_2 + \frac{1}{2}\right)^2 + \left(n_3 + \frac{1}{2}\right)^2\right]}{\left[\frac{1}{2}\left(n_1 + \frac{1}{2}\right)^2 + \frac{1}{2}\left(n_2 + \frac{1}{2}\right)^2 + \left(n_3 + \frac{1}{2}\right)^2\right]^{\frac{5}{2}}} \tag{16}$$

$$\text{with } \mu = 4n_3 + 2 \quad (n_3 = 0, \pm 1, \pm 2, \ldots).$$

Similarly, for planes denoted by $\mu = 3, 7, \ldots$ etc.,

$$\xi_\mu = \frac{1}{8} \sum_{n_1,n_2} \frac{3\left(n_3 + \frac{3}{4}\right)^2 - \left[\frac{1}{2}\left(n_1 + \frac{1}{2}\right)^2 + \frac{1}{2}\left(n_2 + 1\right)^2 + \left(\frac{3}{4} + n_3\right)^2\right]}{\left[\frac{1}{2}\left(n_1 + \frac{1}{2}\right)^2 + \frac{1}{2}\left(n_2 + 1\right)^2 + \left(\frac{3}{4} + n_3\right)^2\right]^{\frac{5}{2}}} \tag{17}$$

$$\text{with } \mu = 4n_3 + 3 \quad (n_3 = 0, \pm 1, \pm 2, \ldots)$$

and for planes denoted by $\mu = 4, 8, \ldots$ etc.,

$$\xi_\mu = \frac{1}{8} \sum_{n_1,n_2} \frac{3n_3^2 - \left[\frac{1}{2}(n_1^2 + n_2^2) + n_3^2\right]}{\left[\frac{1}{2}(n_1^2 + n_2^2) + n_3^2\right]^{\frac{5}{2}}} \qquad (18)$$

$$\text{with } \mu = 4n_3 \quad (n_3 = \pm 1, \pm 2, \ldots).$$

The even numbered planes are those in common with the FCC structure—the odd numbered planes are the new ones. As in the previous cases, here also $\xi_\mu = \xi - \mu$; we give the values of ξ_μ in Table 1. Again to the accuracy we are interested, only ξ_0, ξ_1, ξ_2, ξ_3, and ξ_4 (calculated from 14–18) have non-zero values—the rest of them can be taken to be zero. We note also that $\Sigma_\mu \xi_\mu = -8 \cdot \pi/3$ (to 0.05 percent) as is to be expected, since diamond structure has cubic symmetry.

To determine the local field near the surface, we consider for this case a 33 layer slab, we take a larger number of layers as now there are more non-zero ξ_μ's and also because, in contrast to the other cases, the influence of the other two planes above and below the reference plane is comparable to the reference plane itself.

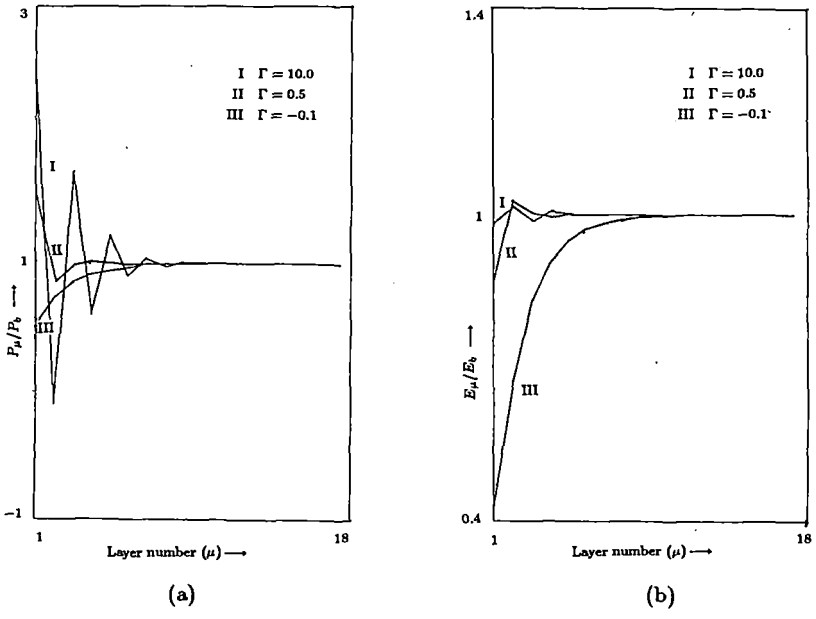

Fig. 4. (a) Variation of P_μ/P_b against μ, the plane index, for $\Gamma = 0.5$, 10.0 and -0.1 in diamond structure. (b) Variation of E_μ/E_b against μ for $\Gamma = 0.5$, 10.0 and 0.1 in diamond structure.

The results for the dipole moment density and the dipolar field obtained by inverting the matrix M also show (Fig. 4) some interesting results. There is a large range of Γ, from $-0.12(\sim -3/8\pi)$ to very large negative values, for which

the inversion process breaks down. We have shown the results for $\Gamma = -0.1$ just above this range. We see the behaviour similar to the other cases—both P_μ/P_b and E_μ/E_b are less than one on the surface plane and monotonically goes to one as we go into the bulk. For large positive values of Γ, $P_{\ddot{\mu}}/P_b$ and $E_{\ddot{\mu}}/E_b$ behave in a different manner. We show in Fig. (4), the results for $\Gamma = 10$. We see that P_μ/P_b has a large oscillatory behaviour. The first layer has a P_μ greater than twice the bulk value, while the second layer has a negative value, i.e., the dipole moment is in the direction opposite that of the bulk! The dipolar field is also oscillatory, but the dipolar fields for the first and second layers are $0.98E_b$ and $1.01E_b$, which is quite a contrast to the behaviour for the dipole moments. This can happen because as we have remarked above, the influence of the two neighbouring planes together is actually greater than that of the reference plane. The oscillations in P_μ are such that their total effect is to make the dipolar field for each layer remains almost the same. For $\Gamma = 0.5$, the results shown in Fig. 4, are similar, but now the oscillations in P_μ/P_b are smaller. For values of Γ larger than 10, the oscillations grow larger and at some stage 33 layers are inadequate to achieve convergence. However, for the values of Γ shown in the Fig. 4 convergence was achieved with 33 layers.

The results for diamond structure are therefore, the most interesting ones. First, there is a large range of Γ for which our procedure breaks down, i.e., for these values of Γ the system can support spontaneous polarization modes. Second, for positive Γ values, we see large changes in dipole moment from layer to layer, but the dipolar field shows much smaller variation. We think that this behaviour can be traced to the fact $|\xi_1| \sim |\xi_0|$, in particular $|2\xi_1/\xi_0| > 1$, which again has its origin in the fact this interlayer spacing $(a/4)$ is smaller than the distance of the in-plane nearest neighbour $(a/\sqrt{2})$.

We have here considered three structures for which the self-consistent dipole moment density and the dipolar fields have been determined layer by layer. From a comparison of these results along with those for the simple cubic, face-centred cubic and body-centred cubic systems, we are led to believe that for the structures (and for the crystallographic directions) for which the interplanar spacing becomes much smaller compared to the distance of the nearest neighbour in the plane, the behaviour of the dipole moment and the local field would be more interesting. However, in no case we have seen an enhancement in the dipolar field for the surface by an order of magnitude or more. This is consistent with the conclusions reached with the cubic structures.

Acknowledgment

One of the authors (N.K.) acknowledges a research grant from C.S.I.R., India, towards this work.

References

1. M. Born and E. Wolf, *Principles of Optics* (Pergamon Press, 1970), Sec. 2.3.
2. N. Kar and A. Bagchi, *Solid State Commun.* **33**, 645 (1980).
3. See, for example, R. Shuttleworth, *Proc. Phys. Soc. (London)* **A62**, 167 (1949).
4. B. R. A. Nijboer and F. W. de Wette, *Physica* **24**, 422 (1958).
5. G. D. Mahan, *J. Chem. Phys.* **43**, 1569 (1965).
6. F. W. De Wette, *Phys. Rev.* **123**, 103 (1961).

Modern Physics Letters B, Vol. 8, No. 6 (1994) 361–366

PHOTOEMISSION CALCULATION WITH KRONIG–PENNEY MODEL

R. K. THAPA
Department of Physics, Pachhunga University College, Aizawl, Mizoram 796 001, India

P. DAS and N. KAR
Department of Physics, North Bengal University, Siliguri, West Bengal 734 430, India

Received 8 July 1993

Photoemission calculations have been performed using the Kronig–Penney model and including photon field variation with the help of a simple model, where the dielectric response in the surface region is a local function linearly interpolated between the vacuum value and the experimentally measured bulk value. Results with different dielectric functions are also presented.

For photoemission calculations, the current density may be written with the help of golden rule expression[1] as

$$\frac{dj(E)}{d\Omega} = \frac{2\pi}{\hbar} \Sigma |\langle \psi_f | H' | \psi_i \rangle|^2 \delta(E - E_f) \delta(E_f - E_i - \hbar\omega) f_0(E - \hbar\omega)[1 - f_0(E)], \quad (1)$$

where $|\psi_i\rangle$ and $|\psi_f\rangle$ refer to the initial and final states, and $H' = (e/2mc)(\mathbf{A}\cdot\mathbf{p} + \mathbf{p}\cdot\mathbf{A})$ with $\mathbf{p}$ being the one electron momentum operator and $\mathbf{A}$ is the vector potential for the photon field. Although the one electron states are treated quite accurately in many photoemission calculations (see, for example, Ref. 2), the variation of the photon field in the surface region is usually neglected. We have used a simple model for field calculations[3] with the experimentally determined photon energy-dependent dielectric functions as the input parameters, and used this in conjunction with free electron wave functions to explain the normal photoemission from the Fermi level for aluminum (100) surface with some success.[4] To incorporate band structure effects, we shall consider here the Kronig–Penney model for the electron states, and determine the photoemission cross section with this model.

The Kronig–Penney model has been used in connection with surface electronic states by several authors.[5,6] It has been seen that some surface related features come out, at least qualitatively, from these calculations. Schaich and Ashcroft[7] have

PACS No.: 79.60-i.

calculated numerically the photo yield by using the modified form of the Kronig–Penney model. Band structure effects were also included in it. They used the wave function of Mitchell[8] for free electron gas in a semi-infinite box and considered the photon field vector to remain constant. However, the numerical data as obtained by them in the case of potassium is quite realistic. This is evident for the nature of the photocurrent data obtained by them from various planes below the surface. Steslicka[9] had performed a detailed calculation of the surface states using the Kronig–Penney model both for the semi-infinite and the infinite crystal model. Eldib[10] had also applied the Kronig–Penney model to one-dimensional crystal. He had calculated only the electronic energy bands for mono- and polyatomic crystals and compared his data with the one computed by using the linear combinations of atomic orbital methods.

In this paper, we shall use a one-dimensional Kronig–Penney model to represent the crystal potential field by a linear array of δ-function wells. By using essentially the electromagnetic field for p-polarized radiation, as given by Bagchi and Kar,[3] and also used by us previously,[4] we shall calculate the photoemission cross section. The initial state wave function will be the one deduced by Thapa and Kar.[11] The relevant matrix element then can be written as, using atomic units ($e = m = \hbar = 1$),

$$\begin{aligned}\langle\psi_f|H'|\psi_i\rangle &= \int_{-\infty}^{\infty} \psi_f^*(z) H' \psi_i(z) dz\,,\\ \langle\psi_f|H'|\psi_i\rangle &= \int_{-\infty}^{\infty} \left[\psi_f^*(z) A_\omega(z) \frac{d\psi_i}{dz} + \frac{1}{2}\psi_f^*(z) \frac{dA_\omega}{dz}\psi_i(z)\right] dz\,,\end{aligned} \tag{2}$$

using the commutation relation between A and p, with $A_\omega(z)$ being the vector potential for the photon with energy $\hbar\omega$.

The expressions for $A_\omega(z)$ are the same as given by Bagchi and Kar,[3] and may be written as

$$A_\omega(z) = \begin{cases} A_1\,, & z < -a/2\,,\\ \dfrac{A_1}{z/a + B_1}\,\dfrac{\varepsilon(\omega)}{1-\varepsilon(\omega)}\,, & -a/2 < z < a/2\,,\\ \varepsilon(\omega) A_1\,, & z > a/2\,,\end{cases} \tag{3}$$

with $\varepsilon(\omega)$ being the dielectric function and A_1 and B_1 are constants depending on $\varepsilon(\omega)$ and the angle of incidence. The surface region is $-a/2 \le z \le a/2$ where the dielectric function is a linearly interpolated one between the vacuum value and the bulk value.

In Eq. (2) above, $\psi_f(z)$ is the free electron final state wave function as given by the following expression:

$$\psi_f(z) = \begin{cases} (1/2\pi q)^{1/2}\,\dfrac{2q}{q+k_f}\,e^{ik_f z}\,, & z < 0\,,\\ (1/2\pi q)^{1/2}\left[e^{iqz} + \left(\dfrac{q-k_f}{q+k_f}\right)e^{-iqz}\right], & z > 0\,,\end{cases} \tag{4}$$

where $k_f^2 = 2E_f$, $q^2 = 2(E_f - V_0)$, and $E_f = E_i + \hbar\omega$.

To evaluate the initial state wave function $\psi_i(z)$, one generally solves the one-dimensional Schrödinger's equation which can be written as

$$\frac{d^2\psi(z)}{dz^2} + k_i^2\psi(z) = -2V(z)\psi(z)\,, \tag{5}$$

where $k_i^2 = 2E$ and $V(z)$ is the δ-function potential of the Kronig–Penney model.

We shall calculate $\psi_i(z)$ by matching the wave function and its derivative at $z = 0$. Let $\phi(z)$ denote the Bloch wave function deep in the metal and $\phi^*(z)$ the time reversal version of $\phi(z)$. The eigenfunction in the semi-infinite solid ($z < 0$) has been chosen to have the form

$$\psi_i(z) = \phi(z) - P\phi^*(z)\,, \tag{6}$$

where P is the reflection coefficient which was evaluated by matching the wave function and the slope at $z = 0$. One can then show that the initial state wave function for $z < 0$ may be written as

$$\psi_i(z) = (1 - iPe^{-i\delta}\sin\delta)e^{ik_iz} - (P - ie^{i\delta}\sin\delta)e^{-ik_iz}\,, \tag{7}$$

where

$$\cot\delta = -\frac{k_i}{g}$$

with g being the strength of the potential. The initial state wave function outside the metal ($z > 0$) is

$$\psi_i(z) = Te^{-\varkappa z}\,, \tag{8}$$

where T is the transmission coefficient across the boundary plane and

$$\varkappa^2 = 2(V_0 - E)\,, \tag{9}$$

V_0 being the step potential at the surface. By matching conditions at $z = 0$, we get

$$P = \frac{(\varkappa - ik_i) - (k_i - i\varkappa)e^{i\delta}\sin\delta}{(\varkappa - ik_i) + (k_i - i\varkappa)e^{-i\delta}\sin\delta}\,, \tag{10}$$

$$T = \frac{2k_i\sin 2\delta}{(\varkappa - ik_i) + (k_i - i\varkappa)e^{-i\delta}\sin\delta}\,. \tag{11}$$

The proper evaluation of P and T with the appropriate numerical values for other factors enables one to write explicitly the initial state wave function ψ_i. The photoemission cross section was calculated by using the formula

$$\frac{d\sigma}{d\Omega} = \frac{k^2}{\omega}\,|\langle\psi_f|H'|\psi_i\rangle|^2\,. \tag{12}$$

The matrix element $I = \langle\psi_f|H'|\psi_i\rangle$ in Eq. (12) can be written as

$$I = \int_{-\infty}^{-a/2} \psi_f^* A_\omega(z) \frac{d\psi_i}{dz}\, dz + \int_{-a/2}^{0} \psi_f^* A_\omega(z) \frac{d\psi_i}{dz}\, dz$$
$$+ \frac{1}{2} \int_{-a/2}^{0} \psi_f^* \frac{dA_\omega(z)}{dz} \psi_i dz + \int_{0}^{a/2} \psi_f^* A_\omega(z) \frac{d\psi_i}{dz} dz$$
$$+ \frac{1}{2} \int_{0}^{a/2} \psi_f^* \frac{dA_\omega(z)}{dz} \psi_i dz + \int_{a/2}^{\infty} \psi_f^* A_\omega(z) \frac{d\psi_i}{dz}\, dz\,. \qquad (13)$$

To calculate the photocurrent, these integrals were evaluated analytically, where possible, or numerically. To ensure convergence a factor of $e^{-\alpha|z|}$ was introduced for $z < 0$. This represents the effect of inelastic collisions. We have used complex dielectric functions corresponding to tungsten and silicon. The data for these were those given by Weaver[12] and Edwards.[13] Since it is a model calculation, we have chosen the same set of data (in a.u.) for these two cases: $E = 0.43$ eV, $\delta = -0.5753$, $g = 0.60$, and $\theta = 45°$.

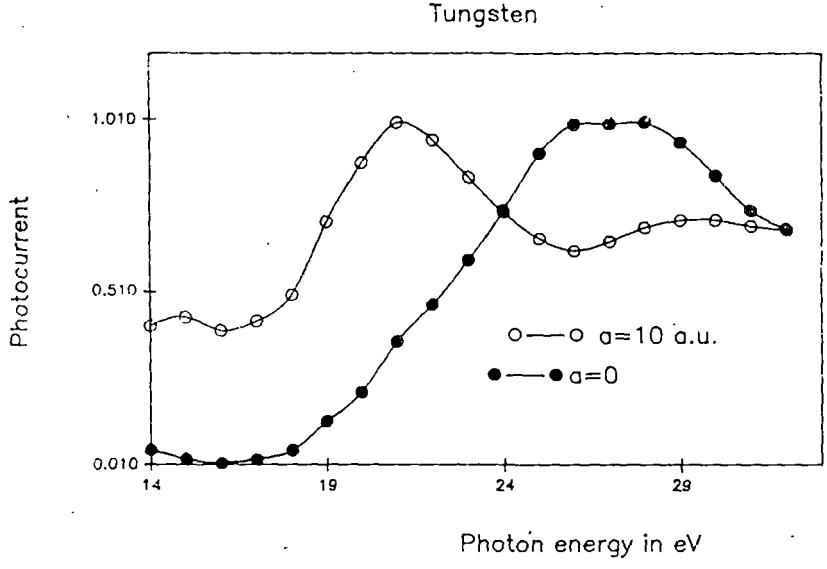

Fig. 1. Photocurrent against photon energy plots with tungsten dielectric functions for $a = 10$ a.u. and $a = 0$, i.e. with Fresnel field. The scales for the two curves are not the same; they have been so adjusted that the maxima for the two curves become comparable.

The results obtained with the dielectric function of tungsten for $\alpha = 0.5$ and $a = 10$ a.u. are shown in Fig. 1 (the curve with open circles). As expected, there is a minimum around the plasmon energy ($\hbar\omega_p$) which in this case is about 25 eV.

There is a peak below $\hbar\omega_p$ and another broad one above it. We also did a calculation without any surface region (Fig. 1 — the curve with closed circles) and again we find that the minimum at the plasmon energy is missing, but instead there is a maximum at 27 eV. Experimental observations of photocurrent from the tungsten (100) surface state did show a minimum at the $\hbar\omega_p$ and this supports our conclusion that the surface variation of the photon field is important in analyzing this type of spectrum.

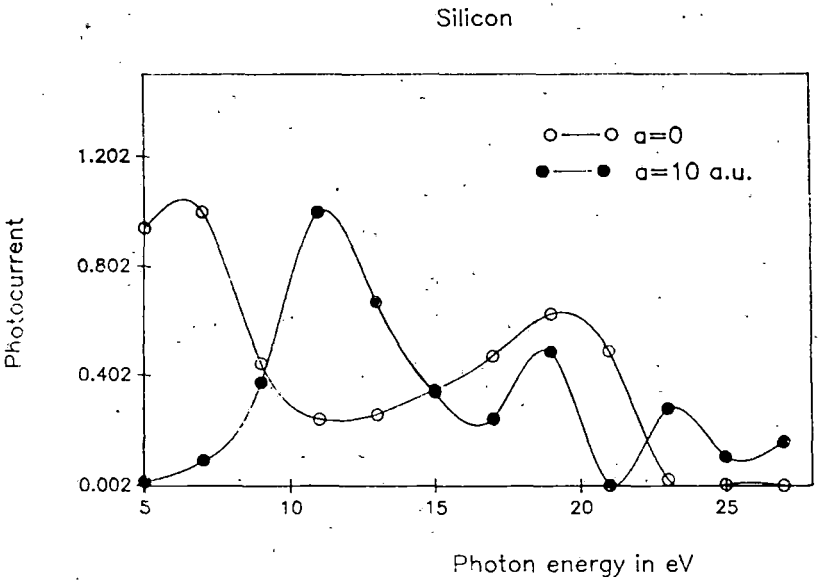

Fig. 2. Photocurrent against photon energy plots with silicon dielectric functions for $a = 10$ a.u. and $a = 0$, i.e. with Fresnel field. The scales for the two curves are not the same; they have been so adjusted that the maxima for the two curves become comparable.

We have also used this model in conjunction with the dielectric function $\varepsilon(\omega)$ for silicon as given by Edwards[12] which is a semiconductor and has a somewhat different dielectric response. With the same Kronig–Penney parameters and the same E, the results for $\alpha = 0.5$ and $a = 10$ a.u. are shown in Fig. 2 (the curve with filled circles). As in the other cases, there is a minimum at the plasmon energy around 16 eV. There is a maximum below $\hbar\omega_p$ and the current rises also beyond $\hbar\omega_p$. But in this case, we see another minimum which is at 21 eV. The reason for this can be traced to the behavior of $\varepsilon(\omega)$ for silicon which has instability in the region of 21 eV. As a result of this, the fields inside the solid become extremely small and, consequently, the photocurrent also shows a minimum. The photocurrent calculated with no surface region, i.e. with Fresnel fields (Fig. 2 — the plot with open circles) shows no minimum at 16 eV (the plasmon energy of silicon) and a

maximum at 21 eV. This, again, demonstrates that the behavior with and without the surface region is strikingly different.

A study of these cases shows that the surface variation of the photon field is important in calculating photoemission cross section, since neglecting it fails to reproduce the minimum at the plasmon energy. We also see that using dielectric functions corresponding to different elements changes the results. All of these point to the fact that a full fledged photoemission calculation should include the correct variation of photon field near the surface.

Acknowledgement

One of the authors (N.K.) acknowledges a research grant from the Council of Scientific and Industrial Research, India. The other author (R.K.T.) also acknowledges a grant from the Department of Atomic Energy, India.

References

1. D. R. Penn, *Phys. Rev. Lett.* **28**, 1041 (1972).
2. J. B. Pendry, *Surf. Sci.* **57**, 679 (1976).
3. A. Bagchi and N. Kar, *Phys. Rev.* **B18**, 5248 (1978).
4. P. Das, R. K. Thapa, and N. Kar, *Mod. Phys. Lett.* **B5**, 65 (1991).
5. W. Shockley, *Phys. Rev.* **56**, 317 (1939).
6. S. G. Davison and J. D. Levine, *Solid State Phys.* **25**, 2 (1970).
7. W. L. Schaich and N. W. Ashcroft, *Phys. Rev.* **B3**, 2452 (1971).
8. K. Mitchell, *Proc. Royal Soc. London, Ser.* **A146**, 443 (1934).
9. M. Steslicka, *Prog. Surf. Sci.* **5**, 157 (1974).
10. A. M. Eldib, H. F. Hassaon, and M. A. Mohmad, *J. Phys.* **C20**, 3011 (1987).
11. R. K. Thapa and N. Kar, *Indian J. Pure Appl. Phys.* **26**, 620 (1988).
12. J. Weaver, in *Handbook of Chemistry and Physics of Solids* (CRC Press, Boca Raton, Ohio, 1987) E-377.
13. D. F. Edwards, *Handbook of Optical Constants of Solids*, ed. E. P. Palik (Orlando, Academic, 1985) p. 555.